

## Energetic neutral atom imaging of space plasmas

Mike Gruntman

*Department of Aerospace Engineering, MC-1191, University of Southern California, Los Angeles, California 90089-1191*

(Received 20 February 1997; accepted for publication 18 July 1997)

Experimental techniques and instrumentation for space plasma imaging in fluxes of energetic neutral atoms (ENAs) are reviewed. ENAs are born in charge exchange collisions between space plasma energetic ions and background neutral gas. ENAs are ubiquitous in the space environment and their energies are in the range from a few eV up to  $>100$  keV. Contrary to charged particles, ENAs can travel large distances through space with minimal disturbance, and by recording ENA fluxes as a function of observational direction, one can reconstruct a global image of a planetary magnetosphere or the heliosphere. Plasma ion energy distribution and ion composition can be remotely established by measuring ENA energies and masses. ENA imaging opens a new window on various phenomena in space plasmas with a promise to qualitatively improve our understanding of global magnetospheric and heliospheric processes. At first we review ENA fluxes in space and their properties, and present a brief history of ENA experimental studies and the evolution of experimental approaches. The concepts of ENA imaging and particle identification are considered and followed by comparison with corpuscular diagnostics of fusion plasmas. Basic ENA techniques and instrument components are then described in detail and critically evaluated; performance characteristics, limitations, and requirements to key instrumental elements are discussed. And finally, representative ENA instruments are shown, and promising instrumental approaches are identified. © 1997 American Institute of Physics. [S0034-6748(97)02810-4]

### I. INTRODUCTION

In the beginning of the space age, in the 1950s and early 1960s, many space experiments were simply an extension of the measurements performed in the physics laboratory, although under very unusual conditions of spacecraft. Severe limitations of available power, requirements of small mass and size, remote control and data acquisition through limited telemetry called for new approaches to designing and building space instruments. An emphasis on reliability—one cannot go and replace a fuse or correct axis alignment on a spacecraft in orbit—was another important new requirement. Space experiments were initially considered by many in the physics community as an unconventional application of simplified laboratory techniques. (As Samuel Johnson put it, “A horse that can count to ten is a wonderful horse, not a wonderful mathematician.”) However with time, space instruments evolved into a highly specialized area of scientific instrumentation pioneering new measurement techniques and leading instrument development in such areas as plasma analyzers, particle- and photon-counting position-sensitive detectors, and many others. In this article we review a new emerging field of space experiments and instrumentation: imaging of space plasmas in fluxes of energetic neutral atoms.

The interaction between charged and neutral particles is a common phenomenon in space plasmas. Whenever an energetic ion undergoes a charge exchange process in a collision with a neutral background atom, an energetic neutral atom (ENA) is born. Ion-electron recombination and neutral

atom acceleration by the solar gravitation may also contribute to an ENA population under certain conditions. ENAs are ubiquitous in space environment and their study opens a new window on various phenomena in space plasmas with a promise to qualitatively improve our understanding of global magnetospheric and heliospheric processes. However ENAs have remained poorly explored due to enormous experimental difficulties.

ENAs, contrary to charged particles, can travel large distances through space with minimal changes without undergoing further interaction with plasma. ENA measurements are recognized as a powerful tool to remotely study various global plasma objects in space.<sup>1–12</sup> By recording ENA fluxes as a function of observational direction, one can reconstruct a global image of the object of interest, thus the term “ENA imaging,” first introduced in 1984 for imaging from outside<sup>13</sup> and from inside<sup>14</sup> of the magnetosphere. Plasma ion energy distribution and ion composition can be remotely established by measuring ENA energies and masses. ENA imaging usually means not only determining ENA flux angular distribution but also ENA energies and masses. An ENA imaging experiment would ideally produce a set of images of a plasma object in ENAs of different masses and in different energy ranges.

Protons are the most abundant component of space plasma ions. Unlike other space plasma ions (e.g.,  $\text{He}^+$  and  $\text{O}^+$ ), protons cannot be imaged optically, which makes ENAs in many cases the only tool to study processes of interest remotely. The definition of an “energetic” particle

was originally limited by a minimum energy of several keV, but new experimental techniques have significantly lowered the energy threshold. For the purpose of this article, the ENAs occupy the energy range from few eV up to several hundred keV.

Any object that contains energetic ions and background neutral gas can be imaged in ENA fluxes. Important examples are planetary magnetospheres and the heliosphere. (The heliosphere, the region containing expanding solar wind plasma, is about 200 AU in size; 1 AU = 1 astronomical unit =  $1.5 \times 10^{13}$  cm is the distance between the earth and the sun.) Planetary magnetospheres are filled with plasma and the solar wind plasma fills interplanetary space in the heliosphere. Being far from thermodynamic equilibrium, space plasmas are characterized by wildly varying populations of energetic ions. Neutral atom background around the Earth is provided by the terrestrial exosphere that contains escaping hydrogen atoms;<sup>15–17</sup> the extended hydrogen geocorona was observed and measured many times.<sup>18,19</sup>

The presence of a global population of neutral atoms in interplanetary space is less known. The interstellar gas from the local interstellar medium (LISM) permeates the heliosphere. If one excludes the sun, planets, and other celestial bodies, then 98%–99% of the mass of matter filling the heliosphere is represented by neutral atoms with only the remaining 1%–2% of matter being plasma.<sup>10</sup> Outside the heliosphere, interstellar space is filled by dilute interstellar gas with varying degrees of ionization. Hence ENAs are born in the planetary environment and in interplanetary and interstellar space as well.

Almost 3 decades of instrument development made ENA imaging of space plasmas possible: the phase of practical implementation has been finally achieved. Simple ENA instruments were recently flown on GEOTAIL,<sup>20</sup> CRRES,<sup>21</sup> and ASTRID<sup>22,23</sup> missions around the Earth. A sophisticated first large size ENA camera will perform imaging of the Saturn's magnetosphere on the Cassini mission to be launched in October 1997.<sup>24</sup> A dedicated space mission to globally image the terrestrial magnetosphere was studied for several years.<sup>25–27</sup> A medium-class explorer (MIDEX) mission IMAGE was recently selected by NASA to perform such imaging; it is presently under preparation for launch in January, 2000. Another ENA experiment ISENA<sup>28</sup> was unfortunately lost with the SAC-B spacecraft during launch in October 1996. A number of other experiments to image planetary magnetospheres and the heliosphere have been proposed and are currently at different stages of development.

ENA images and their evolution in time promise a breakthrough in the understanding of fundamental global processes in space. Conventional *in situ* measurements of local plasma parameters are inherently limited in their capabilities. Some plasma regions of interest are too far away to be conveniently visited by spacecraft. For example, only remote observations are capable of providing continuous monitoring of the time-varying size and shape of the global heliosphere.<sup>6–9,29</sup>

Experimental studies of planetary magnetospheres face difficulties of another kind. The measurements of magnetospheric plasma are performed from fast moving (2–9 km/s)

spacecraft, and they cannot unambiguously distinguish between temporal and spatial variations of plasma parameters.<sup>1,5</sup> Consequently even the simultaneous measurements from several spacecraft are inherently insufficient for reconstruction of complex global magnetospheric processes and require heavy reliance on often simplified and incomplete models.

Accurate understanding of the global magnetospheric processes has become especially important with the growing realization of possible adverse effects of space environment on many technological systems, both on the ground and in space. Communications, TV broadcasting, world-wide navigation, and national security applications that include advance warning, reconnaissance, and nonproliferation compliance monitoring, are increasingly dependent on space-deployed technical assets. Our ability of predicting the magnetospheric conditions, especially during geomagnetic storms, remains disappointing.<sup>30</sup> NASA, the Air Force, and National Oceanic and Atmospheric Administration (NOAA) are currently working to establish a national space weather service.<sup>31,32</sup>

Although first dedicated direct ENA measurements were attempted in the late 1960s, enormous experimental difficulties prevented detailed study of ENAs. ENA fluxes are very weak, sometimes  $< 1 \text{ cm}^{-2} \text{ s}^{-1}$ , and the realistic approach to their direct detection is based on particle interaction with solid surfaces, e.g., electron emission. Ultraviolet (UV) and extreme ultraviolet (EUV) photons interact with surfaces often in a similar way, and the background EUV/UV photon fluxes are 3–7 orders of magnitude higher than those of ENAs. Therefore background photon-induced count rate of a conventional secondary electron multiplier would be 2–6 orders of magnitude higher than the ENA count rate. Such inhospitable conditions make ENA measurement an exceptionally challenging task.

There are similarities and there are essential differences between corpuscular diagnostics of hot plasmas in the laboratory and ENA diagnostics of space plasmas. Neutral atom emissions from magnetically confined fusion plasmas were used efficiently to determine plasma ion temperature.<sup>33–36</sup> The photon-to-ENA ratios in space are not unlike those from fusion plasmas. An important difference between conditions in space and those in the laboratory is that fusion plasma processes are of relatively short duration,  $< 1\text{--}10$  s, with high ENA fluxes, while ENA fluxes are very low in space but it is possible to accumulate the signal much longer. For example, the desired temporal resolution for study of important magnetospheric ring current is in the 5–15 min range. The fusion plasmas have become “ENA-thick” with the increasing density, which limits passive corpuscular diagnostics to the study of the plasma edges. In space, the objects are usually “ENA-thin,” and ENAs can travel large distances without much disturbance.

The goal of this article is to review and critically evaluate *experimental techniques and instrumentation for space plasma imaging in ENA fluxes*, covering the energy range from a few eV up to  $> 100$  keV. ENA instrumentation was traditionally divided into two groups corresponding to “high” and “low” energies with a new “ultralow” energy

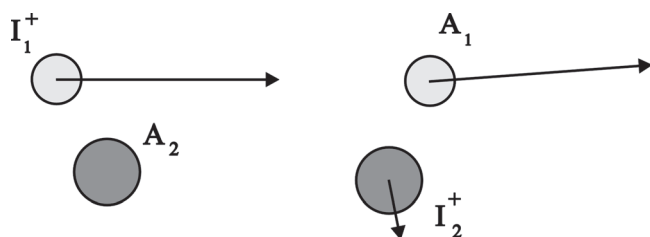


FIG. 1. Charge exchange collision between an energetic plasma ion and a neutral gas atom;  $I_1^+$  is an ion of species “1” and  $A_2$  is an atom of species “2.”

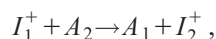
group emerging. (Due to the lack of a better phrase we will be using hereafter such awkward terms as “low-energy ENA” and “high-energy ENA.”) The division between high- and low-energy ENAs, although never clearly defined, results from use of different approaches and instrument components for suppression of EUV/UV radiation. For example, solid state detectors and thin-film filters are used in high-energy ENA instruments, while many other components, such as ultrathin foils and microchannel plate detectors, are common for both groups. ENA instruments employ many approaches and techniques widely used in space ion analyzers which is an exceptionally developed and advanced area of space instrumentation;<sup>37–49</sup> the ion analyzers are beyond the scope of this article.

At first we review ENA fluxes in space and their properties, and present a brief history of ENA experimental study and the evolution of experimental approaches. The concepts of ENA imaging and particle identification are considered and followed by comparison with corpuscular diagnostics of fusion plasmas. Basic ENA techniques and instrument components are then described in detail and critically evaluated; performance characteristics, limitations, and requirements to key instrumental elements are discussed. And finally, representative ENA instruments are shown and promising new approaches and developments are identified.

## II. ENAS IN SPACE

### A. Charge exchange collisions

ENA fluxes come from different ion populations with different compositions, flux levels, and energy, spatial, and temporal dependencies. ENAs are formed in charge exchange collisions (Fig. 1) between energetic plasma ions and neutral gas atoms



where  $I_1^+$  is an ion of species “1” and  $A_2$  is an atom of species “2.” Species “1” and “2” may be identical (e.g.,  $H^+ + H \rightarrow H + H^+$ ), and a simultaneous exchange of two electrons is possible ( $He^{++} + He \rightarrow He + He^{++}$ ). The initial velocity of an energetic particle is only slightly changed in a charge exchange collision.<sup>50</sup> Proton–hydrogen charge-exchange collisions are often the most important process in space plasma: they occur at large impact parameters with only a small momentum exchange between collision partners. For many practically important applications ENAs can be assumed to be born exactly with the ion momentum.

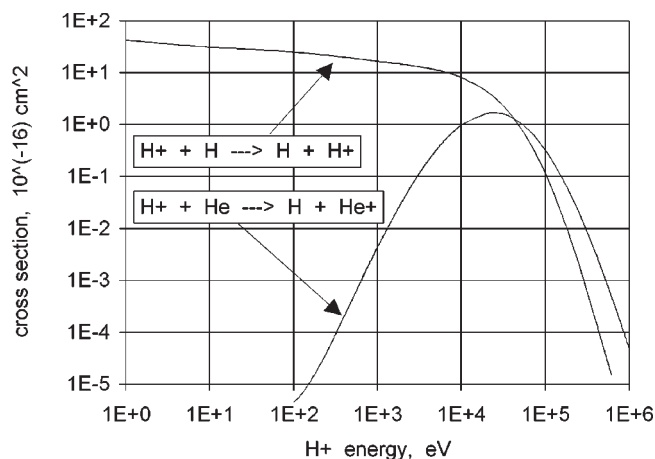


FIG. 2. Cross section energy dependence for proton charge exchange on hydrogen and helium atoms.

After the birth of an ENA, its trajectory is defined by the initial velocity and gravitational forces only. With a few exceptions, gravitation can be disregarded, and one can assume that the ENA preserves both the direction and magnitude of the energetic ion velocity before the charge-exchange collision. As ENAs travel in space, they may be lost in charge exchange, electron collisions, and photoionization.

Only few species are important for ENA formation. Neutral gas in the heliosphere consists of hydrogen ( $\sim 90\%$ ) and helium ( $\sim 10\%$ ) atoms. Atomic hydrogen dominates the neutral particle environment around the earth from an altitude of 600 km and a few thousands km during periods of minimum and maximum solar activity, respectively. Other important neutral species around the earth are helium and oxygen atoms. Magnetospheric plasma consists mostly of protons with some helium, oxygen, and sulfur (found at Jupiter) ions. The protons are the major component of the interstellar and solar wind plasmas; the latter contains also  $\sim 5\%$  of double-charged helium ions (alpha particles).

Charge exchange cross sections important for ENA production are readily available.<sup>51</sup> A cross section energy dependence for proton charge exchange on hydrogen and helium atoms is shown in Fig. 2. The difference in cross sections reflects the fact that charge exchange is of a resonance type for proton–hydrogen collisions and requires overcoming an energy threshold in proton–helium collisions. Since the background neutral hydrogen is usually much more abundant than helium, the charge exchange on hydrogen atoms would dominate hydrogen ENA production for energies  $< 10\text{--}100\text{ keV}$ . The charge exchange on helium may become however important for energies  $> 100\text{ keV}$ .

The ENA measurements would allow one to study the ion population if neutral gas parameters are known, and conversely the neutral atom population characteristics could be obtained if the ion parameters are known. Some information is usually available on both the ions and neutral gas, but often we have a relatively good knowledge of only one component, for example neutral particle environment around the earth. Let us consider now the sources of major magnetospheric and heliospheric ENA fluxes.

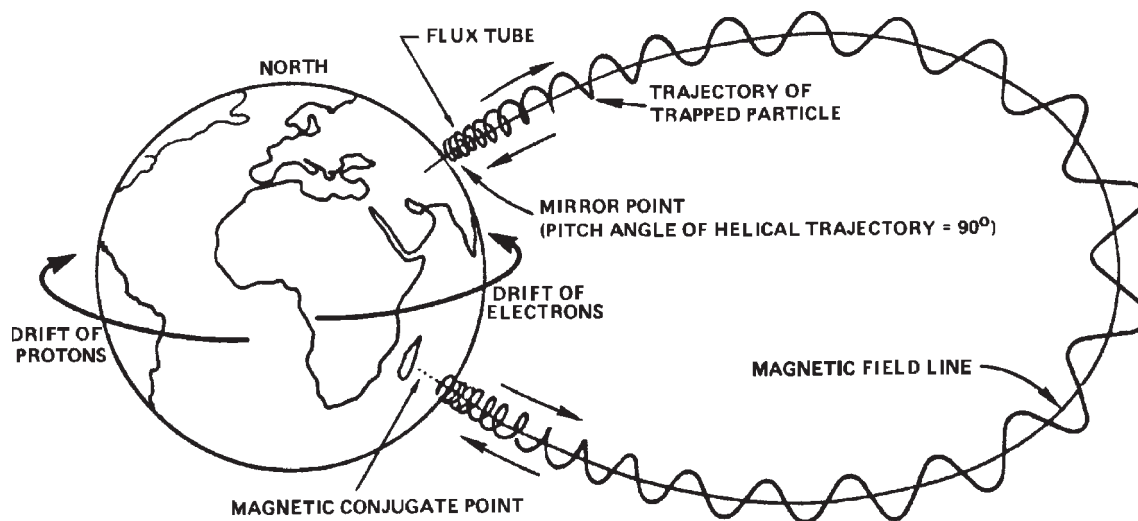


FIG. 3. Planet's magnetic field dominates the magnetosphere and traps charged particles, which may be accelerated up to very high energies. Trapped charged particles gyrate about magnetic field lines, participate in drift motion, and form radiation belts. (After Ref. 52.)

## B. Magnetospheric ENAs

Magnetospheres are objects formed by the solar wind plasma flow around planets with intrinsic magnetic field (Mercury, Earth, Jupiter, Saturn, Uranus, and Neptune). Magnetic field presents an obstacle for the highly supersonic solar wind plasma flow, and a bow shock is formed in front of the planet. The size and shape of the magnetospheres are determined by the strength and orientation of the magnetic field, which is usually compressed at the sunward side and significantly stretched at the nightside (magnetospheric tail). Planets without intrinsic magnetic field (Venus, Mars, and Moon) may sometime form magnetospherelike plasma structures around the upper atmospheres that are ionized by solar EUV and x-ray radiation. The earth's magnetic field dominates the terrestrial magnetosphere and efficiently traps charged particles (Fig. 3), which may be accelerated up to very high energies.<sup>52</sup> The ionospheric and solar wind plasmas find a way to leak and fill the magnetosphere with ions and electrons.

Various aspects of magnetospheric physics are discussed

in a number of publications.<sup>53–68</sup> The earth's magnetosphere is shown schematically in Fig. 4. The bow shock is located approximately at the distance of 12–18  $R_E$  ( $R_E \approx 6370$  km is the earth's radius). A long magnetospheric tail may stretch far beyond the Moon's orbit ( $\sim 380\,000$  km) in the antisolar direction. Processes in the magnetospheric tail play an important role in transport of energized plasma toward the earth during magnetospheric disturbances. The orbits of practically all earth-orbiting satellites are inside the magnetosphere. Low-earth orbits are those with altitudes below a few thousand km. A large number of communications and direct broadcasting satellites are at geosynchronous (geostationary) orbit with a one-day period. This orbit is at approximately a 36 000 km altitude which is well within the magnetosphere.

A magnetosphere is a very complicated object with plasma parameters varying wildly from one region to another. Solar wind carries frozen-in interplanetary magnetic field, about  $\sim 5$  nT near the earth, which changes its direction occasionally. Interplanetary magnetic field interaction with the geomagnetic field is important for energy transfer to the magnetosphere. Many processes involving magnetic field occur in the boundary region between the plasma of the geospheric origin and the solar wind plasma, the geopause.<sup>67</sup> The geopause is at a geocentric distance of  $\sim 10 R_E$  on the upstream side. Variations of the solar wind pressure and magnetic field result in change of the magnetosphere's size, shape, electric current patterns, and ion flows and lead to energization of electrons and ions and development of various instabilities.<sup>53,58,69</sup>

The solar-terrestrial link through the interaction of the solar wind with the magnetosphere makes magnetospheric conditions strongly dependent on the solar activity. The most prominent manifestation of this link is large nonrecurrent geomagnetic storms, which are believed to be triggered by relatively dense clouds of plasma ejected from the solar surface, the so called coronal mass ejections, impinging on the magnetosphere.<sup>70–76</sup> A magnetospheric storm is accompanied by an increase of a ring current,<sup>5,69,77,78</sup> which produces perturbations up to 1% of the magnetic field at the earth's

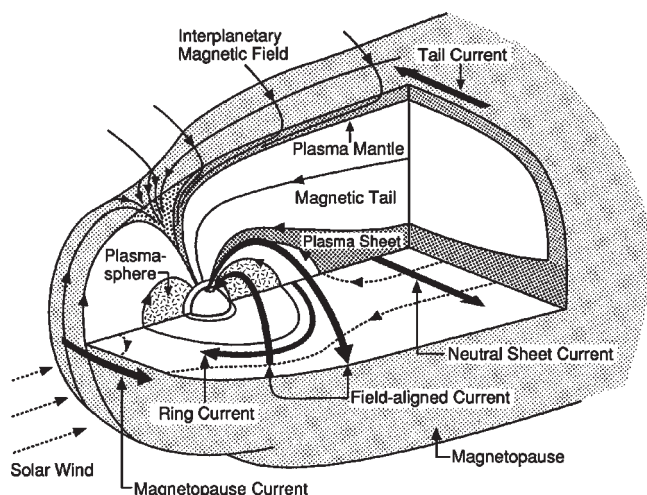


FIG. 4. Three-dimensional cutaway view of the terrestrial magnetosphere showing various currents, fields, and plasma regions. (After Ref. 197.)



surface. The ring current is an electric current flowing around the earth due to the presence of energetic ions in the magnetosphere; its decay occurs largely through charge exchange on background neutral atoms resulting in production of ENA fluxes.<sup>69,77,79</sup>

Magnetospheres of other planets have been studied by flyby spacecraft (Mercury, Jupiter, Saturn, and Uranus), in some cases (Venus and Mars) by orbiters and landers, and by astronomical observations and radio emission detections from earth. There are detailed descriptions of the magnetospheres of Mercury,<sup>80–82</sup> Venus,<sup>81,83</sup> Mars,<sup>81,84</sup> Jupiter,<sup>85,86</sup> Saturn,<sup>87</sup> and Uranus.<sup>88</sup> The magnetosphere of Jupiter is currently being explored by the Galileo orbiter, and the magnetosphere of Saturn will be studied by the forthcoming Cassini mission.

The emphasis of the study of the terrestrial magnetosphere has shifted from discovering the new magnetospheric features to attempts to explain how the magnetosphere works. Such shift is driven not only by the maturing of the field but by the practical requirements as well. An important goal is to construct a magnetosphere model that will provide capabilities of predicting magnetosphere's behavior in response to solar disturbances, in particular characteristics of geomagnetic storms and substorms. Although a clear understanding of the relation between the disturbed space weather conditions and adverse effects on various technological systems has yet to be achieved,<sup>71,89,90</sup> significantly improved knowledge of geomagnetic storm processes is needed to better understand and to reduce storm-related damage.

On the ground, major magnetospheric disturbances cause changes in the geomagnetic field, which in turn lead to the induction currents in long conductors.<sup>91</sup> Effects of geomagnetic disturbances include disruptions of cable communications, which were observed in telegraph lines since the middle of the 19th century,<sup>91,92</sup> interference with navigational systems such as LORAN and OMEGA and high-frequency (HF) and ultrahigh frequency (UHF) communications; various effects (leading to blackouts of large areas) on power distribution systems;<sup>93</sup> corrosion of pipelines;<sup>94,95</sup> and interference in high-resolution global positioning system (GPS) technology. Magnetospheric storms significantly increase precipitation of energetic particles, which poses health hazards to airline crews and passengers at high altitudes on polar routes; the crews of high-altitude reconnaissance planes may also be affected.

In space, magnetospheric disturbances damage and reduce lifetime of satellites,<sup>96,97</sup> both at low-earth and geosynchronous orbits. In particular, excessive charging of spacecraft surfaces may cause irreparable damage to space systems.<sup>98,99</sup> Major geomagnetic storms lead to heating and expansion of the upper atmosphere. The atmospheric expansion may lead to a significant increase of atmospheric drag on low-altitude satellites and cause their premature reentry. Establishment of a national space weather service requires significantly improved understanding of adverse effects of the disturbed space weather conditions on technological systems<sup>89,90,97</sup> as well as capabilities of advance warning and storm prediction.<sup>30–32</sup>

Plasmas in different regions of the terrestrial magneto-

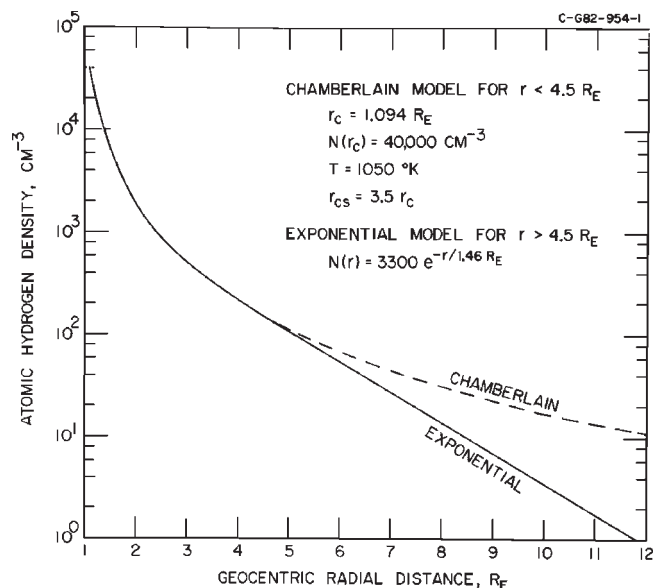


FIG. 5. Radial profile of the spherically symmetric geocoronal hydrogen number density. (After Ref. 102.)

sphere, radiation belts, cusps, plasmasphere, magnetosheath, plasma mantle, plasma sheet, and polar wind, are characterized by widely varying parameters, and these regions actively interact with each other. For example, magnetosheath plasma has temperatures of 0.1–1 keV, proton energies in the magnetospheric tail proton streams are 10–100 eV, while ions in the ring current have energies between few hundreds eV up to hundreds of keV. The macroscale characteristics of the magnetospheric regions and their boundaries and how they interact to define global characteristics of the magnetosphere are not well known<sup>5,100</sup> resulting in a long list of unanswered specific questions.<sup>101</sup>

The uppermost part of a planetary atmosphere, the exosphere,<sup>15–17</sup> provides neutral collision partners for ENA production. The exospheric hydrogen atom population was extensively studied around earth by the Dynamic Explorer (DE-1) satellite.<sup>102,103</sup> The number density distribution, which can be assumed to be spherically symmetric close to the earth, is shown in Fig. 5.<sup>102</sup> At larger geocentric distances, solar radiation pressure (in resonance hydrogen H I Ly- $\alpha$  line, 1216 Å) would produce an asymmetry of hydrogen spatial distribution.<sup>104</sup> Abundant background neutral gas can be found in the magnetospheres of other planets as well.<sup>105</sup>

The composition of magnetospheric ENAs is largely determined by the composition of energetic ions. Hydrogen (H), helium (He), and oxygen (O) ENAs have been identified by the first experimental ENA composition measurement in the terrestrial magnetosphere.<sup>106</sup> One expects to find also sulfur (S) ENAs in Jupiter's magnetosphere (sulfur is abundant in the plasma torus as a result of volcanic activity on Jupiter's moon Io).

Extensive computer modeling<sup>1,2,5,79,107–118</sup> predicts magnetospheric ENA fluxes escaping the earth's magnetosphere outward in the range  $0.01–10 \text{ cm}^{-2} \text{ s}^{-1} \text{ sr}^{-1} \text{ keV}^{-1}$ . For example, the ENA flux at 40 keV energy is  $\sim 10^2 \times (d/R_E)^2 \text{ cm}^{-2} \text{ s}^{-1} \text{ keV}^{-1}$  at large distance,  $d$ , from the

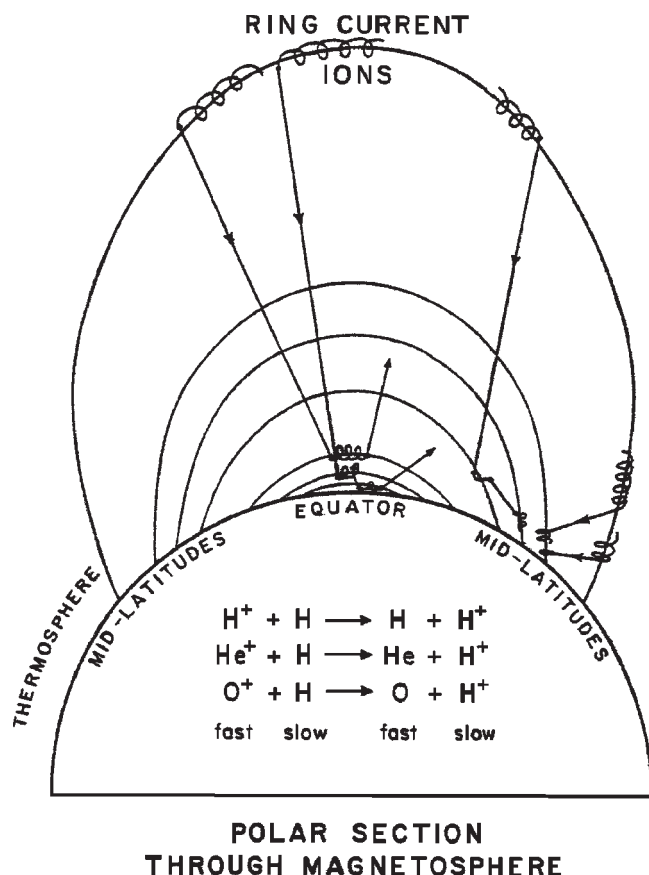


FIG. 6. ENAs produced in charge exchange of ring current ions. The neutrals travel on straight line trajectories, mostly outwards, but a fraction impinges on the upper atmosphere, and depending on species and energy, some will then re-ionize, and near the equator become temporarily trapped. (After Ref. 120.)

earth.<sup>5</sup> A typical angular resolution in ENA imaging instruments (an angular size of imaging pixels) is  $5^\circ \times 5^\circ \approx 8 \times 10^{-3}$  sr, or smaller, and the expected magnetospheric fluxes are in the range  $10^{-4}$ – $10^{-1}$  cm<sup>-2</sup> s<sup>-1</sup> keV<sup>-1</sup> per pixel.

An important type of ENAs can precipitate toward the earth surface,<sup>118–123</sup> for example ENAs born in charge exchange of ring current ions (Fig. 6). The ENAs may reach low altitudes where they are re-ionized by charge exchange and newly born energetic ions are trapped by the magnetic field.<sup>124</sup> The precipitating ENAs can be studied from low-earth orbit spacecraft and were recently measured by the CRRES<sup>21,125</sup> and ASTRID<sup>22,23,118</sup> satellites. The characteristics of precipitating ENAs are important for verification and testing of our theories of nocturnal thermospheric heating, low latitude aurorae, formation of a low-altitude ion belt at low latitudes, particle precipitation, and escaping neutrals. The precipitating ENA fluxes may be as high as  $10^4$  cm<sup>-2</sup> s<sup>-1</sup> sr<sup>-1</sup> keV<sup>-1</sup>.<sup>28,111,121</sup>

The measurements of precipitating ENA fluxes are possible only at altitudes higher than a certain level where the effect of collisions with ionospheric and atmospheric ions and neutrals is minimal. The collisions with atmospheric neutrals are the most important limitation,<sup>123</sup> and the computer simulations<sup>123</sup> showed that ENA measurements would be possible during solar maximum at altitudes higher than

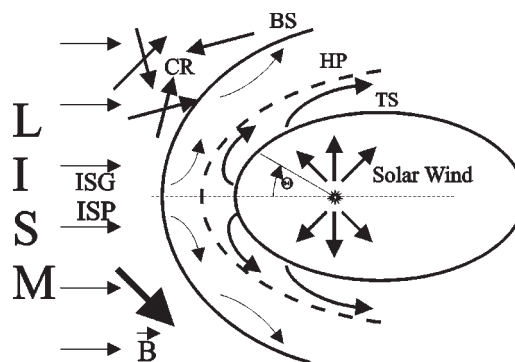


FIG. 7. Two-shock model of the solar wind interaction with the local interstellar medium (LISM). (TS) termination shock; (HP) heliopause; (BS) bow shock; (CR) cosmic rays; [ISG(P)] interstellar gas (plasma); (B) magnetic field.

600–700 km with less than 10% of ENAs affected. Actually the disturbance of ENA fluxes would be smaller since the effect of the collisions in the computer simulation<sup>123</sup> was overstated: the scattering angles of most of the ENAs that experienced an elastic collision would be smaller than the angular resolution of an ENA instrument. In addition, some elastic collision cross sections<sup>126</sup> were calculated in the angular range where the elastic scattering model assumption was not valid. One can expect that the measurements of precipitating ENAs would be possible at altitudes as low as 500–600 km.

### C. Heliospheric ENAs

The interaction between the sun and LISM is manifested by the buildup of a heliosphere.<sup>127–131</sup> The sun is a source of the highly supersonic flow of plasma called the solar wind.<sup>132–135</sup> Solar wind expands into the LISM which is filled with partially ionized interstellar gas, interstellar magnetic field, and cosmic rays. The LISM is a medium with a small but finite pressure. The dynamic pressure of the expanding solar wind flow decreases with distance from the sun, and at a certain distance the solar wind expansion must be stopped. The cavity containing the solar wind is called the heliosphere. The dynamic pressure of the solar wind varies by a factor of 2 during the 11-year solar cycle,<sup>136</sup> thus resulting in variations of the size and shape (heliosphere “breathing”) of the heliosphere.<sup>136,137</sup>

The heliosphere is a complicated phenomenon where solar wind and interstellar plasmas, interstellar gas, magnetic field, and cosmic rays play prominent roles. The structure of the heliosphere and its boundary, as well as properties of the LISM, are of fundamental interest and importance and the available experimental data are scarce and indirect. The heliosphere provides a unique opportunity to study in detail the only accessible example of a commonplace but fundamental astrophysical phenomenon—the formation of an astrosphere. A self-consistent model of the stationary heliosphere has yet to be built and some aspects of the interaction, for example temporal variations and instabilities, are not satisfactorily understood even on the qualitative level. The physics of the LISM is also poorly understood.<sup>138–140</sup>

Various heliospheric models were proposed for different solar wind plasma and LISM parameters.<sup>128–130,141–147</sup> A possible heliospheric structure is shown in Fig. 7 for the most advanced and quantitatively developed two-shock model.<sup>146,148–150</sup> A supersonic flow of the solar wind plasma terminates at a solar wind shock front [termination shock (TS)] beyond which its kinetic energy is largely converted into thermal energy of the subsonic plasma. A supersonic flow of the interstellar plasma (“interstellar wind”) is stopped at the bow shock (BS).

The interstellar wind blows from a direction with ecliptic longitude  $252^\circ$  and latitude  $+7^\circ$  and with a velocity  $26 \text{ km/s} = 5.5 \text{ AU/year}$ ,<sup>151–154</sup> and the heliosphere is likely to be elongated along this velocity vector (Fig. 7). Solar wind anisotropy<sup>135</sup> as well as the presence of the (currently unknown) interstellar magnetic field (typical value  $0.1\text{--}1 \text{ nT}$ ) would result in deviations from cylindrical symmetry. The earth is positioned in the upwind direction in the beginning of June each year. Neutral interstellar gas consists mostly (80%–90%) of hydrogen atoms with a number density  $0.05\text{--}0.2 \text{ cm}^{-3}$ ; the remaining atoms are helium with the addition of traces of heavier elements (O, Ne, Ar, etc.).<sup>138–140,155</sup> Interstellar gas is partially ionized,<sup>138,140,156</sup> and the interstellar plasma is believed to have a number density  $0.02\text{--}0.1 \text{ cm}^{-3}$ . The degree of interstellar gas ionization would affect the morphology of the heliospheric interface region.<sup>150</sup>

The estimates of the size of the heliosphere vary between 70 and 120 AU. The closest possible position of the termination shock is “pushed” steadily away from the sun by the Voyager 1 spacecraft, which was at 65.2 AU on January 1, 1997, and which continues to move in approximately the upwind direction with the speed of  $3.5 \text{ AU/year}$ . Voyager 1 did not cross the termination shock yet. Another distant spacecraft, Pioneer 10, was at 66.6 AU downwind from the sun on January 1, 1997, and it moves with the speed of  $2.7 \text{ AU/year}$ . The Pioneer 10 scientific mission was terminated several months ago due to decreasing capabilities of its power system.

## 1. Background neutral gas

Production of heliospheric ENAs requires background neutral gas. Two major sources of background neutral particles in the heliosphere are provided by the interstellar gas penetrating the solar system and, in the sun’s vicinity ( $<0.5 \text{ AU}$ ), solar wind plasma neutralization on interplanetary dust. Planets provide localized sources of thermally escaping neutral atoms. The lifetime of a hydrogen atom with respect to ionization is about 20 days at 1 AU. Hydrogen would form a cloud with a radius of  $0.01 \text{ AU}$  around the earth. Thus the highly localized planetary neutrals can be disregarded, when global populations of heliospheric ENAs are considered. However ENAs emitted by giant planets (Jupiter and Saturn) may substantially contribute to a global population of heliospheric neutral minor constituents, viz., atomic oxygen.<sup>157</sup>

Number density of interstellar gas is so small ( $\sim 0.1 \text{ cm}^{-3}$ ) that atom mean free path with respect a collision is larger than the expected size of the heliosphere.

Therefore interstellar neutral atoms can be treated as individual particles moving under the forces of the solar gravitational attraction and solar radiation pressure.<sup>158</sup> The radiation pressure approximately counterbalances solar gravitation for hydrogen atoms but is unimportant for helium. Atom loss occurs due to ionization by charge exchange with the solar wind ions, solar EUV photoionization, and collisions with solar wind electrons, the latter process being important only close to the sun ( $<1 \text{ AU}$ ).

A concept of interstellar hydrogen and helium atom penetration of the heliosphere is supported by extensive experimental observations. The techniques to study interstellar gas include observation of interplanetary glow (resonant scattering of the solar radiation in H I 1216 Å and He I 584 Å lines),<sup>141–144,158–162</sup> detection of pickup ions in the solar wind,<sup>163–166</sup> direct detection of interstellar helium flux,<sup>153,154</sup> and astronomical observations of the nearby interstellar medium.<sup>151,152,167,168</sup> An important minor heliospheric constituent, oxygen, can be from interstellar<sup>169,170</sup> and magnetospheric<sup>157</sup> sources. The number density of interstellar neutrals filling the heliosphere is in the  $0.01\text{--}0.1 \text{ cm}^{-3}$  range.

Another source provides neutral gas in the sun’s immediate vicinity ( $<0.5 \text{ AU}$ ). Interplanetary space is filled with a population of interplanetary, or zodiacal dust that tends to congregate toward the sun due to the Poynting–Robertson effect. The surface layer ( $<500 \text{ Å}$ ) of the dust grains is quickly saturated by the bombarding solar wind ions, which leads to desorption of neutral atoms and molecules from the surface to maintain equilibrium.<sup>12,142,171–173</sup> The estimates of this neutral particle source suffer from a large uncertainty in the dust population and details of the outgassing process, but the neutral particle number density is unlikely to exceed  $0.01 \text{ cm}^{-3}$ .

## 2. Interstellar gas (ISG) ENA fluxes

Neutral interstellar gas (ISG), which serves as a background gas for ENA-producing charge-exchange collisions in the heliosphere, can be directly detected by ENA instruments. Fluxes of interstellar atoms can thus be called ISG ENA fluxes. Direct detection of ENA fluxes of interstellar helium atoms accelerated by the solar gravitation was recently demonstrated for the first time by the GAS experiment on the Ulysses spacecraft.<sup>153,154,174–176</sup> The helium flux is  $10^4\text{--}10^5 \text{ cm}^{-2} \text{ s}^{-1}$  with atom energies in the  $30\text{--}100 \text{ eV}$  range.

Different radiation pressures and ionization rates lead to differences in properties of interstellar atoms in the heliosphere. In particular, different interstellar species would have different fluxes and velocity distribution functions at the same observation point.<sup>10</sup> Expected fluxes of interstellar neutrals at 1 AU vary from  $10^4 \text{ cm}^{-2} \text{ s}^{-1}$  down to  $10^{-1} \text{ cm}^{-2} \text{ s}^{-1}$  and their velocities vary from 10 to 70 km/s for an observer moving with the earth along its orbit around the sun (orbital velocity of the earth is  $\sim 29.8 \text{ km/s}$ ). The Ulysses instrument GAS is not capable of mass identification, but an alternative detection technology based on surface conversion to negative ions would be capable of ISG ENA mass analysis.<sup>10,177</sup> Thus direct *in situ* measurement of inter-



stellar hydrogen, deuterium, and oxygen atoms is possible at 1 AU but has not been realized yet. An accurate direct measurement of the interstellar deuterium-to-hydrogen ratio may potentially provide important constraints on Big Bang cosmology, and oxygen is important to the theory of stellar formation and evolution.<sup>10</sup>

### 3. Neutral solar wind (NSW) flux

The understanding of the heliosphere penetration by interstellar neutrals<sup>158</sup> led to the development of a concept of a permanently existing neutral component in the solar wind. This neutral solar wind (NSW) is believed to be born in charge exchange between the solar wind ions and interplanetary neutrals.<sup>178</sup> Solar wind plasma recombination contributes only a small fraction to the neutral component.<sup>12,142,179</sup> The NSW atoms move in the antisunward direction with approximately a solar wind velocity (300–800 km/s). At 1 AU, NSW consists of neutral hydrogen and helium atoms with an estimated flux of  $10^3$ – $10^4$  cm<sup>-2</sup> s<sup>-1</sup> depending on the observer position at the earth's orbit.<sup>12</sup> The NSW constitutes a  $10^{-5}$ – $10^{-4}$  fraction of the solar wind at 1 AU. As the solar wind expands toward the boundaries of the heliosphere, the NSW fraction would increase to 10%–20% and play an important role in the shaping the global heliosphere.<sup>149,180</sup> The NSW flux may be significantly larger when relatively cold solar material is occasionally ejected from the sun in the coronal mass ejection events.

Due to the earth's orbital motion, the NSW flux would be seen as coming from the direction several degrees off the sun for an observer moving with the earth.<sup>181,182</sup> Detailed computer simulations show that the NSW flux is confined within a few degree field-of-view (FOV).<sup>183</sup> An experiment to measure NSW was prepared in the early 1980s, but not flown yet.<sup>182</sup>

### 4. Low-energy heliospheric ENAs

If the supersonic flow of the solar wind plasma terminates at a solar wind shock front (TS), the plasma flow kinetic energy is largely converted into thermal energy of the subsonic plasma (Fig. 7). There is a certain probability for hot ( $T > 100$  eV) protons of the postshock solar wind plasma to charge exchange on background ISG between the termination shock and the heliopause and give rise to creation of fast hydrogen atoms. These atoms, called low-energy heliospheric ENAs, were predicted<sup>184,185</sup> in 1963; their characteristics were studied theoretically<sup>9,129,142,186–188</sup> but never explored experimentally.

Low-energy heliospheric ENAs are probably the only messengers born beyond the solar wind termination shock capable of reaching the inner solar system with minimal changes. The expected ENA flux is highly anisotropic: the flux increases with the decrease of distance from the shock to the sun, and the intensity and energy distribution of ENAs are very sensitive to the details of the interaction of the solar wind with the LISM, the parameters of the LISM, and the characteristics of the distant solar wind.<sup>9</sup> For a termination shock at 80 AU from the sun, the total expected ENA flux is  $200$  cm<sup>-2</sup> s<sup>-1</sup> sr<sup>-1</sup> from the upwind direction, and atoms are

in the energy range 100–800 eV. The ENA flux smoothly changes with the angle of observation, decreasing by a factor of 2 at 40° from the upwind direction.<sup>9</sup>

The strong dependence of ENA characteristics on the heliospheric properties makes ENA measurement an ideal direct method to remotely study the distant boundaries of the heliosphere.<sup>9</sup> Only a remote technique can provide a global view of the structure and dynamics of the heliosphere. The heliosphere ENA imaging will become especially important when a Voyager 1 spacecraft one day crosses the termination shock. Voyager *in situ* measurement will allow “calibration” of the remote observations in one point-direction: the measurements of low-energy heliospheric ENAs would reliably establish the shape of the heliosphere on the basis of the distance to the termination shock to be determined by Voyager 1. The next opportunity to obtain data from the heliospheric interface by *in situ* measurements from another spacecraft (planned Interstellar Probe) may not come earlier than year 2020.

### 5. High-energy heliospheric ENAs

Space plasma in the heliosphere and at its boundary is not in equilibrium and different processes result in distinctive populations of highly energetic ions, which, after charge exchange, would produce high-energy heliospheric ENAs (from 10 keV up to  $> 1$  MeV).

Heliospheric neutrals are ionized and picked up by the solar wind flow. After reaching the termination shock these pickup ions are believed to be accelerated to high energies and can reenter the heliosphere as cosmic rays, conventionally called anomalous cosmic rays (ACRs).<sup>189</sup> Charge exchange of ACR ions produces ENAs whose detection would reveal details of ACR production and acceleration at the heliospheric boundary.

Shocks in plasma efficiently accelerate ions to high energies.<sup>190,191</sup> Various shocks travel through the heliospheric plasma and serve a source of energetic ions and correspondingly high-energy ENAs. Complex shock structures in the solar wind include merged interaction regions (MIRs) and corotating interaction regions (CIRs). High-energy heliospheric ENAs are generated by charge exchange of ACR ions, MIR, and CIR shock-accelerated ions, quite-time interplanetary ions (QTIP), and energetic solar particles (ESPs).<sup>6,8,11</sup> Computer simulations predict complicated dependence of ENA characteristics on the direction of observation;<sup>6,8</sup> upper limits of ENA fluxes do not exceed  $10^{-2}$ – $10^{-3}$  cm<sup>-2</sup> s<sup>-1</sup> sr<sup>-1</sup> keV<sup>-1</sup> and decrease with increasing atom energy. Theoretical models predict the maximum of the ACR-produced high-energy ENA fluxes from the heliospheric tail (downwind) region,<sup>192</sup> which is exactly opposite to the direction where the maximum low-energy ENA flux is expected. The analysis of the experimental data from the CELIAS instrument<sup>49</sup> on the SOHO spacecraft may produce first experimental data on high-energy heliospheric ENAs in the near future.<sup>193</sup>



### III. BRIEF HISTORY OF EXPERIMENTAL STUDY OF ENAS IN SPACE

While there are a number of publications on different aspects of the history of solar-terrestrial and magnetospheric physics,<sup>65,66,194–198</sup> the story of ENA experimental study has never been told in detail. The presence of ENAs in the terrestrial environment was reliably established for the first time in 1950 by optical recording of Doppler-shifted hydrogen Balmer H $\alpha$  emission (6563 Å) in an aurora.<sup>199,200</sup> The precipitating hydrogen ENAs are born in the charge exchange between energetic protons and neutrals of the upper atmosphere and exosphere. Balmer H $\alpha$  emission is in the visible wavelength range. It can be optically detected from the ground, and auroral emissions were extensively used to study the characteristics of energetic particles.<sup>194,201</sup> While hydrogen Balmer lines were observed in the auroral regions since the late 1930s,<sup>202</sup> it was not until 1950 that a Doppler-shifted H $\alpha$  line was unambiguously explained with the presence of hydrogen ENAs.<sup>199</sup>

The importance of ENA production processes for the magnetosphere was understood<sup>203</sup> by noting that the proton–hydrogen atom charge exchange cross section was rather high for collision velocities less than the electron velocity in a Bohr orbit, i.e., for protons with energies <25 keV (Fig. 2). Charge exchange determines many important properties of geomagnetic storms. The “main phase” of a geomagnetic storm may last from 12 to 24 h, and it is characterized by a weakening of the geomagnetic field. The main phase is usually followed by a “recovery phase,” when a gradual field recovery toward the initial undisturbed value of the geomagnetic field is observed. The recovery time constant may be 1 day or sometimes longer.

It was suggested for the first time in 1959 that charge exchange between the magnetic storm protons and neutral atmospheric hydrogen atoms provided the mechanism for the recovery phase.<sup>77</sup> The charge exchange process leads to the production of fast hydrogen atoms and observation of such atoms was first proposed in 1961 as a tool to study the proton ring current present during a magnetic storm.<sup>78</sup> A source of ENAs beyond the magnetospheric boundary, viz., charge exchange between the solar wind and the escaping hydrogen geocorona, was also identified for the first time.<sup>78</sup> The concept of imaging the magnetospheric ring current in ENA fluxes from outside<sup>13</sup> and, “in a limited fashion,” from inside<sup>14</sup> was introduced much later in 1984.

The presence of atomic hydrogen in interplanetary space was first derived<sup>185</sup> in 1963 from sounding rocket measurements<sup>204</sup> of Doppler-broadened hydrogen Ly- $\alpha$  (1216 Å) radiation (see also review of the early study of extraterrestrial Ly- $\alpha$  radiation<sup>205</sup>). It was recognized since the late 1950s that Doppler shift measurements could distinguish between the telluric (geocorona) and interplanetary hydrogen.<sup>206</sup> The emerging concept of the heliosphere<sup>184</sup> was extended in 1963 by the suggestion that about half of the solar wind protons would reenter the solar cavity in the form of hydrogen ENAs (with 3/4 of the initial solar wind velocity) as a result of processes at and beyond the solar wind termination region.<sup>185</sup> It was established later that an interplanetary glow in the hydrogen and helium resonance lines

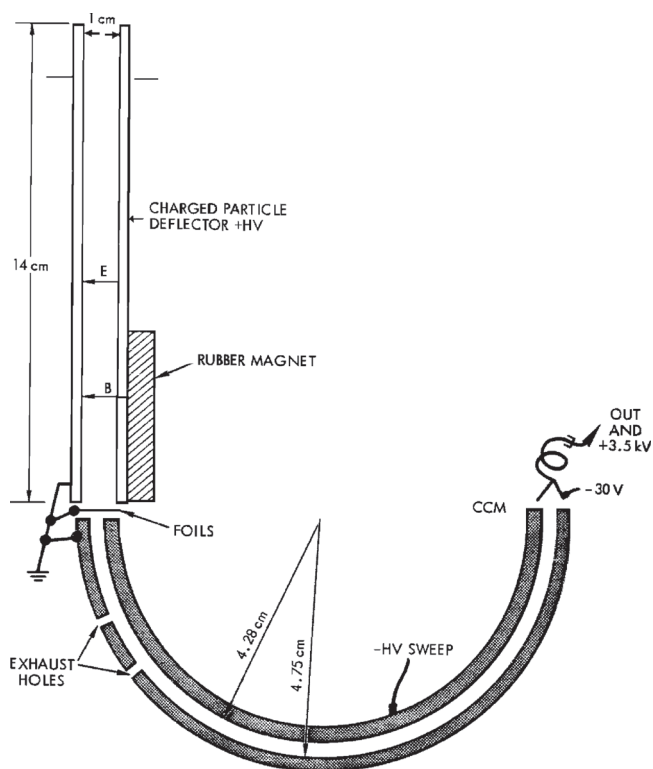


FIG. 8. Schematic representation of the first ENA instrument flown on a sounding rocket in 1968. The instrument consists of charged particle deflector, ultrathin carbon foil, electrostatic analyzer, and ion detector. (After Ref. 212).

was produced by resonant scattering of the solar radiation by interstellar gas directly entering the solar system.<sup>141–144,158–161</sup> The “returning” neutral solar wind flux<sup>185</sup> is believed to be significantly smaller and highly anisotropic.<sup>9</sup>

It was also suggested in the early 1960s that a large number of neutral atoms could be present in the solar wind as transients due to ejection of solar matter in violent events.<sup>207,208</sup> Neutral hydrogen atoms in solar prominences are observed optically, and it was argued that they may reach 1 AU. The follow-on calculations<sup>209,210</sup> showed that most of the neutral atoms would not survive travel to 1 AU because of ionization by solar EUV radiation and electron collisions. The neutral component of the solar wind is born mostly in charge exchange between the solar wind ions and interstellar gas filling the heliosphere.<sup>12,142,178</sup>

Direct ENA measurements promised exceptional scientific return, but the necessary instrument development was only started in the late 1960s by Bernstein and co-workers<sup>119,211–213</sup> at TRW Systems Inc., Redondo Beach, California. Direct, *in situ* measurement of ENA fluxes in space was first attempted on April 25, 1968 in a pioneer rocket experiment.<sup>119</sup> The first dedicated ENA instrument was launched on a Nike–Tomahawk sounding rocket from Fort Churchill, Manitoba, Canada. This experiment was followed by the launch of a similar instrument on a Javelin sounding rocket on March 7, 1970 to an altitude of 840 km at Wallops Island off the coast of Virginia.<sup>214</sup> The experiments detected hydrogen ENA fluxes in the range  $10^5$ – $10^9$  cm<sup>-2</sup> s<sup>-1</sup> sr<sup>-1</sup> with energies between 1 and 12

keV. The reported ENA fluxes were considered by many as excessively high, however these results have never been directly challenged in the literature.

The first ENA instrument<sup>212</sup> is shown in Fig. 8. It had many features and introduced many components and techniques that would later on become widely used by various modern ENA instruments. The instrument was based on foil-stripping of ENAs and subsequent analysis of the resulting positive ions. Electrostatic deflection plates were used to remove incident protons and electrons with energy  $< 25$  keV at the entrance (the instrument also had an additional 100 G magnetic field to remove electrons with energies  $< 50$  keV). The deflection plates served to define the solid angle of the instrument. ENAs were stripped passing an ultrathin ( $2 \mu\text{g}/\text{cm}^2$ ) carbon foil mounted on an 80% transparent grid. A hemispherical energy analyzer, which focused the ions in one dimension, was used for energy analysis. The stripped ENAs, protons, in a selected energy range, passed through the analyzer and were counted by a channel electron multiplier (CEM). Use of two additional identical instrument sections without deflecting voltage and without an ultrathin foil allowed the simultaneous measurement of proton fluxes and the monitoring of the background count rate during the experiment, respectively.

An attempt to measure ENAs was made in the RIEP experiment (a Russian acronym for “registerer of intensity of electrons and protons”) on the Soviet Mars-3 interplanetary mission (launched May 28, 1971; entered low Mars orbit on December 2, 1971). The experiment was designed to measure the energy distribution of plasma ions and electrons in the Mars’ environment as well as in the solar wind during interplanetary coast. The RIEP instrument consisted of eight separate cylindrical electrostatic energy-per-charge analyzers, each followed by a CEM to count particles.<sup>215</sup> Each analyzer unit was designed to measure charged particles of a selected energy-per-charge ratio. Two ultrathin carbon foils ( $150 \text{ \AA} \approx 3.5 \mu\text{g}/\text{cm}^2$ ) were installed in front of two of the eight analyzers. A comparison of count rates from analyzers with and without foil while measuring particles with the same energy-per-charge ratio was expected to provide information on high-intensity neutral atom fluxes. No charged particle deflectors were used in front of the ultrathin foils, and the experiment failed to establish ENA fluxes, which are usually relatively weak.

Another ENA instrument, a slotted-disk velocity selector, was successfully built and mechanically and electrically tested in a rocket flight in 1975.<sup>181</sup> This narrow (FOV) instrument, which demonstrated efficient rejection of charged particles and photons, was especially suitable for measurement of ENAs with velocities  $< 500$  km/s ( $E < 1.3$  keV/nucleon). It is interesting (see below) that measurements of the interstellar helium flux and of the neutral component in the solar wind were considered as possible applications.<sup>181</sup> Apparently due to large size, mass, and power consumption as well as the torque exerted on a spacecraft (the instrument included at least two disks 16.24 cm in diameter on a shaft 74 cm long spinning at  $4.5 \times 10^4$  rpm) this instrument was never used for ENA measurements, and the technique development was discontinued.

The interest to the concept of a mechanically moving ENA velocity selector was recently revived by suggestion to use unconventional high-frequency mechanical shutters mounted on ceramic piezoelectric crystals.<sup>216</sup> Such an approach seems to be especially promising for the study of low-energy ENAs, but further development is needed to demonstrate its feasibility.

The initial ENA measurements<sup>119,214</sup> were not repeated and/or independently verified, and they were largely ignored by the space community. Exceptionally strong EUV/UV radiation background was identified as a major obstacle for reliable ENA measurements in space, and experimental difficulties were perceived as insurmountable by many at that time.

Three groups accepted the experimental challenge and continued independent development of dedicated ENA instrumentation in the late 1970s. A group at the Max-Planck-Institute for Aeronomy (MPAe), Lindau, Germany targeted direct *in situ* detection of interstellar helium flowing into the solar system.<sup>174,175</sup> (The experiment was suggested for the first time in 1972 in a proposal by H. Rosenbauer, H. Fahr, and W. Feldman). Another group at the Space Research Institute (IKI), Moscow, USSR, planned to measure the neutral component in the solar wind and heliospheric ENAs.<sup>177,182,217</sup> It is interesting that the Moscow group initially considered also direct, *in situ* detection of the interstellar helium flux<sup>218</sup> but ultimately decided to concentrate on the neutral solar wind (NSW) and heliospheric ENAs. The NSW experiment was actively supported by a group at Space Research Center in Warsaw, Poland, which also theoretically studied heliospheric ENAs and ENAs produced in the giant-planet magnetospheres.<sup>219–221</sup> A third group at the University of Arizona focused on the possibilities of measuring ENAs in geospace.<sup>222</sup>

The GAS instrument<sup>175</sup> to directly detect fluxes of interstellar helium ( $E = 30\text{--}120$  eV) had a dramatic history of being completely redesigned and built within a record 3 month period in an “almost super-human effort,”<sup>176</sup> which had become necessary to realize the original experimental concept on the European-built Ulysses probe after cancellation of the U.S. spacecraft. The GAS was then successfully flown<sup>153,154,176</sup> on Ulysses which was launched in 1990 after many delays,<sup>223</sup> including the one caused by the Space Shuttle *Challenger* explosion. The neutral helium instrument is based on secondary ion emission from a specially prepared surface.<sup>175,176</sup> The experiment has produced unique data on interstellar helium characteristics and ENAs emitted from Jupiter’s Io torus and continues operating successfully.<sup>154</sup>

A new ultrathin-foil based “direct-exposure” technique, which does not require stripping of incoming ENAs, was developed by the Moscow group to detect the neutral solar wind.<sup>177,182,217</sup> NSW measurements can be performed from an interplanetary or high-apogee earth-orbiting spacecraft by pointing the instrument several degrees off the sun. The possibility of taking advantage of the aberration caused by the earth’s motion around the sun was first suggested in 1975<sup>181</sup> and was independently “rediscovered” later.<sup>177,182</sup>

The NSW instrument was built for the Soviet Relikt-2 mission which was originally planned to be launched in

1987.<sup>182</sup> The initial experiment also included measurements of ENAs from the heliospheric interface and ENAs emitted from the terrestrial magnetosphere. Detection of ENAs escaping Jupiter and Saturn was also expected.<sup>182,220,224</sup> The Relikt-2 mission was postponed many times, and is still awaiting launch (now scheduled for 1999).

The NSW instrument included a diffraction filter<sup>182,225</sup> to significantly increase the ENA-to-EUV/UV photon ratio in the sensor. The filter was optional for the planned measurements,<sup>182</sup> and it was not fully developed, when the instrument was built. A new diffraction filter technology is emerging,<sup>226,227</sup> and a new generation of diffraction filters for ENA instruments is currently being developed and evaluated (see Sec. VI F).<sup>228–231</sup> An introduction of the diffraction filters opens the way to take full advantage of a highly efficient direct-exposure technique.

ENA instrument development in the late 1970s and early 1980s did not attract much attention in the space community, and did not enjoy enthusiastic support of the funding agencies. However, the importance of ENAs for mass, energy, and momentum transport in space was established and new opportunities offered by remote ENA imaging in separating spatial variations from temporal ones in space plasmas were gradually recognized.

Several measurements of large fluxes of ions ( $E < 10$  keV) near the equator at altitudes below 600 km had been reported since the early 1960s.<sup>232</sup> Fluxes of high-energy ions ( $0.25 < E < 1.5$  MeV) were measured later at low altitudes by the German AZUR spacecraft,<sup>124,233</sup> and the ions with energies down to 10 keV were detected there in 1973.<sup>234</sup> Theoretical calculations predicted a short lifetime for such low altitude protons near the equator due to collisions with atmospheric particles. The proton loss thus required an injection of protons in a limited region below 600 km. The required proton source to compensate proton loss due to interaction with atmosphere must also be atmosphere dependent. The explanation, found in 1972,<sup>124</sup> suggested that trapped energetic ions in the ring current at much higher altitudes produce ENAs in charge exchange, and a fraction of these ENAs reaches low altitudes where they are re-ionized by charge exchange and are consequently trapped by magnetic field (Fig. 6).

In the heliosphere, the neutral solar wind is believed to provide a transport mechanism similar to that of magnetospheric ENAs.<sup>180</sup> As the solar wind expands toward the boundaries of the heliosphere, the neutral fraction in the solar wind gradually increases to 10%–20% at the termination shock (Fig. 7). While the solar wind plasma flow is terminated by the shock, the solar wind ENAs easily penetrate the region of the heliospheric interface and enter the LISM, sometimes called “very local” interstellar medium (VLISM.) The solar wind ENAs thus interact with the approaching local interstellar plasma via charge exchange with plasma protons. Hence, the boundary of the region of the sun’s influence, the solar system “frontier,” extends further into “pristine” interstellar medium. The significance of this neutral solar wind effect<sup>180</sup> on LISM was recently confirmed by detailed computer simulations of the heliospheric interface.<sup>149,150</sup>

The interest in ENA characteristics and instrument development began to grow after the serendipitous discovery of ENAs made by energetic particle instruments on several spacecraft. Energetic particle instruments are usually based on solid state detectors and often capable of discriminating against electrons. However, such instruments generally cannot distinguish between a charged particle and an ENA. Therefore an energetic particle detector would efficiently serve as an ENA detector only in the absence of the normally abundant ions. Only high-energy ENAs ( $E > 10$ –20 keV/nucleon) can be detected by such instruments.

Analysis<sup>235</sup> of inconsistencies in interpretation of energetic particle measurements by the IMP 7 and 8 satellites (at  $\sim 30$ –35  $R_E$  from the Earth) led to the conclusion that a certain fraction of counts during periods of very low fluxes<sup>236</sup> was caused by radiation belt-produced ENAs with energies 0.3–0.5 MeV.

Both energetic ions and neutrals were detected during the magnetic storm in 1982 by the SEEP instrument on the S81-1 spacecraft at low altitude. A double charge-exchange mechanism (Fig. 6) was invoked to explain the observations, and it was also suggested that measurements of energetic neutral atoms at low altitude “might be able to image, in a limited fashion, the integral ion intensities of the ring current as a function of latitude and longitude.”<sup>14</sup>

ENA fluxes of nonterrestrial origin were detected on a Voyager 1 spacecraft during flybys of Jupiter<sup>237</sup> and Saturn<sup>238</sup> in March 1979 and November 1980, respectively. The low energy charged particle (LECP) instrument on Voyager-1 included a silicon detector to accumulate counts from eight separate directions in the ecliptic plane.<sup>239</sup> The detector was designed to measure ions (electrons were swept away by magnetic field) with energies  $> 40$  keV.

During the approach to Jupiter, when Voyager 1 was still outside the gigantic Jovian magnetosphere, an excess count rate was measured in the sector containing the planet in its FOV. The detector characteristics limit the possible sources of the excess counts to energetic ions, x rays, and ENAs. No energetic ion fluxes with required intensity and energy were expected at the location of measurements since there were no magnetic field lines connecting to Jupiter.<sup>237</sup> It is known that x rays can be generated in planetary magnetospheres by precipitating energetic electrons, usually in polar regions. Consideration of x-ray generation showed that the required fluxes of electrons were several orders of magnitude higher than those found in the Jovian magnetosphere. The conclusion of data analysis was that “the only remaining possibility of explaining the excess counts ... is energetic neutral atoms.”<sup>237</sup> The energy dependence of the observed ENA spectra was similar to the one established for energetic ions in the magnetosphere during the close flyby.

A similar excess count rate was measured one and a half years later during the flyby of Saturn.<sup>238</sup> Here again the observed count rate, if interpreted in terms of x rays, cannot be reasonably related to precipitating magnetospheric electrons. It was concluded that “charge exchange of energetic ions with satellite tori is an important loss mechanism at Saturn as well as at Jupiter.”<sup>238</sup>

Possible ENA signatures in the experimental data ob-



tained by energetic particle instruments<sup>240</sup> on IMP 7,8 and ISEE 1 were analyzed in 1982.<sup>241,242</sup> Detection of ENAs ( $E \sim 50$  keV) was unambiguously established, and their source was identified as the ring current in the terrestrial magnetosphere.<sup>107</sup> Coarse spatial information on ENA-producing regions was derived and ENA energy distribution and mass composition were determined. The ENA measurements were made from positions where magnetic field lines allowed only negligible fluxes of energetic ions, so that the detectors counted only ENAs. The analysis<sup>107</sup> of these measurements was a major milestone in validating the idea that the global magnetospheric processes can be efficiently studied remotely by measuring ENAs. It was also suggested that ENA imaging could be used to study the magnetospheres of Jupiter and Saturn.<sup>107</sup>

The follow-on analysis of the ISEE 1 data demonstrated the powerful potential of the ENA detection as an imaging technique by reconstructing the first ENA global image of the storm-time ring current (at  $E \sim 50$  keV).<sup>79</sup> The instrument<sup>240</sup> on ISEE 1 was capable of measuring the incoming ENA flux, and imaging was performed by a combination of spacecraft spin and instrument axis scanning by a moving motorized platform. A procedure for computer simulation of all-sky ENA images was established and the theoretically predicted images were compared with the ring current image obtained by ISEE 1 at a radial distance of  $2.6 R_E$  during a 5 min observation.

The analysis of excessive count rates<sup>237,238</sup> detected by Voyager 1 during Jupiter and Saturn flybys allowed one to determine some ENA characteristics in the vicinity of the giant planets.<sup>108</sup> Further computer simulations of expected ENA emissions demonstrated the efficiency of ENA imaging as a tool to study the magnetospheres of Jupiter and Saturn from flyby spacecraft and orbiters.<sup>109,110,224,243</sup>

Use of energetic particle instruments for detection of high-energy ENA fluxes in the absence of ions became an established experimental technique. The storm-time ENA images of the polar cap<sup>244</sup> were recently obtained by the CEPPAD experiment<sup>245</sup> on the POLAR spacecraft. The instrument cannot distinguish between ions and neutrals, and the ENA images were recorded during the portions of the spacecraft orbit where the fluxes of the charged particles were very low.

An instrument with a dedicated high-energy ENA ( $20 < E < 1500$  keV) detection channel was flown on the CRRES satellite in 1991.<sup>21,125</sup> The neutral channel that consisted of a magnetic deflector followed by a solid-state detector measured ENA fluxes precipitating to low altitudes at the equatorial regions. A small geometrical factor put limit to the imaging capabilities of the instrument. A conceptually similar ENA instrument was recently flown on ASTRID.<sup>22,23</sup> A more sophisticated high energy particle (HEP) instrument (10–100 keV ENAs) was launched on the GEOTAIL spacecraft in 1992.<sup>20</sup>

The current phase in the study of ENAs in space plasmas is characterized by extensive computer simulations of ENA images, novel instrument development, and the preparation and planning of a number of dedicated ENA space experiments. The concept of global ENA imaging of the magneto-

sphere is firmly established.<sup>1–5,100,111,112</sup> Computer simulations of low-energy<sup>113–115</sup> and high-energy<sup>111,116,118,246,247</sup> ENA imaging emphasized the importance of ENA measurements throughout a wide energy range from few eV up to several hundred keV. Various aspects of heliospheric ENA global imaging were theoretically studied for various species and energy ranges.<sup>6–12,157,192,248</sup>

The first ENA detections obtained from planetary magnetospheres in the early 1980s triggered new interest in developing dedicated ENA instrumentation: various techniques for detection and imaging of low- and high-energy ENAs were proposed and their laboratory evaluation was begun.<sup>243,249–254</sup> Several new research groups have entered the ENA-imaging field since then and significant improvements of the known experimental techniques as well as a number of innovative approaches were proposed, especially for low-energy ENAs.<sup>4,10,125,216,225,228–230,254–258</sup>

NASA recently selected an IMAGE mission to perform comprehensive imaging of the terrestrial magnetosphere in EUV, FUV, and ENA fluxes. A sophisticated first large size ENA camera INCA<sup>24</sup> on Cassini will soon perform ENA imaging of the Saturnian magnetosphere and the exosphere of the Saturnian moon Titan.<sup>259</sup>

## IV. ENA IMAGING

### A. ENA imaging concept and major instrument requirements

An energetic ion gyrates about a magnetic field line in space (Fig. 3). When charge exchange occurs, the resulting ENA is liberated from the magnetic field and, as a stone from a slingshot, it moves straight away from the point of its birth. Reconstruction of a global ENA image requires measuring ENA flux dependence on the direction of observation: the instrument has ideally to determine the trajectory (flight direction) of each individual ENA, identify its mass and energy, and accumulate the image in the memory. A sequence of ENA images (for different masses and energies) would allow direct observation of global plasma dynamics, e.g., development and decay of a ring current during magnetic storms and variation of the heliosphere's size and shape during the solar cycle.

Some plasma ions, for example  $\text{He}^+$  and  $\text{O}^+$ , can be imaged optically by registering resonantly scattered solar photons at  $\lambda = 304$  and  $834$  Å, respectively.<sup>246,247,260–263</sup> Unlike  $\text{He}^+$  and  $\text{O}^+$ , protons, the most abundant component of space plasmas cannot be imaged optically, which makes ENAs in many cases the only tool to study processes of interest remotely. ENA imaging, complemented when possible by imaging in the EUV<sup>5,247,264</sup> and FUV<sup>264,265</sup> spectral ranges as well as x-ray imaging<sup>266,267</sup> and radio sounding,<sup>268</sup> promises a breakthrough in our understanding of plasma processes in and dynamics of the magnetosphere and heliosphere. (Feasibility of locating and monitoring the position of the earth's magnetopause and plasmopause by a radio wave sounder from a high-altitude satellite is presently being intensely debated.<sup>268–271</sup>)

An ENA instrument ideally has to perform the following specific functions:



- (1) to prevent charged particles from entering the instrument;
- (2) to suppress background EUV/UV radiation;
- (3) to identify the incoming ENAs (i.e., to determine mass and energy);
- (4) to determine trajectories of the incoming ENAs (imaging); and
- (5) to provide a dynamic range covering ENA fluxes from  $10^{-3}$  to  $10^5 \text{ cm}^{-2} \text{ s}^{-1} \text{ sr}^{-1}$  in the energy range from a few eV up to  $>100 \text{ keV}$ .

An instrument deflector-collimator would define the FOV and prevent ions and electrons from entering the instrument. The required mass resolution is usually modest: to distinguish among hydrogen (1 amu), helium (4), and oxygen (16) atoms. One can also expect sulfur (32) ENAs in the Jupiter's magnetosphere.

ENA images can be obtained either from a three-axis stabilized spacecraft or from a spinning spacecraft. The requirements of ambient ion deflection favor a slitlike instrument aperture for imaging in one dimension only (Sec. VI B). The imaging in the second dimension can be obtained by using spacecraft spinning. In that case one records one-dimensional images for consecutive orientations of the spacecraft, which may be only a few degrees apart, as the spacecraft spins about its axis (instantaneous orientation, or attitude, of a spacecraft is usually known with high precision). A two-dimensional composite image is then reconstructed from a set of one-dimensional images. A one-dimensional imager on a spinning platform has become a favorite configuration for ENA experiments.

## B. EUV/UV background radiation

Background EUV/UV photons may trigger MCP detectors in ENA instruments either directly or via photoelectron emission from foils and other exposed surfaces. The spectral range of concern is usually limited to wavelengths  $\lambda < 1400 \text{ \AA}$ . An exposure to direct solar light will "blind" and may permanently damage an unprotected instrument. A special photometric unit,  $1 \text{ R} = 1 \text{ Rayleigh} = 10^6/4\pi \text{ cm}^{-2} \text{ s}^{-1} \text{ sr}^{-1}$ , is used to describe diffuse photon fluxes. If one applies the same unit to neutral particle fluxes, then an ENA flux of  $1 \text{ cm}^{-2} \text{ s}^{-1} \text{ sr}^{-1}$  would correspond to  $\sim 10^{-5} \text{ R}$ . Thus the expected magnetospheric and heliospheric ENA fluxes are in the  $10^{-8}$ – $1 \text{ R}$  range.

A strong background EUV/UV radiation makes space an exceptionally inhospitable place for ENA measurements. The major EUV/UV source in the magnetosphere is the dayglow at the sunlit side and the nightglow at the night side. The glow arises from scattering of sunlight (including multiple scattering of photons in sometimes optically thick environment) and emission associated with various collisional processes in the upper atmosphere, exosphere, and ionosphere.<sup>17,19</sup> Typical dayglow and nightglow spectra contain a number of EUV and UV spectral lines.<sup>272,273</sup> At 600 km altitude, the total dayglow intensities are 54 kR and 25 kR for observations down and up, respectively.<sup>272</sup> The most prominent lines are hydrogen H I 1216 Å and oxygen O I 1304 Å with significant contribution of other helium, oxy-

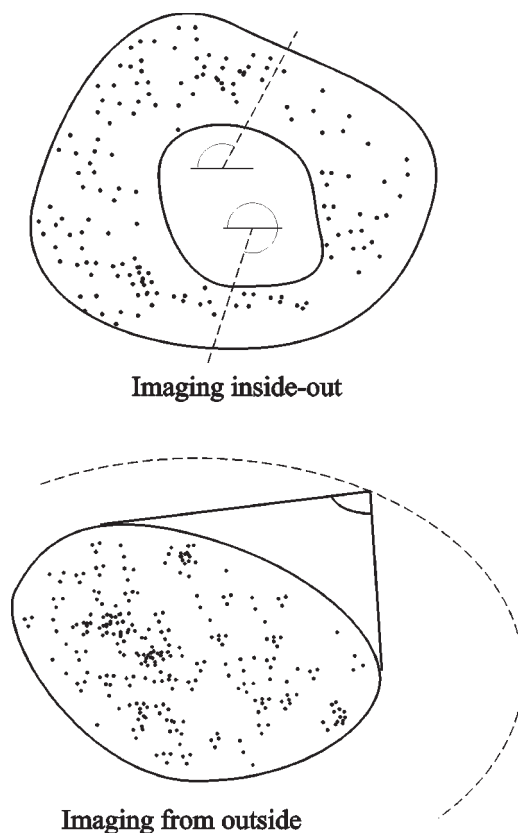


FIG. 9. Two imaging geometries: imaging from inside-out and imaging from outside.

gen, and nitrogen spectral lines. The most important spectral lines of nightglow are hydrogen H I 1216 Å and helium He I 584 Å.<sup>273</sup> The nightglow intensity is 3600 R, which is 4–11 orders of magnitude higher than expected ENA fluxes.

Interplanetary EUV/UV glow is produced by resonant scattering of solar radiation by heliospheric hydrogen and helium atoms. The glow brightness depends on the direction of observation and varies between 500 and 1000 R in H I 1216 Å and between 1 and 10 R in He I 584 Å at 1 AU.

## C. Imaging basics

An ENA image of a plasma object ideally consists of a set of images obtained for different particle masses (e.g., H, He, and O) in different energy ranges (e.g., 1–5, 5–10, and 10–20 keV, ...). ENA imaging thus includes two interrelated tasks, viz., obtaining the object's image and ENA identification (mass, energy, and velocity). We will consider these two tasks separately, and then demonstrate (Sec. VII) how they are combined in the instruments. The images of plasma objects can be obtained in two ways: observing an object from a remote vantage point outside (external imaging) and observing from within a plasma object, the inside-out internal imaging (Fig. 9). The ENA emitting plasma can be assumed to be "ENA-thin" with the exception of the measurements at low-earth orbit, where multiple charge exchange may become important.

Imaging from outside can be performed from a spacecraft flying by a planetary magnetosphere, or from a spacecraft in a high-apogee or high-altitude orbit. The high-apogee

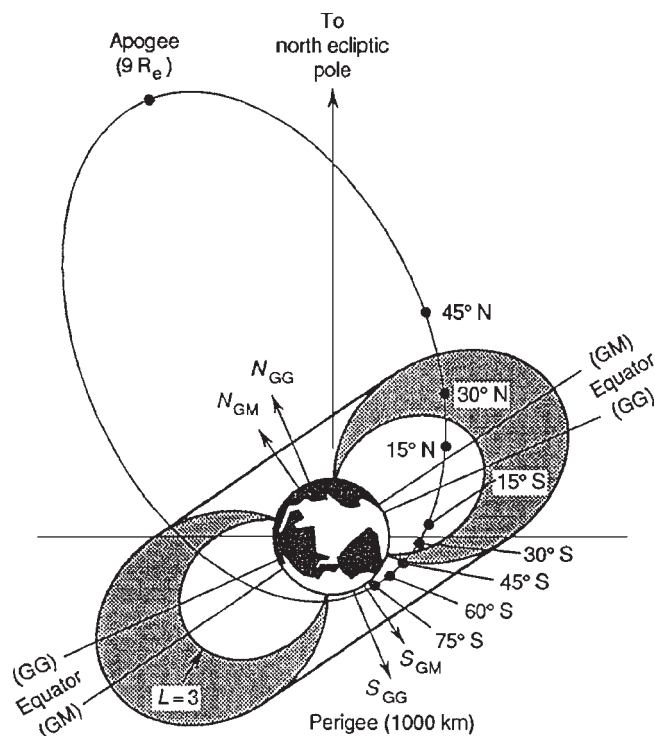


FIG. 10. imaging of the terrestrial magnetosphere from a hypothetical high-apogee polar orbit. Magnetic field lines crossing the magnetic equator at three and five earth radii ( $L=3,5$ ) are shown for reference. (After Ref. 5.)

configuration is illustrated in Fig. 10. The most advanced ENA imaging missions, such as Cassini at Saturn, utilize external outside viewing geometry. An example of the inside-out internal imaging is observation of the heliosphere (Fig. 7) from the earth's orbit and study of precipitating magnetospheric ENA fluxes (Fig. 6) at low-earth orbit. The measurements of the latter type were performed on CRRES<sup>21</sup> and ASTRID<sup>22,23</sup> missions.

The ENA flux  $j_{\text{ENA},i}(\text{cm}^{-2} \text{s}^{-1} \text{sr}^{-1} \text{keV}^{-1})$  of a given species  $i$  from a given direction  $\mathbf{s}$  (Fig. 11) is

$$j_{\text{ENA},i}(\mathbf{s}, E) = \int_{\mathbf{s}} j_i(\mathbf{s}, E) \sum_k [\sigma_{ik}(E) n_k(\mathbf{s})] \times \exp[-D(\mathbf{s}, E)] d\mathbf{s},$$

where  $j_i(\mathbf{s}, E)$  is the directional differential flux of parent ions,  $n_k(\mathbf{s})$  is the number density of neutral species  $k$  of the background gas,  $\sigma_{ik}(E)$  is the energy-dependent charge exchange cross section between ions of species  $i$  and neutrals of species  $k$ , the factor

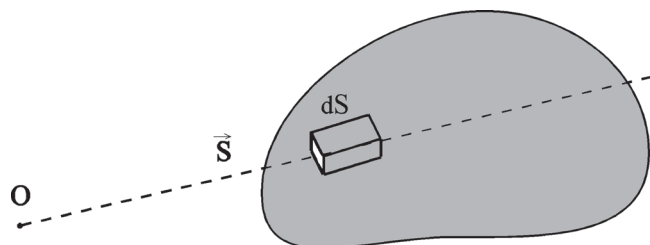


FIG. 11. Geometry of remote sensing of an ion population by measuring ENA fluxes from an observation point O.

$$D(\mathbf{s}, E) = \int \beta dt$$

allows for extinction of ENAs on their way from a point of birth to an observation point  $O$ , and  $\beta$  is the ENA loss rate (charge exchange, electron impacts, and photoionization). The ENA flux reaching the observer from a given direction is thus determined by an integral along the line-of-sight  $\mathbf{s}$  (Fig. 11), and the flux contains information on the velocity distribution function of ions along the line-of-sight.

An ENA image is reconstructed by measuring the ENA flux dependence on the direction of observation. The recording of ENA images is complicated by fast motion of the spacecraft and by differences in ENA velocities. The spacecraft motion puts the limit on possible image accumulation time, which may be in conflict with the desired statistical accuracy. The observer motion may also become advantageous if it allows derivation of the ENA velocities due to the aberration effect. For large distances between of the spacecraft and plasma object, high-velocity, and slower ENAs simultaneously emitted by the same plasma region would be detected at different times. This time difference varies from 1 to 15 min for earth magnetosphere imaging from a high-altitude spacecraft to more than a year for the imaging of the heliospheric boundary from 1 AU.

An ENA image is a projection of a three-dimensional ENA-emission plasma object on a two-dimensional image plane. The interpretation of images thus becomes model dependent. Image inversion is a specialized area<sup>1,2,5</sup> that is beyond the scope of this article. We only note that forward modeling is often used as a method of choice of treating ENA images, that is varying the free parameters to achieve the best fit of the model predictions to experimentally obtained images.<sup>1,2,5,79,116</sup> It is important that ion distribution functions may not be entirely independent in different magnetospheric regions. Energetic ion motion in the magnetosphere is constrained by magnetic field geometry, which allows one to relate ion characteristics in spatially separated areas. Significant progress was achieved in applying discrete inverse theory to optical geophysical images,<sup>264</sup> which may also be used for some aspects of ENA imaging. Inversion of ENA images requires accurate knowledge of the instrument characteristics such as the FOV and detection efficiencies. Future ENA experiments will also perform simultaneous observations from multiple spatially separated spacecraft to achieve tomographic imaging of planetary magnetospheres.

The ENA fluxes are usually weak and the observation time is limited. Consequently a number of counts in an image pixel is mostly small and, as a result, significant statistical noise due to the random nature of the particle flux is often experienced. This noise is present even in the absence of the detector intrinsic noise. The trade off between the observation time and the desired image angular resolution and "photometric" accuracy is one of the most important goals of the modeling of an ENA imaging experiment.

A weak ENA flux cannot be collected and concentrated by diffracting and/or refracting elements as it is done in optics. In this respect, ENA imaging is similar to hard x-ray imaging.<sup>274,275</sup> Reconstruction of the trajectories of indi-

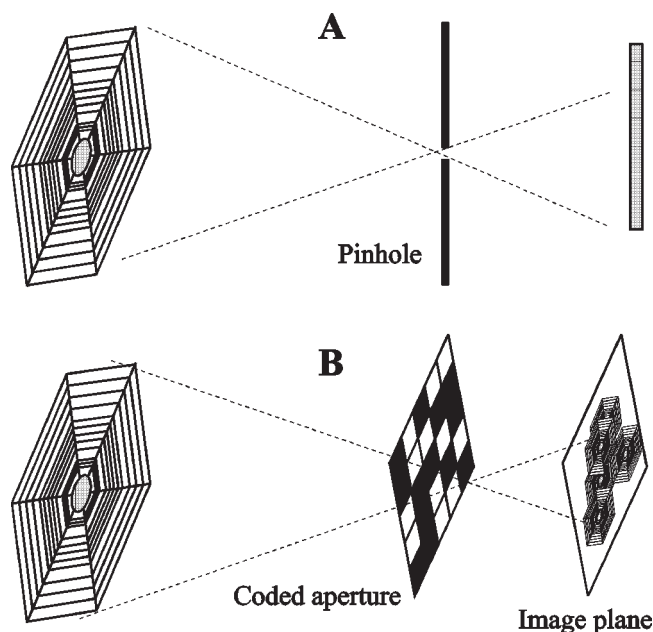


FIG. 12. Pinhole (A) and coded-aperture (B) imaging cameras.

vidual ENAs can be achieved by a two-point trajectory extrapolation, when the location of particle entry into the instrument is connected by a straight line with the point of ENA impact on the instrument “focal plane,” i.e., the plane where the ENA image is formed.

The point of ENA impact can be determined by a position-sensitive detector. The simplest way to determine the entry point is to restrict the entry area by a mechanical aperture: this is a pinhole camera [Fig. 12(A)]. In a one-dimensional imaging system a slit would play a role of a pinhole. Another approach is based on placing an ultrathin foil at the instrument entrance (see Sec. VI A) and determining the position of ENA entry by measuring electron emission from the foil caused by the passing ENA. Since an ENA flight direction may be changed in the foil passage (scattering), the latter configuration allows reconstruction of the ENA trajectory *inside* the instrument after the entrance foil.

While a simple pinhole camera can be used for ENA imaging in any energy range, thin-foil cameras are limited to high-energy ENAs. The direction of high-energy ENA arrival practically coincides with the particle trajectory inside the instrument, and the latter trajectory can be used for ENA image reconstruction. A low-energy ENA would significantly scatter in the foil. Consequently, the imaging in low-energy ENA fluxes requires a pinhole camera with a disadvantage of low instrument throughput. In the context of imaging, the division of particles in high-energy and low-energy ENAs depends on the foil thickness and the required angular resolution.

#### D. Coded aperture versus pinhole

A pinhole camera provides excellent imaging but requires relatively high ENA fluxes. ENA fluxes in space are weak, and an increase of the instrument’s geometrical throughput, or geometrical factor, is of paramount importance. The greater the desired angular resolution, the smaller

the pinhole should be for the same area of the image in the focal plane. The speed of the image forming system may not suffice to produce an image of the desired photometric quality during a given exposure time. The situation may be also aggravated by the detector noise independent of the object image. (This noise should be distinguished from the noise due to random nature of the incoming particle flux, which is object-dependent).

The coded-aperture technique was proposed simultaneously and independently in the mid-1980s by two groups<sup>249,276</sup> to enhance performance characteristics of ENA instrumentation. One group suggested installing coded-aperture masks at the instrument entrance to increase geometrical throughput.<sup>112,276–278</sup> Another group argued that although a coded aperture was not superior to a pinhole in terms of the signal-to-noise ratio for magnetosphere imaging, the coded-aperture camera would allow efficient use of the same sensor for imaging simultaneously in both low- and high-energy ENA fluxes.<sup>249</sup>

The coded-aperture technique is based on simultaneous use of a number of pinholes. The images formed by the pinholes mix (multiplex), overlap and superimpose (not matching each other) and produce picture at the instrument’s image plane non recognizable at first glance [Fig. 12(B)]. If a pinhole pattern is selected in a proper way, then it is possible to unscramble the resulting image by postprocessing, while minimizing errors and artifacts, and produce the image of the object.

Image multiplexing was pioneered in 1968<sup>279,280</sup> and used many times in space and laboratory experiments.<sup>274,275,281–288</sup> Uniformly redundant arrays<sup>283,289</sup> (URAs) of pinholes were found to provide the most efficient aperture coding with minimal imaging artifacts. URAs are based on pseudorandom sequences<sup>290,291</sup> widely used in the communications technology. A conceptually similar technique with multiplexing in time instead of space is successfully used in neutron scattering<sup>292</sup> and molecular beam<sup>293,294</sup> experiments.

A detailed comparison<sup>295</sup> between pinhole and coded-aperture cameras is summarized in Table I. Three factors are most important in the selection of the ENA imaging system. First, the magnetospheric and heliospheric images are expected to be widely distributed structures with slowly varying brightness rather than starlike objects. Second, the detector noise (with the exception of the statistical noise due to random nature of particle fluxes) is efficiently suppressed by coincidence requirements employed by ENA identification techniques. Third, EUV/UV background radiation may overload MCP detectors in the sensor.

The coded-aperture technique is advantageous when used for the detection of starlike objects and in the presence of the object-independent detector noise. Pinhole cameras seem to be superior for ENA imaging since they are simpler, more tolerant to background EUV/UV, and free of the problems with object partial coding, while the coded-aperture technique is prone to artifacts.<sup>295</sup> Additionally, even small manufacturing imperfections of coded-aperture masks may result in very complex imaging artifacts.<sup>296,297</sup> A pinhole-

TABLE I. Comparison of pinhole and coded-aperture imaging systems for ENA imaging of space plasmas.<sup>a</sup>

Characteristic	Pinhole camera	Coded-aperture camera
imaging of starlike objects	inferior	superior
imaging of objects with uniformly distributed brightness	slightly superior in the absence of noise; becomes inferior with the increasing of detector noise	slightly inferior in the absence of noise; becomes superior with the increasing of detector noise
detector noise	may be a problem	suppressed
partial coding of objects	objects are fully coded	image artifacts
high count rates of detectors due to the EUV/UV background	insignificant	significant
electronic adjustment of the resolution	impossible	possible
simultaneous use for high-energy ENA imaging	no	yes
manufacturing imperfections	negligible effect	can be significant; image artifacts
simple/complex	simple	complex

<sup>a</sup>After Ref. 295.

type camera is thus an imaging configuration of choice, at least for the experiments in the near future.

## V. ENA DIAGNOSTICS OF FUSION PLASMAS

ENA diagnostics is a well-established approach to study fusion plasma characteristics.<sup>33–36,298–300</sup> Such corpuscular diagnostics have been successfully used in various forms since the early 1960s<sup>33,301</sup> at many magnetically confined plasma machines, e.g., T-3,<sup>4</sup> DOUBLET III,<sup>302</sup> PLT,<sup>34,303</sup> TFTR,<sup>304</sup> 2XIIB,<sup>300</sup> JET,<sup>305,306</sup> ASDEX,<sup>307</sup> JT-60,<sup>308,309</sup> RFX,<sup>310</sup> MST,<sup>311</sup> and TORTUR.<sup>312,313</sup> The energy range of the measured neutrals extends from a few hundred eV<sup>303,314</sup> up to 0.1–1.0 MeV.<sup>304,306,309</sup>

Most of the fusion plasma ENA analyzers in the energy range 0.5–100 keV are based on ionizing the neutrals in special stripping cells and subsequent analysis of positive ions. A stripping cell is usually filled with gas<sup>301,302,308,311,314</sup> or plasma.<sup>315</sup> Pulsed gas and pulsed plasma targets have been also used to increase stripping efficiency while minimizing the load on vacuum pumps. One of the major advantages of gas targets is minimal disturbance of the neutral atom energy distribution (compare with energy losses and scattering in ultrathin foils: see Sec. VI D 2). Gas targets can also be used in space instruments that do not require continuous long-term operation, such as the solar EUV optics-free spectrometers.<sup>316–318</sup> For ENA imaging in space, the use of gas targets is unlikely.

The instruments for detection of fusion plasma-emitted ENAs with  $E < 500$  eV are usually based on mechanical choppers in various configurations<sup>303,307,310</sup> although electron impact ionization has also been used.<sup>319</sup> The chopper approach is conceptually not unlike the slotted-disk velocity selector developed for space neutrals.<sup>181</sup> Conventional me-

chanical choppers are unacceptably large and heavy for space instruments, however recent suggestion<sup>216</sup> to mechanically modulate the incoming ENA flux by miniature transmission gratings may open a way for this technique in space instruments.

Neutral atom surface conversion to negative ions was recently implemented for fusion plasma diagnostics.<sup>312,313</sup> A similar approach for detection of ultralow-energy ENAs in space<sup>10,177</sup> has tremendous promise when fully developed and will be discussed in some detail below (Section VI G 2). Similarities between ENA imaging of space and fusion plasmas led to the proposals of application of recent technological advances in space instruments to fusion plasma diagnostics.<sup>320</sup>

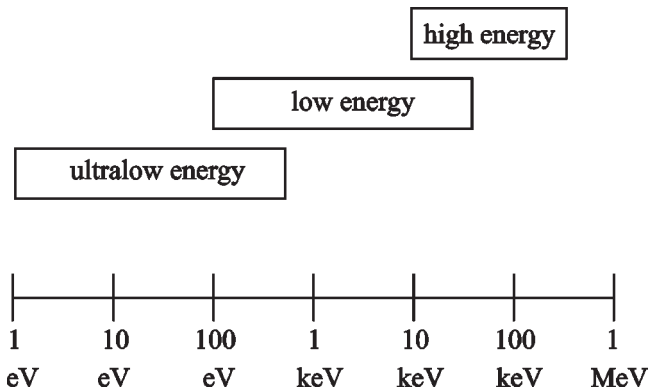


FIG. 13. Energy ranges of three major ENA instrument groups.



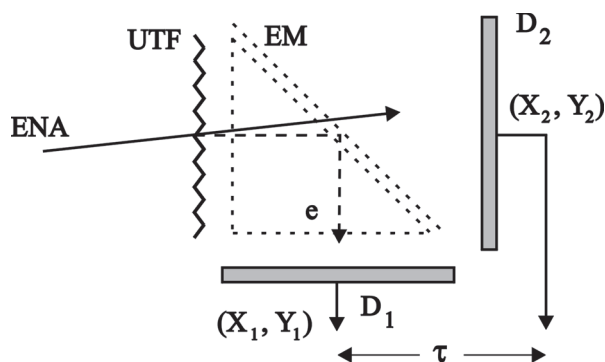


FIG. 14. Schematic of a generic sensor illustrating techniques used in many ENA instruments. (UTF) ultrathin foil; (EM) electrostatic mirror, ( $D_1$  and  $D_2$ ) detectors capable of determining coordinates ( $X, Y$ ) of particle impinging on the sensitive surface and accurately fixing the moment of particle registration.

## VI. BASICS OF ENA DETECTION AND IDENTIFICATION

### A. Principal scheme of ENA detection in space

Presently all ENA instruments can be roughly divided into three partially overlapping major groups (Fig. 13): instruments for high-energy ENAs ( $E > 10$  keV/nucleon), for low-energy ENAs ( $100 \text{ eV} < E < 50 \text{ keV}$ ), and for ultralow energy ENAs ( $E < 500 \text{ eV}$ ). Various aspects of ENA instrumentation were reviewed in the past.<sup>4,10,111,112,216,248,250,256,295,321</sup> In this section we will start with a brief description of common approaches in ENA instruments, and then consider in some detail major instrument components and techniques. Then in Sec. VII we will consider representative instrument designs illustrating the state of the art and new directions in ENA instrumentation.

An ENA instrument consists of a deflector-collimator followed by a sensor performing detection and identification of incoming neutral particles. The deflector prevents ambient charged particles from entering the sensor, but leaves the incoming EUV/UV background radiation unaffected. The upper energy limit of the instruments is determined by the deflector ability to separate ENAs from energetic ions by preventing the latter from entering the sensor (usually 100–300 keV/e). Cosmic ray particles (penetrating particles) are rejected by using sensor capabilities of measuring ENA energy and/or velocity.

Let us first demonstrate some concepts of ENA detection and identification on a simplified generic sensor found in various forms in many ENA instruments. This sensor consists of an ultrathin (20–200 Å) foil (UTF) at the entrance, electrostatic mirror (EM), and detectors  $D_1$  and  $D_2$  (Fig. 14). An ENA penetrates the foil and hits the detector  $D_2$ . The electrons emitted from the foil by ENA passage are accelerated and transported to the detector  $D_1$ . By measuring coordinates of the electron impinging on  $D_1$  ( $X_1, Y_1$ ) and particle on  $D_2$  ( $X_2, Y_2$ ), one can determine the particle's trajectory between the foil and the detector  $D_2$ .

The particle velocity is determined by measuring a time interval (time of flight) between electron detection by  $D_1$  and particle detection by  $D_2$ . If  $D_2$  is a solid-state detector, then the particle total energy can also be established. Simulta-

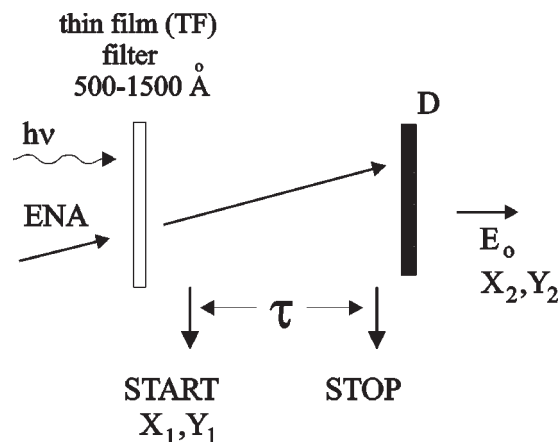


FIG. 15. Schematic of high-energy ENA detection.

neous measurement of particle velocity and energy allows unambiguous mass identification. The ability of thin-foil time-of-flight (TOF) spectrometers to distinguish among incoming monoenergetic particles with different masses improves with the increasing particle energy. For example masses 1, 2, and 4 can be separated at such low energies as 3 keV,<sup>322,323</sup> while separation of masses 12 and 16 would require energy  $\sim 25 \text{ keV}$ .<sup>37</sup>

TOF spectrometers are exceptionally efficient in rejecting detector noise counts. A valid ENA event (detection) requires signals from several detectors within well-defined narrow (100–200 ns) time gates (coincidence requirement). Background photons and stray particles would produce detector noise count rates proportional to the instrument geometrical factor and correspondingly proportional to the incoming ENA fluxes. The noise counts are random, and there is a certain probability that they produce a false “ENA event” by triggering the detectors within the coincidence time gates. The rate of double and triple random coincidences is proportional to the square and cube of the incoming flux, respectively. The ENA signal is directly proportional to the incoming ENA flux. This square or cube proportionality of the random coincidence rates allows extraction of a weak ENA signal from the superior detector noise count rate.<sup>217</sup> For example, a triple coincidence random noise due to background EUV/UV radiation is expected to be about seven events per year in the ENA instrument on Cassini.<sup>24</sup>

Particles with very high energies ( $> 1 \text{ MeV}$ ), typical for nuclear physics experiments, are detected with almost 100% efficiency by TOF spectrometers. The energies of ENAs and electrons emitted from thin foils are much smaller, and the detection efficiencies can be anywhere between a fraction of a percent and 100%. Electron yields from foils may also vary from a hundredth to a few electrons per incident ENA. A coincidence technique offers a unique opportunity to determine, in the absence of noise, instrument absolute detection efficiency without independent knowledge of the incoming calibration flux.<sup>217</sup> This feature of the coincidence technique was used for the first time in the 1920s by Geiger and Werner<sup>324</sup> who determined the efficiency ( $< 100\%$ ) of human observers in counting scintillations.

Schematics of high-energy, low-energy, and ultralow-

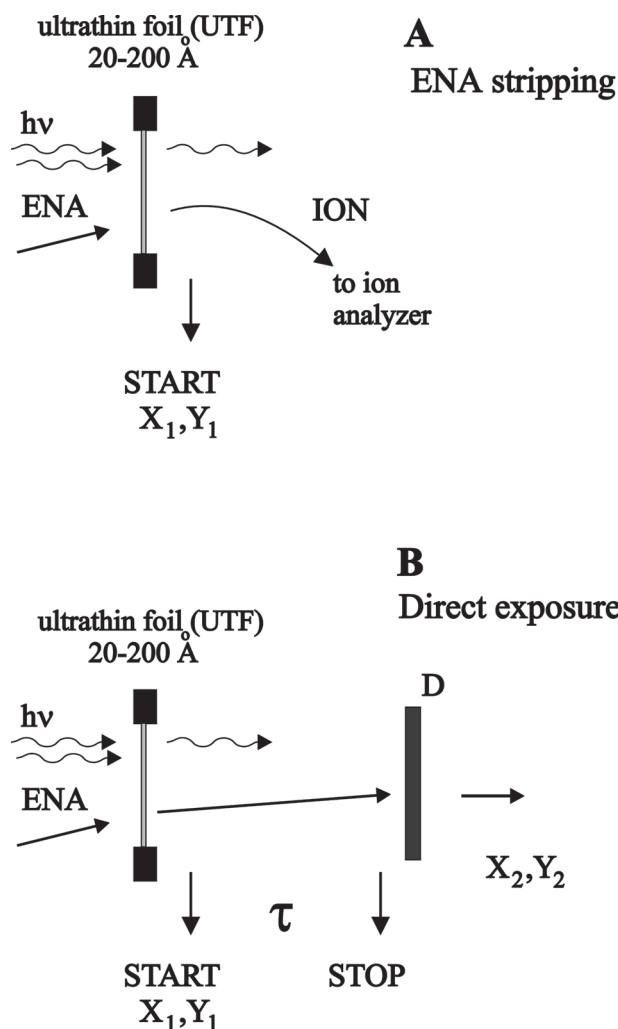


FIG. 16. Schematic of low-energy ENA detection by conversion of ENAs to ions (A) and by a direct-exposure time-of-flight technique (B).

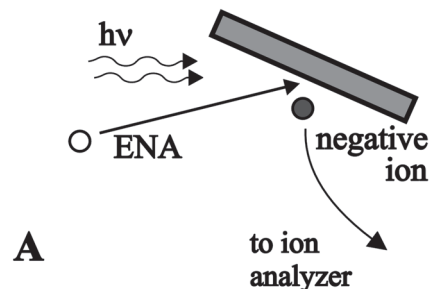
energy ENA sensors are shown in Figs. 15, 16, and 17, respectively.

### 1. High-energy ENA sensors

A high-energy ENA instrument can be protected against background radiation by a thin ( $\sim 0.1 \mu\text{m}$ ) film (TF) filter, which significantly reduces the EUV/UV photon flux into the instrument (Fig. 15). A protective thin-film filter at the instrument entrance would modify energy and angular distributions of incoming ENAs. Thin-film filters and solid-state detectors determine an effective energy threshold ( $> 10 \text{ keV/nucleon}$ ) for such instruments.<sup>250</sup> Electron emission from the film, or from an additional ultrathin foil, can be used to provide a START signal for a TOF analyzer and to determine the position ( $X_1, Y_1$ ) of the point of ENA entry. The detector D provides a STOP signal and particle position ( $X_2, Y_2$ ). A solid-state detector D would also measure the total energy of the particle. Thus one can determine the particle's trajectory, velocity, and energy (and mass).

Conceptually similar TOF spectrometers are often used for particle identification in nuclear physics.<sup>325</sup> ENA energies are insufficient for thin solid-state  $\Delta E$  detectors, as used in particle  $\Delta E-E$  telescopes,<sup>38,40</sup> therefore ultrathin foils are

### Conversion to negative ions



### Secondary ion emission

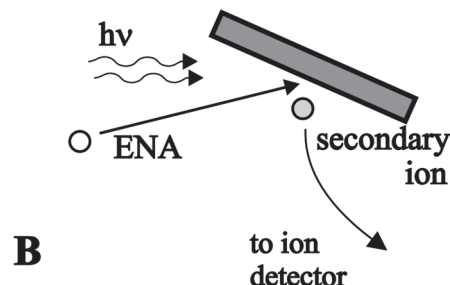


FIG. 17. Schematic of ultralow-energy ENA detection by ENA surface conversion to negative ions (A) and by secondary ion emission (B).

needed for START signal generation. The ultrathin foils were introduced in TOF spectrometers initially for study of particles with  $E > 100 \text{ keV}$ ;<sup>326–328</sup> this energy limit was lowered later down to  $\sim 10\text{--}20 \text{ keV}$ <sup>37</sup> and eventually down to  $600 \text{ eV}$ .<sup>217</sup>

### 2. Low-energy ENA sensors

Particle absorption, straggling, and scattering prohibit use of protective thin-film filters for detection of ENAs with  $E < 10 \text{ keV}$ . Two ways to register low-energy ENAs by filterless, open-type instruments have been developed (Fig. 16): (A) to convert ENAs to ions by stripping in an ultrathin foil with subsequent deflection (and separation from the background photons), analysis and detection of ions;<sup>4,212,321</sup> and (B) to expose the instrument directly to both the EUV/UV radiation and ENA flux and to detect ENAs by the TOF technique.<sup>182,217</sup>

Both techniques have advantages and disadvantages. The efficiency with which the ENA-stripping technique [Fig. 16(A)] “uses” incident ENAs is relatively low: only a fraction of ENAs is ionized during the passage of the foil, and an electrostatic energy analyzer usually measures ions in a scanning mode. The efficiency of stripping helium and oxygen ENAs is approximately a factor of 5–10 lower than the probability of stripping hydrogen of the same energy.<sup>256</sup> An important advantage of the stripping technique is convenient particle separation from photons, which efficiently suppresses the background EUV/UV radiation.<sup>4,212,321</sup>

An alternative direct-exposure approach [Fig. 16(B)] allows highly efficient simultaneous parallel detection and velocity analysis of ENAs across the wide energy range by the

TOF technique. An incoming photon may trigger either the start or stop detector, when an ENA may trigger both (coincidence). The coincidence requirement allows separation of weak ENA signals from superior background counts. The technique does not require ENA stripping and hence it does not discriminate against helium and oxygen. The major disadvantage is direct exposure of ultrathin foils and detectors to the background EUV/UV radiation. The restrictions on detector maximum count rates thus limit possible sensor geometrical throughput. New diffraction filters (Sec. VI F) transparent to ENAs and suppressing EUV/UV radiation open the way for efficient use of the direct-exposure instruments.

The efficiency of ENA stripping and electron yield from the foils decreases with the decreasing ENA energy which determines the lower energy limit of the described approaches (Fig. 16). The upper energy limit is determined by the desired energy resolution of TOF spectrometers. The energy range of low-energy ENA instruments can be between a hundred eV and 50–80 keV (Fig. 13).

### 3. Ultralow-energy ENA sensors

Ultralow-energy (<500 eV) ENA detection is an emerging technique. The ENA energy is insufficient for a particle to penetrate an ultrathin foil, to strip an ENA, or to produce electron emission with the required efficiency. Traditional electron impact ionization was used for measurements of cometary neutrals from a fast moving spacecraft,<sup>319,329,330</sup> but such a technique is inefficient and can be employed only for relatively high neutral number densities.<sup>330,331</sup>

Two distinct new approaches to ultralow ENA detection were proposed (Fig. 17). The first approach [Fig. 17(A)] is based on surface conversion of impinging ENAs to negative ions with subsequent ion energy and mass analysis.<sup>10</sup> Surface conversion technique have no energy threshold for some incoming neutrals and surfaces, while the realistic upper energy limit is several hundred eV (Fig. 13). An alternative technique is based on secondary ion emission from a specially prepared surface which allows efficient suppression of EUV/UV radiation [Fig. 17(B)]. The latter technique is not capable of ENA mass analysis, has energy threshold 30–50 eV, and was successfully demonstrated in the GAS experiment on Ulysses for detection of interstellar helium atom flux.<sup>175,176</sup>

### B. Charged particle deflectors and collimators

A charged particle deflector at the ENA instrument entrance prevents ambient ions and electrons from entering the sensor and defines the instrument's FOV.<sup>11,111,112,248,250</sup> The upper energy limit of the instrument is the maximum energy  $E_{\text{MAX}}$  of the deflected ions, which can be anywhere from 50 to 500 keV/e depending on the specific mission requirements. Both electrostatic<sup>24,212,216</sup> and magnetic<sup>21,125,182,212</sup> fields as well as their combination<sup>23,212</sup> can be used in the deflectors. Permanent magnets (e.g., SmCo), which are especially efficient in removing ambient electrons, have an ad-

vantage of zero power consumption. However a permanent magnet deflector usually requires a yoke and magnetic shield, which may be unacceptably heavy.

An alternative arrangement is to use an electrostatic deflector, which is sometimes simpler and has an option of being turned on and off when desired, thus allowing the use of the same sensor for ion investigation.<sup>11</sup> The simplest deflector arrangement is a pair of parallel plates with the length,  $L$ , separation,  $d$ , and voltage between them,  $V$ . Ignoring the fringe fields, a simple trajectory under constant force allows one to approximate the maximum energy of ions  $E_{\text{MAX}}$  of charge  $q$  with initial velocity parallel to the plate such a collimator can reject

$$E_{\text{MAX}} = (qV/4)(L/d)^2.$$

The requirements of miniaturization and low power consumption limit realistically available deflection voltages to 20–30 kV in space instruments.<sup>43,45</sup> For a given voltage source, maximizing the  $L/d$  ratio maximizes  $E_{\text{MAX}}$ , but would simultaneously reduce the FOV of the instrument in the direction perpendicular to the deflection plates. Such a dependence favors a one-dimensional imaging instrument with a slitlike field of view. The collimator of a one-dimensional instrument would thus have much smaller separation,  $d$ , between deflector plates and consequently would allow one to achieve the desired value of  $E_{\text{MAX}}$  with much smaller voltage,  $V$ . A stack of several plate pairs can increase the effective geometrical factor, and correspondingly the instrument's sensitivity.<sup>11,24,111,112,248</sup> Therefore a one-dimensional ENA imaging system is highly attractive; the imaging in the second dimension can be achieved by taking advantage of spacecraft spinning (see Sec. IV A).

The collimator can be a source of noise counts and other undesired effects.<sup>11,111</sup> Forward scattering of incident particles by the collimator plates would alter the angular and energy characteristics of the incoming ENA flux. A serration of the plate surface reduces this effect.<sup>250,252</sup>

When a secondary electron, whether produced by an impact of an ion or a photon, is released from a negatively biased collimator plate, it is accelerated toward the opposite plate. The electron impact may produce x-ray or EUV photon(s). The photons, in turn, with some probability would strike the negatively biased opposite plate with production of more photoelectrons, resulting in a photon-electron cascade. Such cascades would increase the flux of energetic photons into the sensor and may overload the deflection plate high-voltage power supply. The treatment of the plate surfaces with graphite reduces photoelectron yield for bright background 1216 Å radiation; the lowering of the deflection voltage would reduce the x-ray yield.

The deflector/collimator design presents a special challenge for the instruments pointed close to the sun, e.g., for neutral solar wind measurements (5°–7° off the sun). Solar radiation is scattered and diffracted at the collimator (baffle) edges, and careful design is required to minimize the probability of stray photons reaching the sensor. Photon scattering characteristics of the instrument internal surfaces are thus important, in particular reflectance of bright 1216 Å radiation from various materials.<sup>302,332</sup> Stray light was successfully

suppressed in many space optical instruments.<sup>333</sup> Experimental verification of collimator performance presents a non-trivial problem, when suppression of 7–10 orders of magnitude has to be demonstrated for a bright light source close to the instrument axis.

A strong emphasis on compact instruments for future space missions led to the development of new efficient collimators with a large geometrical throughput.<sup>334</sup> A wide circular FOV combined with a small distance between the deflecting plates can be achieved by maintaining a slitlike geometry of the collimator while bending it to form a full circle thus resulting in an annular collimator. Such a collimator provides an unusually high geometrical throughput for its size, and is suitable for study of ENA fluxes with low angular resolution, for example the heliospheric low-energy ENAs.<sup>9,334</sup>

### C. Detectors

Various detectors are used in ENA instruments for detection of incoming ENAs and secondary ions and electrons produced by ENA interaction with foils and surfaces. Solid-state semiconductor detectors can be used directly for detection of ENAs with energies higher than 10–20 keV. Solid-state detectors are capable of measuring the total energy of incoming particles, and when combined with TOF velocity measurement, the particle mass can be identified.

An energetic particle penetrates the solid-state detector and loses energy in Coulomb collisions with free and bound electrons.<sup>335,336</sup> The particle energy loss thus results in the creation of electron-hole pairs. For example, it takes on average 3.62 eV to create an electron-hole pair in silicon at room temperature. The charge carriers created by the energetic particle drift to the contacts of the opposite polarity. By measuring the total charge collected on a contact one can determine the total energy lost by a particle in the detector. Solid-state semiconductor detectors have been used widely for energetic particle detection in nuclear physics experiments<sup>336,337</sup> and in space.<sup>21,38,40,239</sup> Such detectors can be applied without any modification for ENA detection providing incoming charged particles are prevented from reaching the detectors.

Detectors are often required to provide signals for both precise timing and pulse amplitude (for total energy or position) measurements. While a solid-state detector provides a “slow” signal for amplitude measurement, the electrons knocked out from the detector’s surface can be used for precise timing by triggering an additional “fast” detector. Electron detection also allows independent determination of the position of particle impact, similar to determination of the point of foil penetration (Fig. 14). The solid-state detectors are sometimes cooled to improve energy resolution.<sup>125</sup> The energy loss in the detector surface layer that determines effective energy threshold is well known for H, He, and O particles.<sup>338,339</sup>

The technology allows fabrication of solid-state multianode detectors with radiation hardened complementary metal-oxide semiconductor (CMOS) electronic circuits to amplify and sort out signals from different anodes, for example a 256-pixel multianode sensor with independent readouts.<sup>125</sup>

The proton dead zone is 8 keV and energy resolution <2 keV at room temperature. Thus one can build simple ENA instruments consisting of multianode solid-state sensors with collimators defining separate FOV for each anode.

Low-energy ( $E < 10$  keV) ENAs cannot be directly detected by solid-state detectors. Low energy particles can be registered by detectors on the basis of secondary electron emission, the so called secondary electron multipliers. Secondary electron multipliers register any particle, including a photon, that can produce a secondary electron impinging on the sensitive surface.<sup>340</sup> EUV/UV photons are readily counted by secondary electron multipliers, and the detection efficiency of a typical nonsensitized detector is a few percent at the hydrogen Ly- $\alpha$  line;<sup>341</sup> it may exceed 10% for  $\lambda < 1000$  Å,<sup>342</sup> and it decreases again in the x-ray spectral range. Secondary electron multipliers would be swamped by counts due to background EUV/UV radiation if exposed unprotected in space.

CEMs and microchannel plates (MCPs) are most widely used in space instruments. These detectors were patented in the early 1940s and practically usable devices were fabricated 20 years later. A CEM is a tube made of a slightly conducting glass. A high voltage applied between the tube ends creates an axial electric field inside the tube that allows the propagation and multiplication of an incoming electron, thus producing an avalanche of many millions of electrons at the channel exit. A CEM became a workhorse of particle detection since the early 1960s.<sup>343–345</sup>

A remarkable feature of the channel multipliers is that electron multiplication is determined mostly by the channel length-to-diameter ratio rather than the absolute channel size. This dependence opened the way for miniaturization of channel multipliers, while preserving to a large extent their multiplication properties. An MCP is a two-dimensional array of several millions identical miniature channel electron multipliers, closely packed parallel to each other.<sup>346–351</sup> The first MCPs were composed of channels 200  $\mu\text{m}$  in diameter;<sup>352</sup> in modern plates channel diameters are 6–12  $\mu\text{m}$ . MCP sensitive areas vary from a few cm in diameter up to  $10 \times 10$  cm and larger.

The MCPs are usually used in stacks of two or more plates (with straight microchannels) in series to increase their gain without causing undesired ion feedback. Sometimes MCPs with curved channels are used but they are more expensive and more difficult to handle.<sup>353</sup> CEMs and MCP stacks generate electron avalanches consisting of  $10^6$ – $10^8$  electrons in response to an arrival or emission of a single electron at the entrance. The exit electron charge outbursts are easily amplified and registered by conventional electronic circuitry.

An individual CEM does not have any position determination capability except to establish that it received a particle. Formation of an electron avalanche in the channel and its propagation is a statistical process.<sup>346,354</sup> The time interval between a particle impact on the sensitive surface and appearance of the electron outburst at the channel’s exit slightly varies (time jitter). This results in another disadvantage of the CEM, viz., the inability to determine the moment of particle detection with accuracy better than a few nano-



seconds. MCP detectors allow one to reduce the time jitter to a fraction of a nanosecond,<sup>350</sup> which makes them detectors of choice in ENA instruments. MCPs can also provide position sensitivity (see below) across large sensitive areas.

The requirement of timing accuracy is exceptionally important for high-energy ENA identification since it directly determines velocity resolution of the compact TOF sensors. A time resolution better than 1 ns is usually desired for high-energy ENA instruments. For low-energy ENAs, the requirements on timing accuracy are more relaxed since ENA straggling in ultrathin foils results in variation of energy loss. The resulting energy spread translates into variations of ENA velocities, and correspondingly TOF. A typical timing accuracy requirement in low-energy ENA instruments is 1–2 ns.

The electron avalanches leaving MCPs vary in amplitude: the width of pulse height distributions is usually quantitatively characterized by the so-called amplitude resolution. Simple threshold discriminators allow one to obtain timing accuracy 1–3 ns. Timing accuracies 0.5 ns and better can be achieved by more sophisticated constant-fraction discriminators.<sup>350</sup> Precise timing also requires impedance-matched 50  $\Omega$  anodes to prevent signal distortion and ringing. Such anodes provide an impedance-matched transition from an electron collector plate (anode) to a cable to an amplifier. These anodes are usually of conic shape<sup>328,350,355</sup> with large size extension in the axial direction. A novel compact impedance-matched anode with significantly reduced axial size was recently suggested on the basis of the circle of Apollonius.<sup>356,357</sup>

The exact position of particle impinging on the MCP sensitive surface can be determined by using a specially designed electron collector (anode). The position-sensitive detectors (PSD) use various electron readout designs.<sup>351,358–362</sup> The most common readout schemes are based on charge division either between edges of the resistive anode<sup>363,364</sup> or between isolated conducting anodes, in particular of the wedge-and-strip type.<sup>365</sup> Coordinate determination by a charge-division technique is based on accurate measurement of charges collected at several anode outputs or anode elements. Charge pulse amplitude measurement (“slow”) does not usually allow simultaneous use of the anode signals for particle timing (“fast”). A signal from the exit side of the last (in the stack) MCP is commonly used for fast timing. This fast positive pulse is related to the electron avalanche escape from the MCP exit and is obtained independently from the collector (charge) signals.<sup>366–368</sup>

Recently developed delay line MCP position-sensitive detectors are based on the measurement of the time interval between appearance of signals at two ends of the anode line. The delay lines were first used for coordinate determination in gas proportional counters.<sup>369</sup> First delay-line designs for MCP signal readout were based on wires.<sup>370,371</sup> Introduction of planar anode technology was a breakthrough that allowed fabrication of highly robust and reliable MCP delay line detectors,<sup>372–376</sup> the qualities highly desirable for space applications. The delay line technique is conceptually similar to TOF measurements common in many ENA instruments. Consequently the delay line position-sensitive detectors are exceptionally attractive and advantageous for straightforward

integration with the TOF electronics of ENA instruments.

Only modest position resolution is usually required in ENA instruments since

- (1) scattering in ultrathin foils introduces uncertainty into ENA initial trajectory, and
- (2) accuracy of an electron image transfer from the foil to the detector does not typically exceed 1 mm (see Sec. VI E).

The desired spatial resolution is thus limited to 30–40 pixels in one dimension; both one- and two-dimensional position-sensitive detectors are used.

## D. Ultrathin foils

### 1. Foil fabrication and characterization

Freestanding ultrathin foils play an exceptionally important role in ENA instrumentation: they serve for stripping passing ENAs, for producing secondary electrons, and for incident radiation attenuation. The foils must be freestanding without a solid substrate support to allow passage of ENAs and simultaneously mechanically robust. A high-transparency (90%–95%) metal grid usually provides the required foil support with slight reduction of the foil’s effective area. The adjectives “unbacked” and “self-supported” are sometimes used to describe the freestanding foils.

Two different units are used for foil thickness,  $\mu\text{g}/\text{cm}^2$  and  $\text{\AA}$ . The foil lattice structure is poorly known, and the material density may significantly differ from that of the bulk material.<sup>377</sup> Foil characterization by mass per unit area (which directly translates into the number of atoms per unit area) is preferable for many applications since it allows determination of energy loss and scattering of passing particles. The area density 1  $\mu\text{g}/\text{cm}^2$  of widely used carbon foils corresponds to a thickness of 35–45  $\text{\AA}$ , or  $\sim 15$  atomic layers.

The development of thin foil technology was started in response to nuclear physics demands for thin targets, thin windows, and thin strippers in linear particle accelerators. By the end of the 1940s and beginning of the 1950s, unbacked metal foils were produced with the 20–30  $\mu\text{g}/\text{cm}^2$  thickness.<sup>378,379</sup> The Chromium Corporation of America succeeded in fabricating freestanding nickel foils with the thickness down to 500  $\text{\AA}$ .<sup>380</sup> Nonmetal (SiO) foils were also produced with the thicknesses down to 8  $\mu\text{g}/\text{cm}^2$  in 1952.<sup>381</sup> Dielectric, nonconducting foils usually require extra care in applications to avoid charging that may lead to foil cracking.

Low atomic number materials reduce scattering and energy losses of penetrating particles. Consequently, carbon emerged as the material of choice for ultrathin foils: the carbon foils are characterized by high mechanical strength and technological simplicity. Freestanding carbon foils with 4 and 1  $\mu\text{g}/\text{cm}^2$  thicknesses were fabricated in 1960<sup>382</sup> and in the late 1960s,<sup>383</sup> respectively. Ultrathin foils are hardly visible by the naked eye and become opaque only at thicknesses greater than 80  $\mu\text{g}/\text{cm}^2$ . Foils as thin as  $\sim 20 \text{\AA}$  (0.5  $\mu\text{g}/\text{cm}^2$ ) were reported.<sup>4,256,384</sup>

Foil fabrication usually starts with deposition of the required material on a glass flat (or a microscope slide) covered by a soluble substrate. For example, evaporation of car-

bon from an arc *in vacuo* may serve as a source of carbon. After removal of the soluble layer (e.g., by dissolution in distilled water) the floating foil is picked up by a high-transparency metal grid which would serve as a supporting structure. Basics of thin foil fabrication technology,<sup>383</sup> fabrication details of thicker ( $35 \mu\text{g}/\text{cm}^2$ ) foils,<sup>385</sup> destructive technique for determination of carbon foil surface densities,<sup>386</sup> and deposition techniques for thin film preparation<sup>387</sup> are described in the literature.

The transparency of supporting metal grids can be as high as 90%–95%, and ultrathin carbon foils can be made 3 cm in diameter and larger. Although large research groups traditionally prepare foils in-house, thin carbon foils are commercially available, e.g., from the *Arizona Carbon Foil Co.*, Tucson, Arizona. The carbon foils with the diamondlike lattice structure were recently fabricated using plasma sputtering of pure graphite in high-vacuum discharge.<sup>388</sup> These foils are claimed to be significantly stronger, exhibit longer lifetimes under ion bombardment, and are characterized by lower energy loss of penetrating particles. The latter feature may allow reduction of the energy threshold for particle detection, but the smaller energy loss would result in lower electron emission and reduced detection efficiency.

Mechanical robustness to withstand vibrations and shocks of the rocket launch is a major foil requirement. In addition to carbon foils, thin Formvar foils (56% carbon, 7% hydrogen, and 37% oxygen by weight) seem to have outstanding mechanical strength.<sup>384</sup> Another problem of concern is possible pinholes, since a few pinholes may significantly reduce the foil's ability to suppress incoming radiation. When the primary purpose of a thin foil is ENA stripping and/or production of electrons for timing, the instrument characteristics are practically immune to pinholes and even to cracks in the foil structure; these defects would only slightly reduce detection or conversion efficiencies.

A clever way to nondestructively test thin foils for pinhole presence is to illuminate the foil by a flux of low energy (200 eV) ions.<sup>389</sup> Incident ions that pass through the undamaged foil emerge mostly as neutrals at this energy. The neutrals are detected with a very low detection efficiency (<1%) by an MCP-based position-sensitive detector installed immediately behind the foil. However if a pinhole is present, then an incident ion would pass through the hole without changing its charge. The ion is accelerated between the foil and the detector and registered with high efficiency. Thus the bright spots in the registered image would show the pinholes in the foil.

Carbon is a very effective adsorbent, and carbon foils may contain large amount of impurities. Characterization of the foils which are only 10–20 atomic layers thick is a non-trivial problem. One desires to establish both the amount of carbon in the foil and impurities in the foil and on its surface. Bulk material impurities would affect ENA energy loss, scattering, and secondary electron production and transport inside the foil. Surface impurities would mostly affect electron escape probability and electron yield as well as charge state of exiting particles.

Ultrathin foils were analyzed by various techniques common in surface studies.<sup>390</sup> The enhanced proton scatter-

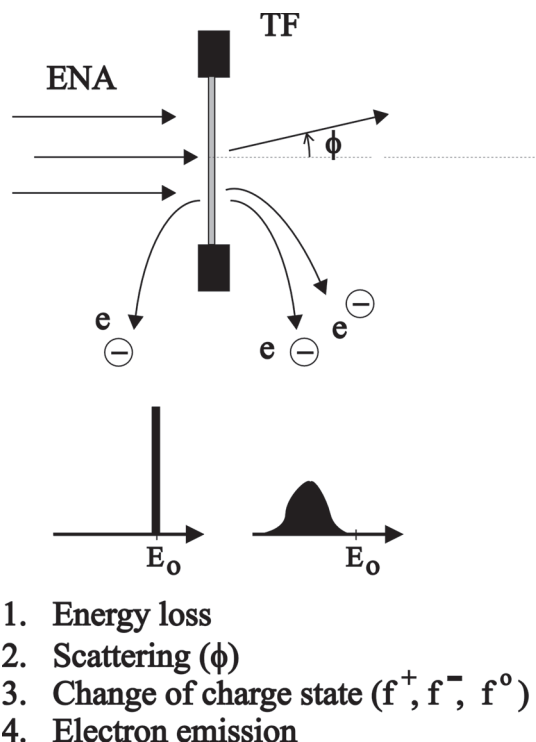


FIG. 18. ENA penetration through a thin foil (TF) results in particle energy loss, scattering, possible change of particle charge state (fractions  $f^+$ ,  $f^-$ ,  $f^0$ ), and electron emission (backward and forward).

ing technique is very sensitive to carbon and especially suitable for the analysis of ultrathin foils. Rutherford backscattering spectroscopy (RBS) is useful in determination of carbon and bulk heavy impurities in thicker ( $>500 \text{ \AA}$ ) foils. Various fast ion techniques can be used for characterization of even thicker ( $>1000 \text{ \AA}$ ) foils.<sup>391</sup>

Secondary ion mass spectroscopy (SIMS) is especially efficient for study of the surface layer composition. However, the probing beam currents are unacceptably high in conventional SIMS instruments and would destroy a fragile ultrathin foil. An unconventional TOF SIMS technique was developed to nondestructively study ultrathin foils.<sup>392</sup> The presence of H, O, F, Na, K, and other species was revealed at the surface of a  $30 \text{ \AA}$  carbon foil.

Foil properties may be significantly modified during applications. For example, the observed foil thickening under particle bombardment may be attributed to deposition of carbon from cracking the residual hydrocarbons.<sup>393</sup> Foil crystallographic transformations may also occur because of local temperature increase due to energy deposition by passing energetic particles.<sup>394</sup> Such structural transformations may result in ultimate foil breakage and effectively reduce the foil lifetime. ENA fluxes in space are usually very weak, and the effect of foil crystallographic transformation is probably insignificant in ENA instruments.

The degree of uniformity of the foil thickness is largely unknown. An average number of atomic layers may not exceed a dozen in an ultrathin foil. If the foil material deposition during fabrication is a random process, then large variations in the foil thickness can be expected.<sup>395</sup> For example, for a foil with a thickness of 16 atomic layers, one could expect a  $\pm 25\%$  thickness variation for such a model. An

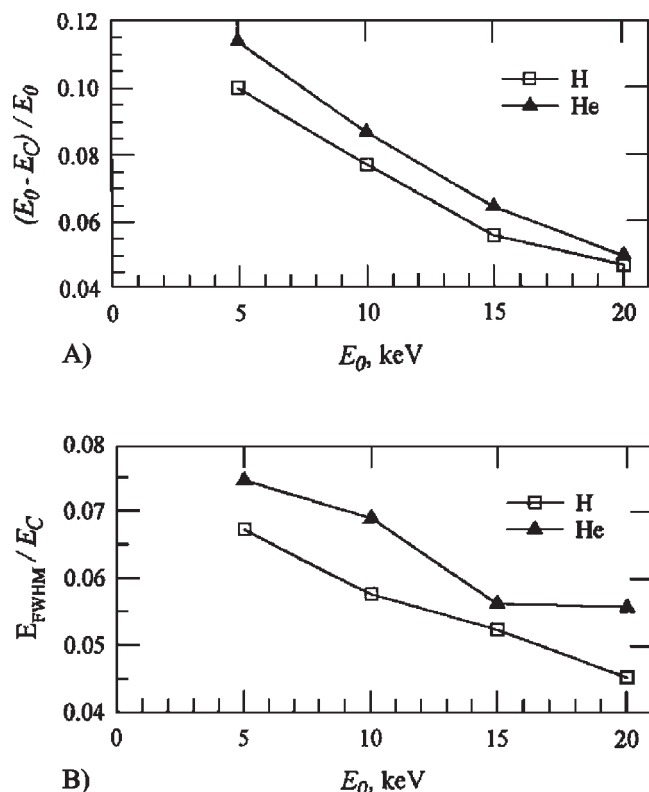


FIG. 19. Energy-loss statistics of H<sup>+</sup> and He<sup>+</sup> transiting a 1.1 μg/cm<sup>2</sup> carbon foil: (a) energy loss ( $E_0 - E_C$ , where  $E_C$  is the most probable energy of transmitted particles) relative to incident energy  $E_0$  and (b) energy spread (FWHM) relative to  $E_C$ . (After Ref. 216.)

experimentally established foil thickness is an average across the surface, and there are no reliable experimental data on thickness distribution. The thickness uncertainty limits our ability to optimize ENA instrument characteristics by accurate selection of ultrathin (<100 Å) foils.

Special caution should be exercised for use of ultrathin carbon foils in the instruments in low earth orbit. Highly reactive atomic oxygen is the most abundant constituent of the atmosphere between 200 and 500 km altitudes. The collision energy of impinging oxygen atoms with respect to a spacecraft is ~5 eV (for orbital velocity 7–8 km/s), and materials exposed to oxygen atom flux are subject to potentially severe chemical etching. Study of bulk graphite etching in low earth orbit show that one C atom is etched for every eight incident O atoms.<sup>396</sup> Such an etching yield would result in etching out one layer of carbon atoms in 2–3 min in a 400 km altitude orbit. Thus an ultrathin carbon foil directly exposed to the ram oxygen atom flux would not survive more than a few hours in low earth orbit.

## 2. ENA interaction with foils

ENA penetration of a thin foil results in particle energy loss, scattering, possible change of its initial charge state, and emission of electrons from the foil surface (Fig. 18). These processes depend on the ENA energy and mass and the composition and thickness of the target and are generally well understood.<sup>397–405</sup>

**Energy loss and scattering:** ENA scattering and energy loss occur due to collisions and interactions with solid body

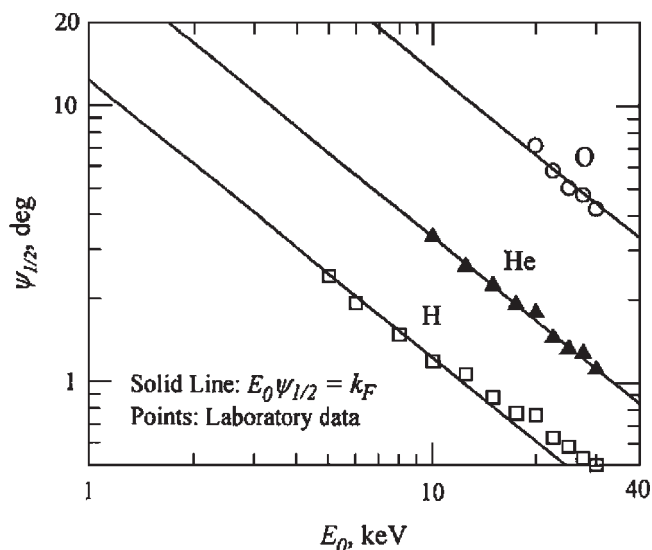


FIG. 20. Scattering of H, He, and O ENAs in a 1.1 μg/cm<sup>2</sup> carbon foil;  $\psi_{1/2}$  is the angular scattering half-width. (After Ref. 216.)

electrons and lattice ions. These interactions are a statistical process, and an incident monoenergetic and collimated particle beam would be characterized by a certain energy and angular distributions after leaving the foil (Fig. 18). Both the relative mean energy loss (i.e., energy loss divided by the incident particle energy) and relative energy spread increase with the decreasing incident particle energy (Fig. 19).<sup>216</sup> The relative energy spread becomes comparable to the mean energy of transmitted particles at energies <1000 eV. For example, for 1000 eV hydrogen atoms incident on 2.7 μg/cm<sup>2</sup> carbon foil, the mean energy after the foil is  $E = 670$  eV, the energy spread, full width half-maximum (FWHM) is  $\Delta E = 140$  eV, and  $\Delta E/E \approx 0.21$ .<sup>406</sup> For incident hydrogen atoms with the energy 600 eV,  $\Delta E/E \approx 0.5$ .<sup>217</sup>

Monte Carlo computer simulations were shown to accurately describe particle energy loss and scattering for a given target composition.<sup>407</sup> The widely used computer code, The Transport of Ions in Matter (TRIM)<sup>405,408</sup> allows one to perform extensive simulations of particle penetration through various thin films and ultrathin foils.<sup>216</sup> A major problem in such simulations is the uncertainty of the real foil parameters, in particular ultrathin foil thickness.

Figure 20 demonstrates the energy dependence of the average scattering angle in an ultrathin (1.1 μg/cm<sup>2</sup>) carbon foil for H, He, and O ENAs.<sup>216</sup> The particle scattering limits the accuracy of ENA trajectory reconstruction by measuring coordinates of two trajectory points in the sensor (Fig. 14). Scattering significantly increases with the decreasing energy and with the increasing particle mass for a given energy. The reconstruction of the incoming particle trajectory with an accuracy of 3° can be done for H atoms with the energy  $E > 4$  keV, for He atoms with  $E > 14$  keV, and for O atoms for  $E > 40$  keV. Scattering in the foil is determined mostly by multiple small angle scatterings; only rarely is the particle deflected by a large angle in a close collision. Correspondingly the angular distribution of particles after the foil can be roughly described by a Gaussian function with a small large-angle tail due to rare collisions.<sup>400</sup>



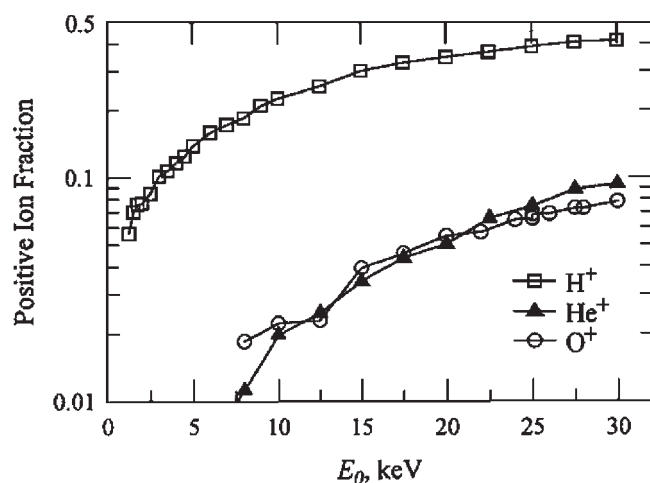


FIG. 21. The probability that H, He, and O exit a  $1.1 \mu\text{g}/\text{cm}^2$  carbon foil as positive ions. The solid lines are to guide the eye. (After Ref. 216.)

**Charge state:** Many low-energy ENA instruments [Fig. 16(A)] are based on ENA conversion to ions in foil passage. An incident ENA can be either stripped to a positive ion, or emerge as a negative ion, or stay neutral. The efficiency of ENA detection by the foil-stripping technique is directly proportional to the ENA stripping efficiency. The charge of the emerging particle is determined by the average charge of the ion moving inside the foil and the processes at particle exit from the foil.

An incident particle loses its initial charge after passing through the first 2–3 atomic layers in the foil, and the exit charge state thus does not depend on the initial charge. Therefore the experimental data on ion interaction with ultrathin foils can be directly applied to ENAs. When a particle leaves the foil as a positive ion, the probability of electron capture from the exit surface strongly depends on particle velocity. A higher exiting velocity translates into less time spent near the surface and correspondingly lower probability of neutralization.

The charge fraction measurements for H, He, and O ENA species were performed mostly for energies higher than several keV.<sup>216,255,409–412</sup> Charge fractions of many other energetic particles were measured in support of the development of thin-foil heavy-ion TOF analyzers.<sup>410,413–416</sup> The energy dependence of the positive fraction is shown for H, He, and O ENAs in Fig. 21.<sup>216</sup>

The stripping technique is especially efficient for  $E > 10$  keV/nucleon, but can be used for ENAs with energies as low as 100 eV. Experimental data on charge fractions for  $E < 1000$  eV are scarce. The first measurements in the 200–3000 eV range established the following energy dependence for hydrogen after the carbon foil:  $f^+(\%) = 3.0 E_{\text{keV}}$  and  $f^-(\%) = 2.3 E_{\text{keV}}$  for positive and negative fractions, respectively, where  $E_{\text{keV}}$  is in keV.<sup>406</sup> The hydrogen charge fractions were recently measured<sup>411,412</sup> for energies down to 500 eV; these measurements confirmed the earlier<sup>406</sup> results. The foil stripping technique would provide ENA detection efficiency up to 1% for energy  $\sim 300$  eV.

For hydrogen ENAs, the positively charged ion fraction is always higher than the negatively charged fraction

after the foil.<sup>255,406,409,411</sup> For oxygen ENAs, the negative fraction is higher than the positive one for energies  $< 50$  keV,<sup>255,413,416</sup> for example by a factor of 5 for 10–20 keV. Hence negatively charged ions can be efficiently used for detection of oxygen ENAs in ultrathin foil instruments [Fig. 16(A)]. The negative ion fraction can be further increased by modifying the foil exit surface by electronegative materials such as cesium.

**Secondary electron emission:** Secondary electron emission under bombardment of atomic particles involves several physical processes.<sup>417–421</sup> At first energetic electrons are collisionally produced inside the solid body by a fast moving particle. The electrons are transported to the surface, where finally they must overcome the surface potential barrier to leave the body. The number of the produced energetic electrons is roughly proportional to the particle energy loss per unit length (eV/Å), and the secondary electron yield correspondingly increases with the increasing particle energy. The depth of electron escape from solid body varies from 10 to 15 Å for metals up to  $\sim 100$  Å for dielectrics. Electron emission from a thin foil determines detection efficiency of the direct-exposure ENA instruments [Fig. 16(B)] which could be about 15% for 3 keV hydrogen ENAs, and decreases rapidly to 0.5% with the energy decreasing to 600 eV.<sup>217</sup>

Electron emission occurs from both sides of the foil, forward and backward.<sup>253,422–427</sup> There is an asymmetry in electron yield, which depends on ENA energy. If a significant part of the particle energy is lost during the foil penetration, then more energetic electrons are produced near the foil surface exposed to the incoming beam and the backward electron yield is higher. If only a small fraction of ENA energy is lost, then usually the forward emission is higher because of the apparent preferential direction of the electron motion after their birth in the foil.

An unconventional secondary electron multiplier was proposed on the basis of forward electron emission using several ultrathin foils in series with voltages between the foils to accelerate the electrons.<sup>424</sup> Not only emitted electrons could be multiplied in the foils but also an incoming energetic particle would deposit all its energy in several consecutive foils thus producing the maximum possible electron emission.

A conventional thin-foil TOF spectrometer allows one to determine only velocities of low-energy ENAs without mass identification. Electron emission provides a means to distinguish among ENAs with the same velocity but different masses (and energies).<sup>24,249,253</sup> More energy would be lost by ENAs with higher mass (energy) and correspondingly the electron yield would be higher. Thus the differences in numbers of emitted electrons can be used for mass identification.

Such mass identification relies on statistical properties of electron emission, i.e., the distribution of probabilities of emission of one, two, etc. electrons. Statistics of the electron emission under heavy particle bombardment was extensively studied for solid bodies.<sup>427–435</sup> The measurements of the emission statistics from the foils are limited.<sup>253,425,426,431</sup> Deviations from a Poissonian distribution are a common feature of the electron emission from both solid bodies and foils, in particular the higher probability of emitting zero electrons



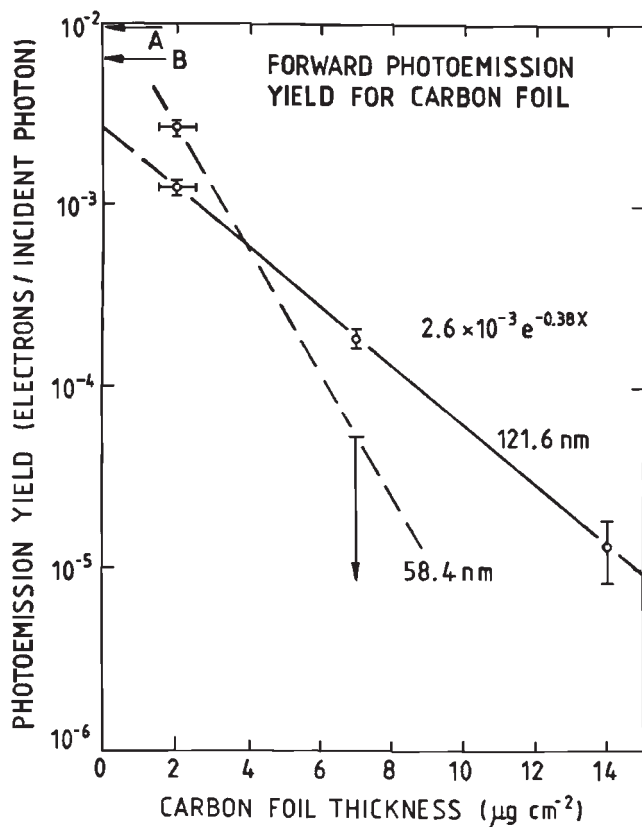


FIG. 22. Forward photoemission yield of carbon foil at 584 and 1216 Å. The low yield at 584 Å limits further information beyond  $7.0 \mu\text{g}/\text{cm}^2$ ;  $x$  is the foil thickness ( $\mu\text{g}/\text{cm}^2$ ) in the approximation formulas. (After Ref. 437.)

(i.e., no emission) is experimentally observed.

The detailed study of the electron emission statistics from ultrathin carbon foils showed that it would be possible to distinguish between hydrogen and oxygen ENAs, but separation of helium is more difficult.<sup>253</sup> The measurement of pulse heights from MCP detecting electrons is successfully used for ENA mass identification in the INCA instrument on Cassini.<sup>24</sup>

The foils could be sputtered by bombarding particles in ENA instruments. Sputtering yield depends on incoming particle mass and energy<sup>436</sup> and is usually much less than unity for light atoms. ENA fluxes in space are weak, and for all practical purposes one can disregard such foil degradation.

### 3. EUV interaction with foils

Thin-film filters (500–1500 Å) efficiently block background EUV/UV photon flux in high-energy ENA instruments (Fig. 15), while in low-energy ENA instruments, the photon flux is only partially attenuated by ultrathin foils (Fig. 16). The foils are directly exposed to the incoming radiation, and the photoelectrons that are indistinguishable from the electrons emitted by ENA passage may swamp the electron detectors.

External photoemission from solids is well understood and widely used in photon detectors (photomultipliers). The photoelectron yield from the exposed side of an ultrathin foil would be somewhat smaller than from the bulk material since some photons pass through the foil without absorption.

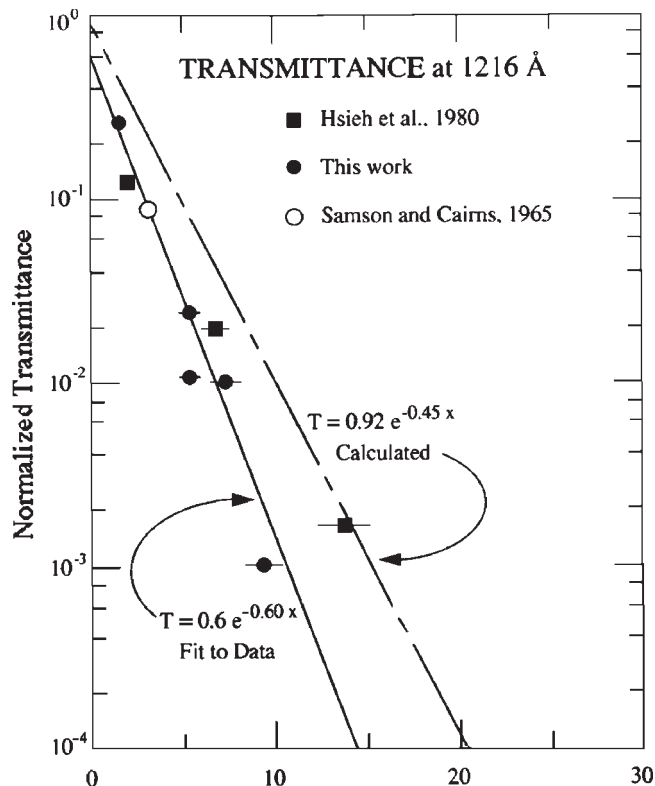


FIG. 23. Transmittance of the carbon foil at 1216 Å as function of foil thickness;  $x$  is the foil thickness ( $\mu\text{g}/\text{cm}^2$ ) in the approximation formulas. (After Ref. 438.)

Similarly to the ENA-induced electron emission, the forward photoelectron emission is most important in ENA instruments.

Forward photoelectron yield (a number of photoelectrons per incident photon) was experimentally established for the  $2\text{--}14 \mu\text{g}/\text{cm}^2$  foil thickness range at 584 and 1216 Å.<sup>437,438</sup> The yields (Fig. 22) can be best described<sup>438</sup> as  $2.6 \times 10^{-3} \times \exp(-0.38x)$  for 1216 Å and  $1.3 \times 10^{-2} \times \exp(-0.77x)$  for 584 Å, where  $x$  is the foil thickness in  $\mu\text{g}/\text{cm}^2$ . For example, approximately  $10^5$  photoelectrons/s would be forward emitted from a foil of  $2.5 \mu\text{g}/\text{cm}^2$  thickness,  $1 \text{ cm}^2$  area, and 1 sr field of view, pointed from 1 AU at the “darkest” possible direction (500R in H I Ly- $\alpha$ ).

Carbon foil transmittance<sup>437,439</sup> at 1216 Å is shown in Fig. 23.<sup>438</sup> The transmittance thickness dependence can be best described<sup>438</sup> as  $0.26 \times \exp(-0.37x)$ , where  $x$  is the foil thickness in  $\mu\text{g}/\text{cm}^2$ . The foil transmittance at 584 Å can be described<sup>438</sup> as  $0.10 \times \exp(-0.56x)$ .

### E. Electrostatic mirrors

Electron transfer from the foil to the detector (Fig. 14) has to preserve information on the position of electron emission and allow precise fixing of the moment of emission. The latter requirement means that the electron TOF between the foil and the detector should be independent of the point of emission, and such systems are called isochronous. If electrons are accelerated to the same energy, then their flight distances should be equal in an isochronous device. The simplest arrangement is to position an electron detector parallel to the foil surface, however such a configuration will not let

the normal-incident incoming particle to go through. Therefore the electron detector parallel to the foil can be used if the incoming particles impinge on the foil at a large angle, say  $45^\circ$ .<sup>37,328,440</sup>

Non-normal ENA incidence is inconvenient, the foil is effectively thicker, and geometrical transparency of the supporting grid is smaller. It is preferable to mount the foil normally to the incident particles and to position the electron detector off the sensor axis without exposing it directly to the accompanying EUV/UV photons. Excellent timing and imaging properties were achieved by magnetic isochronous electron transport systems.<sup>441–443</sup> Bulky and heavy field shielding and high power consumption preclude their use in compact space instruments.

An alternative isochronous electron transport device on the basis of an electrostatic mirror (Fig. 14) was introduced in nuclear physics spectrometers in 1980.<sup>368</sup> The first grid near the foil accelerates electrons to several keV. After traveling in the field-free zone, the electrons turn  $90^\circ$  in the reflection field, and after crossing the field-free zone again would reach the detector  $D_1$ . The electron flight distances are independent of the place of emission.

The electrostatic mirror also transfers an ENA-formed image from the foil to the detector  $D_1$  (Fig. 14). The energy distribution of the emitted electrons usually peaks at 1–2 eV and has a long “tail” of higher energy electrons. A realistic electron accelerating voltage is limited to several kV. A simple analysis shows that uncertainty in transport of position information is mostly due to the initial lateral electron velocity, which would limit electrostatic mirror performance to an approximate  $30 \times 30$  pixel image. Such an image would correspond to about 1 mm position resolution for a 30-mm-diam detector. An electron has to traverse grids several times on its way from the foil to the detector; one-dimensional (harp) high-transparency ( $\geq 0.95$ ) grids are often used to minimize electron losses.

## F. Diffraction filters

Separation of ENA particles from intense EUV/UV background radiation is one of the most important requirements to ENA instruments. Diffraction filters were suggested in the early 1980s to simultaneously provide efficient suppression of the incident EUV/UV radiation and high transmission for incoming particles.<sup>177,225</sup> Diffraction filtering is based on the photons ability to pass through a straight channel-pore (slit) in a filter only if the channel diameter (slit width) is much larger than the photon wavelength. In contrast to photons, an ENA passes through the channel freely if it does not collide with the channel walls. Thus diffraction filters permit separation of incident ENAs from EUV/UV photons and would serve as particle collimators. The requirements to filters include efficient suppression of EUV/UV radiation, high geometrical transparency to ENAs, and mechanical robustness.

Diffraction filtering is used in the far infrared wavelength regions. For example, the reflection of radiation by porous structures with pore diameters in the micron range is utilized in “superinsulator” shields for thermal protection in high-vacuum low-temperature environment. Radiation sup-

pression in the EUV/UV spectral range requires filters with an opening size of 1000 Å or less. Initial development of submicron structures for ENA imaging and EUV astronomical applications was based on nuclear track filters (NTF),<sup>177,225,444,445</sup> and it led to successful demonstration of EUV filtering.<sup>444</sup>

NTFs are fabricated by etching nuclear tracks produced by penetration of thin (1–20  $\mu\text{m}$ ) films (mica, lavsan, makrofol, etc.) by high-energy ( $\geq 1$  MeV/nucleon) heavy ( $>100$  amu) ions.<sup>446–448</sup> Almost perfectly cylindrical pores with diameters varying from 40 Å to 10  $\mu\text{m}$  can be reliably produced in films. Combining technological steps with different etching properties, channels with complex profiles could be obtained, e.g., funneled channels or channels with the cones at the entrance and exit connected by a straight part. NTF applications vary from diffusion enrichment of uranium to separation of cancer cells in the blood to clarification and cool stabilization of wine and beer by sieving out bacteria, sediment, and yeast.<sup>446–448</sup>

It was eventually concluded that NTFs are of limited practical use for ENA imaging because of their inherently low geometrical transparency.<sup>225,229,230,449</sup> (Substrate supported NTFs are successfully used in space solar and astrophysical observations.<sup>450,451</sup>) The filter holes are distributed randomly across the film with a rapid increase in hole overlapping with the increasing filter geometrical transparency.<sup>448,449</sup> Hole overlapping affects both filter EUV/UV transmission and mechanical robustness. Although NTFs with geometrical transparency up to 10% have been fabricated, filters with high geometrical transparency become highly fragile yet must withstand severe vibrations and shocks of the rocket launch. NTFs generally remain mechanically strong for geometrical transparencies below 1%.

Alternative technologies that can be used for diffraction filter fabrication include microchannel plates, anodically oxidized aluminum membranes, freestanding transmission gratings, and ion and laser hole “drilling” in filter films.<sup>225</sup> MCPs present a highly ordered structure with geometrical transparency up to 90%,<sup>349</sup> but the desired filter FOV would require MCP thickness and channel diameters far beyond the present-day technology. Laser and ion beam drilling of channels has its own inherent limitations.<sup>225</sup>

Porous structures can be found in anodic oxide films on aluminum.<sup>452,453</sup> When aluminum is anodized in a suitable electrolyte, a porous oxide layer develops on the surface. The film consists of the close-packed hexagonal array of cells, each containing a cylindrical pore. The pore size and the pore density depends on anodizing voltage (typically 10–200 V), whereas thickness of the porous layer is controlled coulombically. The pores are essentially parallel and pore sizes are in the 100–2500 Å range. The film thickness can be over 100  $\mu\text{m}$ , and geometrical transparency up to 0.25 can be obtained.

Recently developed technology allows detachment of the porous films by a programmed anodizing voltage reduction sequence.<sup>453–456</sup> It is possible not only to separate a porous film from the bulk of aluminum but the interface region of this film containing irregularly shaped pores can be etched out.<sup>453,454,456</sup> A highly ordered metal (platinum and gold)

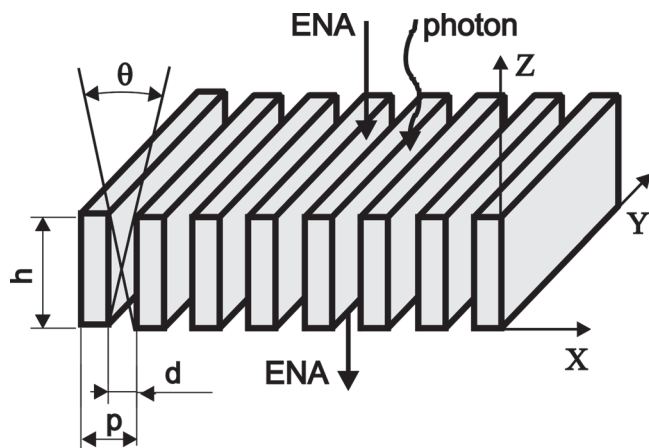


FIG. 24. Schematic representation of a freestanding transmission grating. The supporting large-mesh grid is not shown.

nanohole array was recently fabricated by a two-step replication of an anodic aluminum porous membrane.<sup>457</sup> This metal array presents a closely packed honeycombed structure  $\sim 700$  Å in diameter and 1–3  $\mu\text{m}$  thick.

Honeycomb structures on the basis of anodic membranes are not suitable yet for use as EUV/UV filters. However further development of this technology may lead to efficient diffraction filters for ENA instruments. Analysis of the currently available technologies points to the highly promising characteristics of freestanding transmission gratings that should both attenuate and polarize radiation.<sup>225</sup>

A schematic view of a freestanding transmission grating is shown in Fig. 24. The grating consists of a set of parallel gold bars with the period,  $p$ , and the geometrical transparency,  $g = d/p$ , approximately one half. The grating bars are supported by an extra large-mesh grid (not shown in the figure) and an overall grating geometrical transparency can be as high as 0.25. Standard available freestanding gratings have a period of 2000 Å and useful area of  $5 \times 11$  mm. Gratings can be mosaiced to increase the sensitive area. Transmission gratings are manufactured at the Massachusetts Institute of Technology by a sequence of steps including holographic lithography, ion and reactive-ion etching, and electroplating.<sup>226,227,458–462</sup> The gratings are being produced for NASA's Advanced X-Ray Astrophysics Facility (AXAF) where 336 transmission gratings will be flown as a part of the high energy transmission grating (HETG) spectrometer.<sup>463,464</sup> The present-day technology allows fabrication of gratings with a 1000 Å period.<sup>461</sup>

Although the AXAF requirements are confined to thin-film-supported gratings, a spin-off of the new technology is freestanding transmission gratings (Fig. 24). The freestanding gratings allowed laboratory demonstration of the de Broglie diffraction of neutral atoms,<sup>465,466</sup> and they have been successfully launched for the first time on the Solar and Heliospheric Observatory (SOHO) mission as a diffracting element in the solar EUV spectrophotometer.<sup>467</sup> Transmission gratings can be used in a standing-alone or crossed-tandem configurations for EUV/UV filtering,<sup>225</sup> and they would allow one to achieve efficient radiation suppression and high (5%–25%) geometrical transparency for ENAs.<sup>228–231</sup>

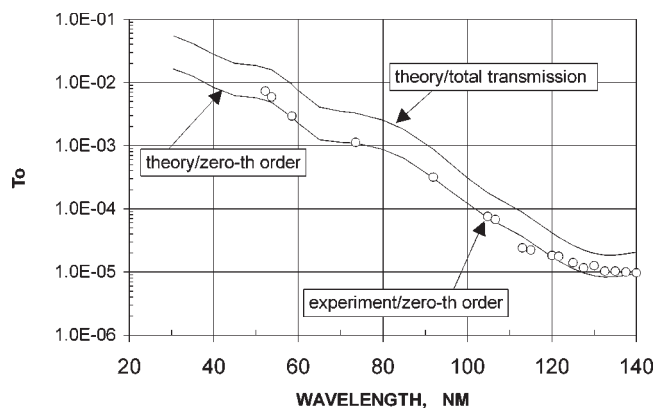


FIG. 25. Spectral dependence of the grating transmission  $T_0$  of unpolarized light. Experimental points (circles) show excellent agreement with computer simulations (thin line) of the transmission in the zeroth diffraction order. Theoretically calculated total transmission (transmitted radiation in all diffraction orders) is shown as a thick line. Grating structure period is 2000 Å, geometrical transparency  $g = d/p = 0.31$ ; grating thickness 4940 Å.

EUV transmission measurements of gratings are complicated by strong dependence on the incident light polarization. One can introduce the grating transmission  $T_P(\lambda)$  for transmission of the light polarized parallel to the grating metal bars, and the grating transmission  $T_S(\lambda)$  for transmission of the light polarized perpendicular to the grating metal bars.<sup>229,230</sup> The  $(T_P/T_S)$  ratio may be as high as  $>100$  at some wavelengths. The monochromatic light produced by any realistic testing facility is partially polarized. Though synchrotron light sources provide highly polarized radiation, the radiation at the monochromator exit would be partially polarized because of finite angles of acceptance into the monochromator system.<sup>468</sup>

Grating filtering properties can be obtained, using partially polarized radiation, by independent measurement of grating transmission at two grating orientations that are mutually perpendicular and normal to the incident photon beam.<sup>229,230</sup> From such measurements one can determine the sum of grating transmissions  $T_{\text{SUM}}(\lambda) = T_P(\lambda) + T_S(\lambda)$ . The transmission  $T_0$  of the incident “unpolarized” light by a single grating is  $T_0(\lambda) = T_{\text{SUM}}(\lambda)/2$ .

An example of the measured grating transmission  $T_0$  in the zeroth diffraction order is shown in Fig. 25 for the 520–1400 Å wavelength range.<sup>231</sup> The grating parameters were: period  $p = 2000$  Å, gap  $d = 620$  Å, geometrical transparency  $g = d/p = 0.31$ , and thickness  $h = 4940$  Å. The overall (with supporting structure) grating geometric transparency, i.e., transmission to ENA fluxes, was  $\approx 14\%$ .

Total grating transmission (i.e., radiation intensity in all transmitted diffraction orders) decreases almost three orders of magnitude with the wavelength increasing from 520 to 1300 Å, from  $T_0 \approx 1.7 \times 10^{-2}$  down to  $2 \times 10^{-5}$  (Fig. 25). One can see that the usually bright 1216 Å line would be attenuated by a factor of  $5 \times 10^4$  by a single grating. Even more efficient EUV/UV radiation suppression can be achieved by two crossed-tandem gratings,<sup>225,229,230</sup> i.e., by two sequentially installed and perpendicularly oriented gratings. The theoretical model and a computer code simulating grating filtering properties<sup>458</sup> were experimentally verified in the EUV wavelength range.<sup>231</sup>

A transmission grating would serve as a collimator for incoming particles. In our example, the grating collimator would have an angle  $\theta = 2 \arctan(d/h) = 14.3^\circ$  in the plane  $XZ$  and “unlimited” field of view (say  $\pm 40^\circ$ ) in the plane  $YZ$  (Fig. 24). Transmission gratings can be used in a straightforward way in one-dimensional ENA imaging instruments with  $5^\circ$ – $10^\circ$  FOV (1 pixel) in one direction and 8–20 pixels  $4^\circ$ – $10^\circ$  each in another perpendicular direction.

The efficiency of grating performance can be illustrated by an example of a direct exposure instrument [Fig. 16(B)] in the presence of nightglow and dayglow in the terrestrial environment. Let us consider an instrument without a transmission grating filter with a  $10^\circ \times 20^\circ$  FOV and sensitive area of  $0.08 \text{ cm}^2$ ; the sensitive area is equivalent to a  $5 \times 11 \text{ mm}$  grating sensitive area multiplied by a total grating geometric transparency of 0.14. For a nightglow intensity  $3600 R$ ,<sup>273</sup> the background photon flux into an instrument would be  $\approx 2 \times 10^6 \text{ s}^{-1}$  in the 400–1400 Å spectral range. The incident background photons would trigger the detectors both directly and via photoelectrons emitted from the ultrathin foil. The resulting  $(1-5) \times 10^4$  detector count rate can be tolerated by MCPs, but it would lead to a random coincidence rate  $> 50 \text{ s}^{-1}$  unacceptably high for ENA measurements. Thus ENA measurements by unprotected direct-exposure instruments are practically impossible in the presence of nightglow and entirely impossible in the presence of the much brighter dayglow.

For an instrument with a single transmission grating filter at the entrance and identical geometric factor (i.e., a  $10^\circ \times 20^\circ$  FOV and sensitive area  $5 \times 11 \text{ mm}$ ), the detector background count rates would be about 1 and  $30 \text{ s}^{-1}$  in the presence of nightglow and dayglow, respectively. For such counting rates the random coincidences are negligible. Thus transmission grating filters would make it possible to use the direct-exposure ENA instruments, which are most sensitive to background radiation, even in the presence of dayglow.

## G. Interaction with surfaces

Detection of ultralow-energy (from few eV up to several hundred eV) ENAs in space presents a special challenge. The ENA energy is not sufficient to pass through an ultrathin foil, and foil stripping efficiency and electron emission yield fall dramatically. ENA number densities are  $< 1 \text{ cm}^{-3}$ . The lowest density that can be detected by a state-of-the-art neutral gas mass spectrometer, such as on Cassini, is about  $4 \times 10^4 \text{ cm}^{-3}$ . In some exceptional cases,<sup>469</sup> when an instrument is deeply cooled (as it was on Apollo 17 during lunar nighttime), the sensitivity can be improved to  $10^2 \text{ cm}^{-3}$ . Therefore any conventional technique based on electron impact ionization of neutrals and subsequent analysis and detection of the ions is not applicable for ENAs.

The idea behind an alternative approach with a much better sensitivity is to use an instrument sensitive to the flux of neutral particles instead of an instrument sensitive to the neutral particle number density. Even a small (1–20 km/s) neutral particle velocity relative to the spacecraft would result in a large flux of atoms into the instrument, and even a small detection efficiency of individual atoms would result in high sensitivity to the neutral particle density.

## 1. Secondary ion emission

A straightforward approach to build an instrument sensitive to the particle flux is to use secondary electron or secondary ion emission from a sensitive surface bombarded by the incoming ENA flux. An example of a secondary ion emission instrument is the interstellar neutral helium detector on Ulysses (see Sec. VII C 1).<sup>175,176</sup> A similar approach was used in the PIPPI-MCP instrument on ASTRID to detect magnetospheric ENAs.<sup>22,23</sup> Measuring ENAs using secondary electrons is virtually impossible because of the superior background photoelectron emission. Secondary ion emission instruments allow particle detection without the capability of energy or mass analysis, and consequently such instruments have limited applications.

## 2. Surface conversion to negative ions

An alternative approach to measure ultralow-energy ENAs in space, first suggested in 1983,<sup>177</sup> was formulated in detail in the early 1990s.<sup>470</sup> The technique is based on the surface neutral-to-negative ion conversion, followed by mass analysis and detection of the negative ions.<sup>10</sup> It is important that negative ions are usually absent in space plasma. In addition, all charged particles with energies  $< 100 \text{ keV}$  are prevented from entering ENA instruments by deflectors. Hence the detected negative ions are uniquely due to the interaction of the incoming neutral atom flux with the conversion surface.

Negative ion conversion techniques have been well developed for the production of high-intensity negative H and D ion beams that, after stripping, are used for fusion plasma energy pumping.<sup>471,472</sup> The conversion on surfaces into negative ions was first suggested for fusion plasma corpuscular diagnostics in the late 1970s.<sup>473,474</sup> This detection application of the effect was emphasized later<sup>475–477</sup> and a practical device was finally built in the early 1990s.<sup>312,313</sup> The surface conversion technique is sometimes misidentified with secondary ion emission (Section VI G 1); these two techniques are based on different physical processes.

Various surfaces can be used as converters of impinging neutral atoms and molecules into negative ions. Atom conversion is generally described by electron tunneling to the classically moving atom. The negative ion yield is a convolution of the reflection coefficient and the charge transfer probability.<sup>10,471,478,479</sup> The affinity level of the atom approaching the metal surface gradually shifts due to the attractive interaction with its image charge in the metal.<sup>480</sup> At a certain distance from the surface the shifted level crosses the level of the work function of the metal so that electrons can tunnel through and be captured by the atom. The initially sharp affinity level is broadened into a band of a finite width. The distance from the surface at which electrons can be captured is  $6-8a_0$  ( $a_0$  is a Bohr radius) for a partially cesium covered tungsten substrate.<sup>481</sup>

After reflection from the surface, on the outbound leg of the particle trajectory when the affinity level becomes again higher than the work function level the electron may tunnel from the negative ion back to the empty metal states. Such a model corresponds to a zero temperature surface, and the



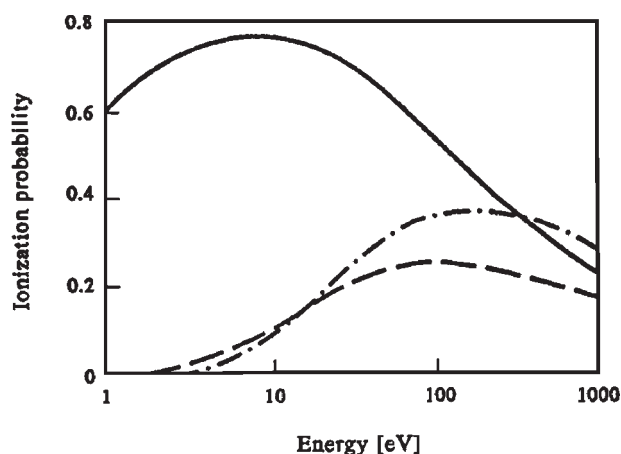


FIG. 26. Calculated negative-ion formation probability for H atoms leaving the surface along the normal vs energy. The solid line is for half a monolayer Cs coverage, the dashed line is for full monolayer Cs coverage, and the chain-dashed line is for a thick Ba coverage of the W(110) surface. (After Ref. 483.)

conversion to a negative ion has an energy threshold equal to the difference between the work function and the unperturbed affinity energy.<sup>479</sup> If the converter temperature is not zero, then the electron distribution is smeared around the Fermi level.<sup>482</sup> This level smearing as well as broadening of the ion affinity level would allow electrons tunneling both ways when the particle is within a certain range of distances from the surface and would result in lowering of the effective energy threshold.

Knowing the electron transition frequency, it is possible to calculate the equilibrium probability for the atom to be negatively charged at a certain distance from the surface. Introducing further the motion of the atom (described classically) and integrating the rate equation, one can determine the probability that the atom leaves the surface as a negative ion. The charge transfer probability depends on both components of the atom velocity, parallel and perpendicular to the surface. For ENA velocities much smaller than the velocities of surface electrons, the charge transfer probability is determined mostly by the velocity component normal to the surface.<sup>481</sup> The highest conversion efficiencies are characteristic of surfaces with a low work function and a high density of electron states at the Fermi level. The most developed and well studied conversion surfaces are metals covered by alkali layers, e.g., by cesium, which provide the highest values of conversion efficiency.

As an example, the calculated normal-energy dependence (supported by the experimental data) of negative hydrogen ion formation is shown for three different surfaces in Fig. 26.<sup>483</sup> For hydrogen ENAs with a normal velocity of 35 km/s ( $\sim 6.4$  eV) the fraction of negative ions among the particles reflected from the tungsten surface W(100) covered by a thick layer of cesium, is 5%–7%. A very thin cesium layer (half a monolayer) may give a much higher negative ion fraction.<sup>481</sup> However, there are difficulties in maintaining such a surface in a space instrument, and the use of a thick cesium layer may be preferable. An overall conversion coefficient of several percent could be expected for such hydrogen ENAs.<sup>483–485</sup>

The work function of the surface is very sensitive to the degree of its coverage by cesium. For example, a clean surface of an *n*-type (100) silicon substrate has a work function 4.75 eV, while the work function is 2.00 and 1.47 eV for the same surface covered by a monolayer of cesium and by a half of a monolayer of cesium, respectively.<sup>486</sup> Controlled oxidation of cesium may lead to further lowering of the work function down to 0.9 eV. For thick layers of cesium oxides, where the substrate is not crucial, work functions of the order of 1 eV have been reported.<sup>486,487</sup> Sputtering and implantation processes are unimportant for a bombardment by low energy neutral atoms, and complex multicomponent converters of cesium oxides—a mixture of Cs/Cs<sub>2</sub>O/Cs<sub>2</sub>O<sub>2</sub>—can be used for ENA detection. Such promising surfaces can be several hundred angstroms thick, their work functions are independent of the substrate compositions, and the cesium oxides have a vapor pressure much lower than pure cesium.<sup>487</sup> An exposure of oxygenated cesium surfaces to large fluxes of hydrogen may result in changes of about  $\pm 0.1$  eV of work function.<sup>486</sup>

The photoemission properties of the conversion surface would depend strongly on its work function. Hence, the measurement of photoelectron emission could be used in flight instruments to monitor conditions on the conversion surface.<sup>10,258</sup> Cesium surfaces, although providing high conversion efficiencies, are not easy to maintain. Cesium has also a high vapor pressure, which could lead to instrument contamination. Metal surfaces covered by layers of alkalis other than cesium, such as Na, Rb and K can also be used for detection of hydrogen ENAs.<sup>477,484</sup>

Barium recently emerged as an efficient conversion surface.<sup>471,483,487,488</sup> Barium is a much more stable and convenient material to use although initial activation—by heating<sup>487</sup> up to 1200 K or by sputtering off several surface atomic layers—is needed to eliminate the oxide layer and provide a metal-type surface. The ambient space plasma can be used to sputter the conversion surface: plasma ions could be sucked in, focused, and accelerated for such a purpose. The low density of the solar wind plasma may require several days of sputtering to accumulate the necessary dose. Another possible surfaces under the study are LaB<sub>6</sub> that also requires heating to a temperature 1400 K for activation<sup>471</sup> and diamond.<sup>489,490</sup>

Different metals, such as W and Mo,<sup>491</sup> as well as Mg, Cu, Au, and Pt also may serve as a conversion surface, although the typical conversion efficiencies are usually very low:  $10^{-4}$ – $10^{-6}$ . Such low efficiencies are high enough however to measure 5 eV oxygen atom fluxes at low earth orbit. The selection of the type of the conversion surface and a way to activate and control it, as well as the stability of the surface and the necessity to refresh it during a long duration space flight require further detailed study.

The process of neutral surface conversion to negative ions has an energy (normal component) threshold equal to the difference between the surface work function and electron affinity of the particle. All atoms and molecules that have a positive electron affinity can form negative ions and can be studied by the conversion technique. Electron affinities of hydrogen (deuterium) and oxygen atoms that are of

TABLE II. Work functions of conversion surfaces used in experiments.<sup>a</sup>

Surface	Work function (eV)
Cs/Cs <sub>2</sub> O/Cs <sub>2</sub> O <sub>2</sub>	0.90–1.45
Cs (0.5 ML on W (100))	1.45
Cs (0.5 ML on Si(100))	1.45
Cs (1 ML on Si(100))	2.00
Si(100) <i>n</i> -type	4.75
Ba/BaO	1.8–2.2
Ba	2.5
W(100)	4.6
Na	2.7
K	2.2
Rb	2.1
LaB <sub>6</sub>	2.3–2.6
Ni(110)	5.04
Cu(111)	4.9
Pt(111)	5.7
Ag(111)	4.7
diamond (111)	5.4
Li	2.9
Mo(111)	4.6
ThO <sub>2</sub>	3.0–4.0

<sup>a</sup>After Ref. 10.

great interest for the heliospheric, magnetospheric, ionospheric, and atmospheric ENA studies are 0.74 and 1.46 eV, respectively. Work functions of various surfaces that have been used for particle conversion are presented in Table II; some of these surfaces are especially promising for space applications.<sup>10</sup>

Only the conversion of hydrogen and deuterium atoms with  $E > 100$  eV has been studied extensively. Conversion of a few other species was also measured: O,<sup>492</sup> C,<sup>492,493</sup> C<sub>2</sub>,<sup>494</sup> O<sub>2</sub>,<sup>495,496</sup> and I<sub>2</sub>.<sup>489</sup> Although surface production of negative ions is qualitatively understood, quantitative agreement between theory and experiment has been achieved only by adjusting some parameter (usually screening distance). Consequently, one has to be cautious in making specific numerical predictions of energy thresholds and conversion probabilities without experimental verification.

Special consideration should be given to the possibility of measuring helium ENA fluxes. Helium ENAs that carry important scientific information are expected in both magnetospheric and heliospheric environment. The surface conversion technique was originally proposed for *in situ* measurement of ultralow-energy hydrogen, deuterium, and oxygen ENA fluxes.<sup>10,470</sup> Later it was asserted that the technique would be efficient for detection of helium ENAs, too.<sup>257,258</sup>

Helium is known to have very weakly bound (0.076 eV) metastable negative ion state He<sup>−</sup>(<sup>4</sup>P).<sup>497,498</sup> He<sup>−</sup> can be formed from neutral He in an excited <sup>3</sup>S state 19.8 eV above the ground state level, and helium conversion to negative ions was demonstrated only on Na surfaces.<sup>476,499</sup> The maximum negative fraction peaked at 0.14%,<sup>476,499</sup> and not at 14% as was erroneously stated.<sup>257</sup> This maximum yield is achieved for helium ions leaving the surface with energies in the 8–12 keV range. The negative fraction yield rapidly falls down to 0.02% with the energy decreasing to 2 keV. It was found that helium conversion efficiency dramatically depends on cleanness of the Na surface and is especially sen-

sitive to the surface contamination by carbon and oxygen.<sup>476</sup>

The ENA conversion efficiency is a convolution of the reflection coefficient and the energy-dependent negative charge fraction yield. The energy dependence of negative fraction yield is determined by the physical mechanism<sup>476,499</sup> that requires helium initial excitation to a highly energetic state. Such an excitation may occur only in rare close collisions with target atoms,<sup>499</sup> and the probability of such collisions would precipitously decrease with the decreasing particle energy. Weakly bound metastable He<sup>−</sup> is susceptible to destruction through deexcitation in the vicinity of the surface, and the probability of leaving the surface as a negative ion would also decrease with the decreasing ion energy. These effects result in vanishing conversion efficiency for incident He energies less than several hundred eV, which makes the technique inapplicable for ultralow-energy helium ENAs.

The potential problem for the surface conversion technique is a possibility of producing negative ions by sputtering previously adsorbed atoms and molecules. Energetic ions with energy  $> 100$ –200 keV (flux  $1 \text{ cm}^{-2} \text{ s}^{-1} \text{ sr}^{-1}$  at 1 AU from the Sun) would pass the ion deflector at the entrance and would hit the conversion surface, sputtering negative ions. Photosputtering of surface atoms<sup>500</sup> by the background EUV/UV radiation may also contribute to negative ion production. Most of the surface contamination may come from the adsorption of atoms and molecules outgassing from the instrument elements and the spacecraft itself. Therefore a special effort must be devoted to maintaining a clean conversion surface in the instrument.

## VII. REPRESENTATIVE ENA INSTRUMENTS

### A. High-energy ENA instruments

#### 1 Solid-state detector instrument on CRRES

A medium energy ion and neutral atom spectrometer was flown on the Combined Release and Radiation Effects Satellite (CRRES) in 1991 in a low-earth orbit.<sup>125</sup> The instrument was capable of measuring ENA flux and energy with the imaging capabilities provided by spacecraft pointing. The measurement technique was based on ion momentum per charge separation in a 7 kG magnetic field followed by particle detection by solid-state detectors (Fig. 27).<sup>21</sup> A sensor, located directly in line with the collimator, measured magnetospheric ENAs and had an ion rejection up to  $\sim 50 \text{ MeV amu/q}^2$ . The ENA detector was of *p*-type silicon to improve light rejection and reduce radiation damage; a  $20 \mu\text{g/cm}^2$  aluminum surface deposit determined energy thresholds for particles.

The signal from the ENA solid-state detector was pulse-height analyzed with an 8-bit resolution in 256 levels, providing information on total particle energy. To reduce noise, silicon sensors, preamplifiers, and electronic box were cooled down to  $-55$ ,  $-12$ , and  $0^\circ\text{C}$ , respectively. A rather small instrument geometrical factor ( $10^{-3}$ – $10^{-2} \text{ cm}^2 \text{ sr}$ ) results in low count rates and very limited imaging capabilities. For example, the integral ENA count rate above 40 keV at 600 km altitude is about  $1 \text{ s}^{-1}$  during a large geomagnetic storm.<sup>125</sup>

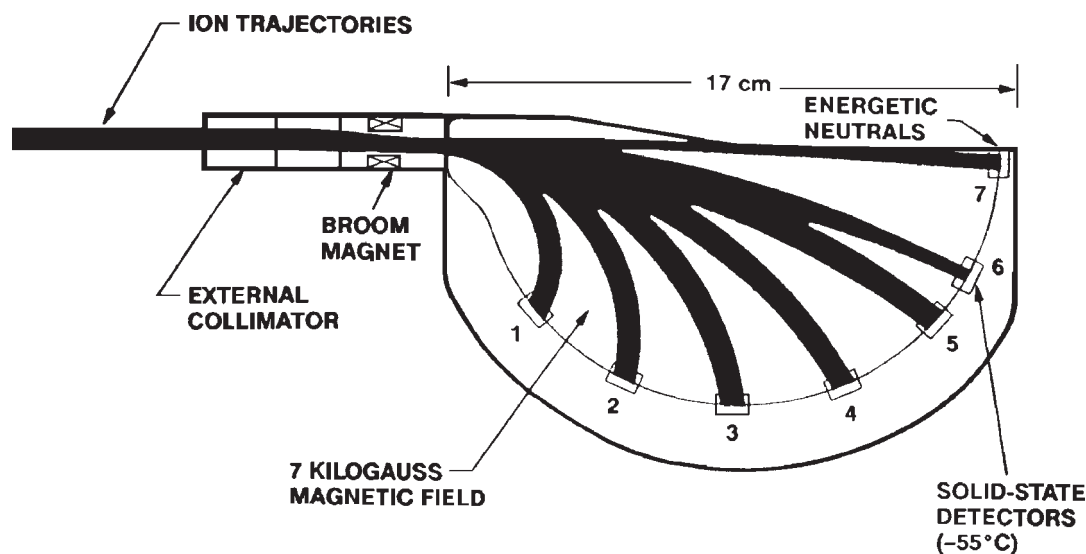


FIG. 27. Principle of operation of the medium energy ion and neutral atom spectrometer on CRRES which is based on ion momentum, mass defect, and energy analysis using a 7 kG magnet and an array of cooled solid-state sensors. (After Ref. 21.)

The strong magnetic field in a 5 mm entrance gap was produced by SmCo permanent magnets. An iron yoke completely surrounded the magnetic field except the entrance aperture, for reduction of the magnetic stray fields. Shape

and dimensions of the yoke were optimized to reduce the instrument mass (5.7 kg). The advantages of the instrument include simplicity, particle energy analysis, and low power consumption; the disadvantages are related to small geometrical throughput and lack of internal imaging capabilities.

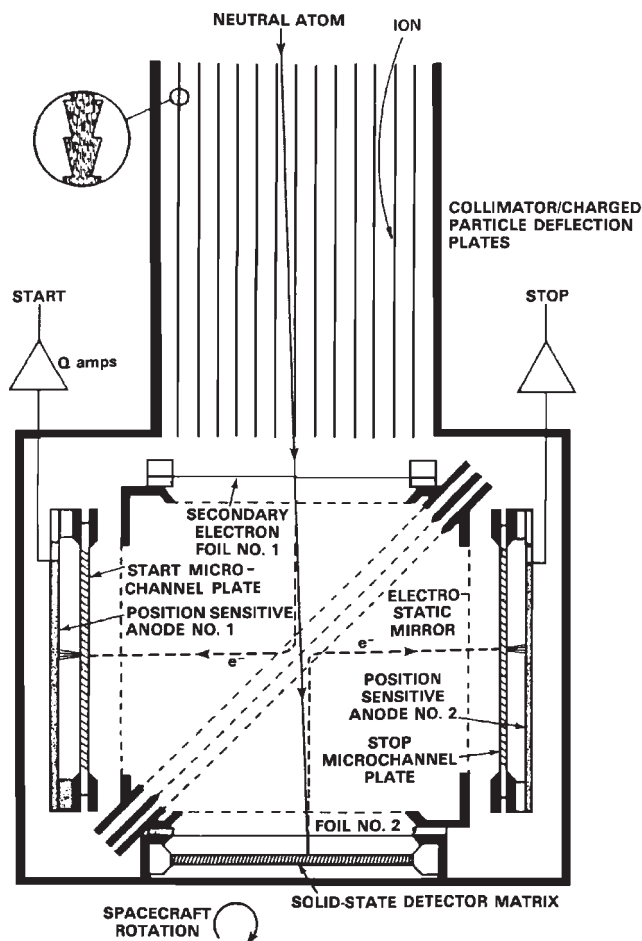


FIG. 28. Schematic of the high-energy ENA imager, which consists of a collimator/deflector, an imaging TOF detector for measuring the arrival direction and velocity of the incoming neutrals, and a solid state detector for measuring their energy. (After Ref. 111.)

## 2. High-energy neutral particle imager

A powerful high-energy ENA imager with mass identification capabilities is shown in Fig. 28.<sup>111</sup> A simplified conceptually similar instrument has been launched as a part of the HEP instrument on the GEOTAIL spacecraft.<sup>20</sup> The parallel plates at the instrument<sup>111</sup> entrance collimate ENAs in one dimension and eliminate (deflect) incoming charged particles. Plate serration reduces particle forward scattering into the sensor. An incoming ENA passes through two thin foils at the front (foil no. 1) and back (foil no. 2) of the sensor. The secondary electrons emitted from the foils are accelerated toward a central electrostatic mirror and directed toward two MCP-based position-sensitive detectors, which are also START and STOP detectors for the TOF analyzer.

The measured positions of the electron impinging on the MCP detectors are used for reconstruction of the particle trajectory in the sensor, and correspondingly the incoming ENA trajectory (flight direction). The uncertainty in the trajectory resulted from

- (1) ENA scattering in the foil No. 1 and
- (2) the effect of initial electron energy on electron transport in electrostatic mirrors.

The electrostatic mirrors are isochronous for electrons emitted from both foil No. 1 and foil No. 2, and the measurement of the time interval between electron detections establishes particle velocity in the sensor. After passage of an incoming ENA through both foils, its total energy is measured by a solid-state detector.

The imager determines ENA trajectory, ENA velocity, and energy (and correspondingly mass). ENA detection requires signals from all three detectors, two MCP detectors

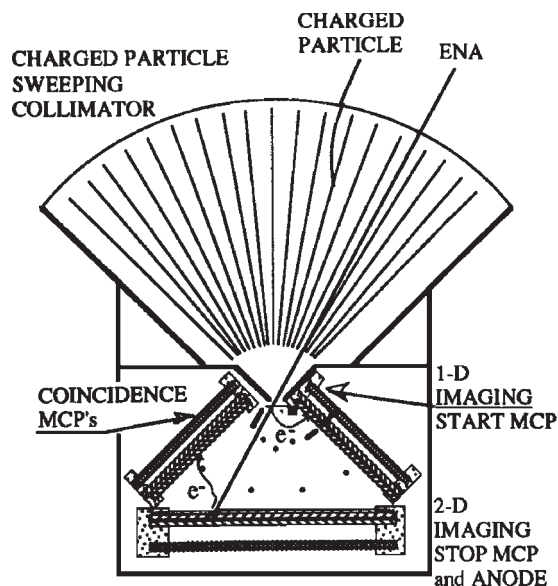


FIG. 29. Schematic of the ion neutral camera (INCA) head, side view. ENA penetrates the front foil (located in horizontal piece across narrow entrance gap), producing secondary electrons, and travels to the back foil in front of the two-dimensional imaging MCP position-sensitive detector. Dots indicate the location of wire electrodes for secondary electron steering. (After Ref. 24.)

and a solid-state detector, within a well defined time interval ( $< 200$  ns). The triple coincidence requirement assures virtually noise-free ENA detection. If an ion with high energy, say  $> 1$  MeV, passes through the deflector, its energy and/or velocity are measured by the instrument, and such an event would be rejected as a non-ENA detection.

Background EUV/UV photons would produce photoelectrons from the thin foils triggering MCP detectors. Foil No. 1 must be thick enough (e.g.,  $> 600$  Å) to attenuate the EUV/UV to an acceptable level, so that MCP detectors are not swamped by noise counts (i.e., keep count rates  $< 1000$  s $^{-1}$ ). The thin foil and the energy threshold of the solid-state detector establish instrument energy threshold at  $> (10-20)$  keV/nucleon.

### 3. ENA imaging camera INCA on Cassini

The ion neutral camera (INCA), probably the most advanced ever-built ENA instrument, was developed for the

Cassini mission (launch October 1997) to Saturn (Fig. 29).<sup>24</sup> The INCA's entrance includes a serrated plate fan charged particle deflector with a FOV of  $90^\circ \times 120^\circ$ . The deflector plates are constructed of epoxy graphite composite and coated with a conductive coating.<sup>24</sup> The plates are serrated to minimize ENA forward scattering, and electric potentials up to  $\pm 6$  kV are applied to the alternate plates. The deflector prevents charged particles with energies up to 500 keV/e from entering the instrument.

A specially designed three-layer foil<sup>438,501</sup> at the entrance slit is  $9.5 \mu\text{g}/\text{cm}^2$  Si,  $6.0 \mu\text{g}/\text{cm}^2$  Lexan, and  $3.0 \mu\text{g}/\text{cm}^2$  C. The foil composition is optimized to maximize UV suppression while providing high electron yield.<sup>438</sup> The foil attenuates 1216 Å radiation by four orders of magnitude, and it would scatter incoming 50 keV protons by  $5^\circ$  (FWHM) and 200 keV O by  $7^\circ$ .

Secondary electrons emitted from the entrance foil are steered toward the imaging one-dimensional MCP detector, which determines the ENA entrance coordinate normal to the plane of Fig. 29 and produces a START signal for the TOF analyzer. A two-dimensional imaging MCP detector fixes particle position at the back of the sensor and provides a STOP signal for the TOF analyzer. Electrons backward emitted from a thin foil at the entrance of the stop MCP detector are directed toward a coincidence MCP detector.

The measured particle coordinates allow reconstruction of a two-dimensional ENA trajectory within the instrument  $90^\circ \times 120^\circ$  FOV; the time interval between signals from the START and STOP detectors determine particle velocity inside the sensor. The triple coincidence ENA detection efficiently suppresses noise. A triple coincidence random noise rate due to background EUV/UV radiation is expected to be about seven events per year.<sup>24</sup>

The secondary electrons forward emitted from the foil in front of the STOP detector are accelerated into the stop MCP detector. The ENAs with identical velocities but different masses would have different energies (proportional to particle mass). Different energy losses in the foil result in a different number of the forward emitted electrons. INCA can reliably distinguish between hydrogen and oxygen ENAs by recording the pulse height of the MCP signal.<sup>24</sup>

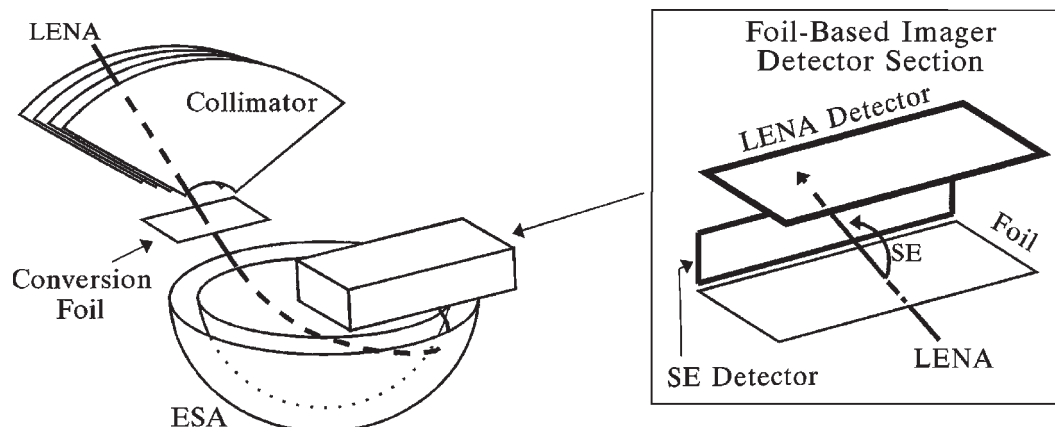


FIG. 30. Schematic of the advanced low-energy ENA imager for a spinning spacecraft. (LENA) low-energy ENA, (ESA) electrostatic analyzer, and (SE) secondary electron. (After Ref. 216.)



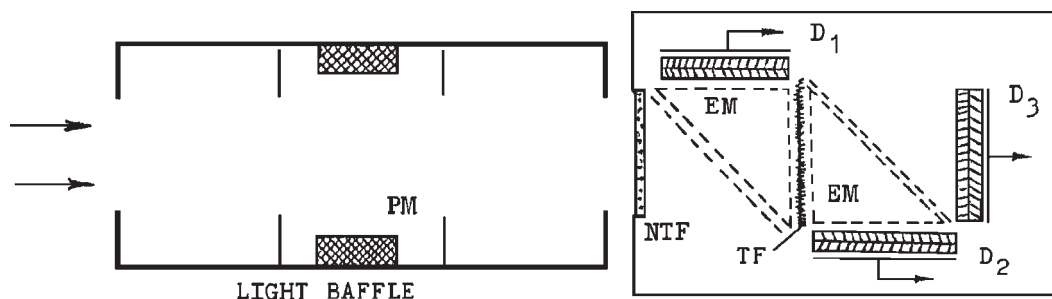


FIG. 31. Schematic of the direct-exposure low-energy ENA instrument for neutral solar wind studies. (PM) permanent magnet, (EM) electrostatic mirror; (TF) ultrathin foil; (NTF) optional diffraction (nuclear track) filter; and ( $D_1, D_2, D_3$ ) MCP detectors. (After Ref. 182.)

## B. Low-energy ENA instruments

### 1. ENA foil stripping analyzer

The first flown ENA instrument<sup>119,212</sup> was based on ENA stripping in an ultrathin foil and subsequent analysis and detection of positive ions by a simple electrostatic analyzer (Fig. 8). The technique of ion energy and mass analysis significantly improved since then, and much more sophisticated, efficient and compact analyzers were developed.

An advanced foil stripping ENA imager<sup>216</sup> for a spinning spacecraft is shown in Fig. 30. Low-energy ENAs transit a collimator that sets polar and azimuthal fields of view and passes through a  $1.1 \mu\text{g}/\text{cm}^2$  carbon foil. The ionized (stripped) ENAs enter a hemispheric electrostatic analyzer. Most of the stripped ENAs are singly charged, and if an ion energy is within the electrostatic analyzer passband, it would reach the ion detector.

The ion detector itself is a combination of another ultrathin foil and two MCP position-sensitive detectors. An ion transiting this second foil produces secondary electron emission. Measurement of the coordinates of both electron and particle impact positions allows reconstruction of the trajectory of the incident ENA. The time interval between electron and particle detections establishes the velocity of the ion and efficiently suppresses noise counts as well. Since the ion energy was selected by electrostatic analyzer, the ENA's mass can be determined. (Introduction of the diffraction filters allows one to use the first foil for generation of the START signal.<sup>182,230,231</sup> Thus it would become possible to combine energy and TOF analyses in a simpler configuration with one thin foil only.<sup>502</sup>)

The ENA imager design (Fig. 30) allows one to build instruments with such exceptionally large geometrical factors as  $1 (\text{cm}^2 \text{ sr keV})/\text{keV}$ , especially suitable for detection of weak ENA fluxes.<sup>216</sup> The instrument's instantaneous FOV could be  $120^\circ \times 2^\circ$  with  $120^\circ \times 360^\circ$  coverage during one spacecraft spin; the nominal angular resolution is  $2^\circ \times 2^\circ$  FWHM and the energy range 0.8–30 keV for hydrogen ENAs.

### 2. ENA direct-exposure analyzer

A direct-exposure ENA instrument was developed to study the solar wind neutral component.<sup>182,217</sup> It consists of a collimator/baffle, permanent magnet deflector, optional diffraction filter, and an ultrathin foil TOF analyzer (Fig. 31). When a background EUV/UV photon enters the analyzer, it

may be either absorbed by the foil (with possible photoelectron emission and triggering of an electron detector,  $D_1$  or  $D_2$ ) or pass through the foil and trigger the “particle” detector,  $D_3$ . An ENA arrival may result in triggering both the electron detector (or two electron detectors) and the particle detector. Thus one can extract a weak signal due to ENAs from the superior photon background by counting double or triple coincidences. By measuring time intervals between the detections of electrons and corresponding particles one determines ENA velocity distribution. The FOV and sensitive area of the sensor are restricted by the requirement to limit MCP count rates by  $<10^4 \text{ s}^{-1}$ .

ENA detection efficiency (the probability to produce a TOF event) is determined by the efficiency of electron emission from the foil and particle detection by  $D_3$ , and it decreases with the decreasing energy from 15% at  $E = 3000 \text{ eV}$  down to  $\sim 0.5\%$  at  $E = 600 \text{ eV}$ . Energy (velocity) resolution of the instrument is determined by straggling and scattering in the ultrathin foil; it is about  $E/\Delta E \approx 2$  at  $E = 1000 \text{ eV}$ , and it improves with the increasing ENA energy.<sup>182,217</sup> The diffraction filter (NTF in Fig. 31) technology was not developed at the time of building the neutral solar wind instrument. Recently introduced transmission grating filters (Sec. VI F) make it possible to build a conceptually similar highly efficient compact ENA analyzers with internal imaging capabilities. Such instruments would be especially attractive for applications when miniaturization is required.

## C. Ultralow-energy ENA instruments

### 1. Secondary ion emission instrument GAS on Ulysses

The Ulysses GAS experiment is designed to directly measure the flux of interstellar helium in the solar system.<sup>153,154,174–176</sup> The instrument (Fig. 32) is based on secondary emissions from a lithium fluoride (LiF) surface bombarded by the ultralow-energy (30–100 eV) interstellar helium atoms. The incoming ENAs are converted into secondary electrons and ions, and depending on the polarity of the accelerating voltage either electrons or positive ions can be accelerated and detected by CEMs. The instrument consists of two independent detection channels with different FOV, light baffle, electrostatic deflector, LiF furnace for in-flight refreshing of the sensitive surfaces, and a quartz crystal to monitor LiF deposition.<sup>176</sup> An integrated turntable in con-

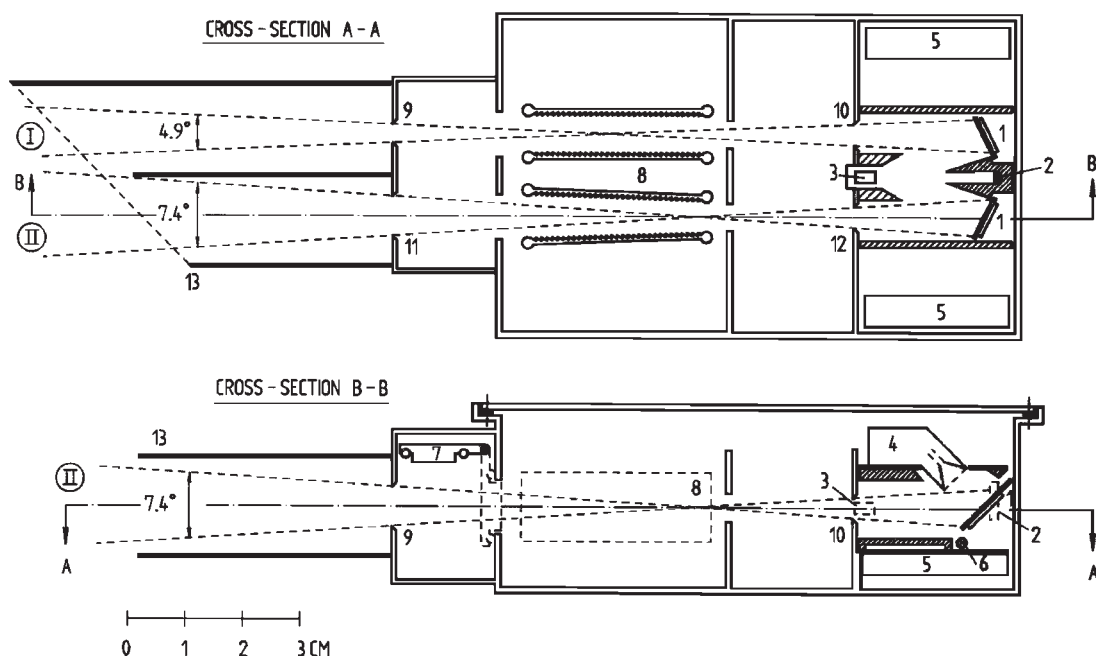


FIG. 32. Cross sections of the sensor head (schematic) of instrument GAS on Ulysses, (1) conversion plate with heater, evaporated with lithium-fluoride (LiF), (2) quartz crystal for monitoring LiF evaporation process, (3) furnace LiF supply, (4) CEM, (5) CEM electronics, (6) tungsten filaments to stimulate CEMs, (7) vacuum-tight cover in closed (dashed lines) and open position, (8) electrostatic deflection system, (9,10,11,12) circular apertures defining the FOV of channel I and II, (13) light baffle. (After Ref. 176.)

junction with the spin of the spacecraft permits scanning of the celestial sphere with resolution of a few degrees.

A clever choice of the sensitive surface material was crucial to the success of this experiment. In order to maximize secondary ion emission, the choice of the surface material is determined by the requirement to contain relatively light atomic species to facilitate momentum transfer in collisions with impinging helium atoms. To minimize photon scattering and electron emission due to EUV/UV background (mostly H I Ly- $\alpha$  1216 Å), the material should be transparent to radiation. Lithium fluoride is the material of choice that provides high yield up to several percent of  $\text{Li}^+$  ions. Photo-sputtering of LiF by EUV/UV radiation is not a problem in this application, although one has to be cautious since experimental data on photosputtering of earth alkalis are scarce.<sup>500,503</sup>

The maximum Ly- $\alpha$  suppression requires the highest possible transparency of the sensitive surface material. Freshly deposited LiF layers are highly transparent to Ly- $\alpha$ , but after some time photoelectron emission increases. Even a small absorption of radiation (that is photon interaction with material electrons) would increase photoelectron emission. Surface layer modification would also increase photon scattering and adversely affect secondary ion emission. Therefore the instrument sensitive surface is refreshed periodically in flight by depositing several new layers of LiF. A tiny furnace, filled with 2 mm<sup>3</sup> of LiF, is heated by telecommand up to about 600 °C, where mild evaporation of LiF refreshes the sensitive surface. Special custom-made miniature CEMs with low intrinsic noise are used as detectors. The small detector size minimizes the noise count rate due to penetrating cosmic radiation and to  $\gamma$  rays from the radioisotope

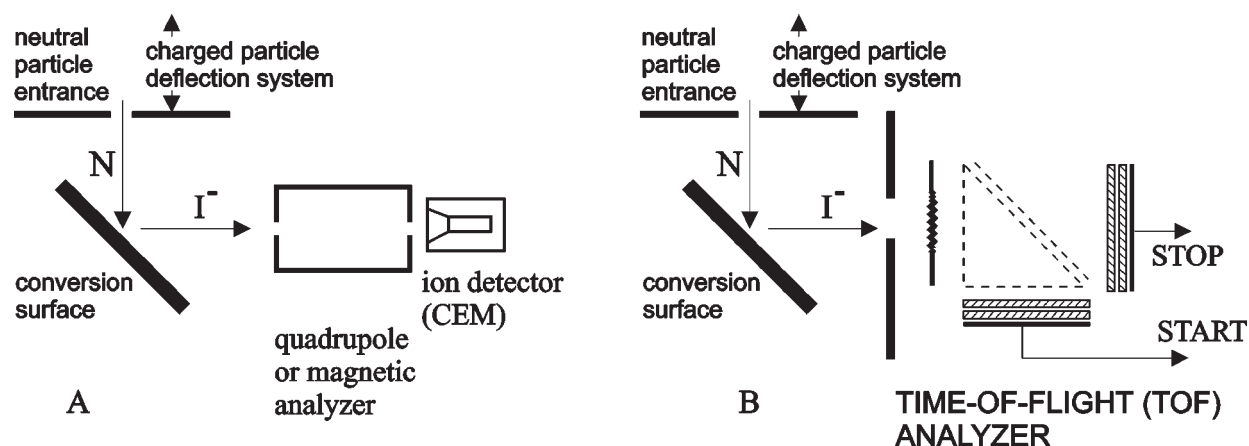


FIG. 33. Schematic of ultralow-energy surface conversion ENA instruments. (A) Accelerated negative ions are mass analyzed by the mass analyzer (e.g., magnetic or quadrupole) and detected by a simple CEM detector. (B) Accelerated negative ions are detected and mass analyzed by a TOF analyzer.

thermal generator (RTG) that provides power to the spacecraft.

Most of the interstellar helium measurements are performed in the secondary ion counting mode. In this mode the EUV/UV background is nearly completely suppressed since photoelectrons released from the surface cannot reach the CEM entrance because of its bias voltage; photons cannot reach it either because the CEM is placed in “shadow.”

## 2. Conversion surface instruments

Detection of ultralow energy ENAs by surface conversion to negative ions is an emerging field of space instrumentation driven by potential science return. A possible schematic of ultralow-energy ENA instruments is shown in Fig. 33. The instrument design can be optimized depending on the species to be measured and experimental requirements. If only a few species are to be detected and the neutral particle flux is relatively high, for example O atoms at low earth orbit, then negative ions formed at the conversion surface can be accelerated up to a certain voltage, pass through a mass analyzer (e.g., quadrupole or magnetic) and be detected by an ion detector [Fig. 33(A)]. Such an application does not require highly efficient conversion, and simple and stable surfaces (e.g., gold) can be used.

For low-intensity magnetospheric and heliospheric ENA fluxes, the negative ions are accelerated and separated (not shown) from electrons and photons, mass analyzed and detected in a noise-free mode by a TOF analyzer [Fig. 33(B)]. Various designs of ion analyzers can be effectively employed for negative ion collection, separation from electrons and photons, and ion mass analysis.<sup>10,11,257,258,504</sup>

## VIII. DISCUSSION

Almost three decades of ENA instrument development led to practical implementation of ENA imaging of space plasmas. Dedicated simple ENA instruments were recently flown on CRRES<sup>21</sup> and ASTRID<sup>22,23</sup> missions in low-earth orbit. A sophisticated first large-size ENA camera<sup>24</sup> will perform imaging of the Saturn's magnetosphere on the Cassini mission to be launched in October 1997. ENA instruments covering a broad energy range will image the terrestrial magnetosphere on the IMAGE mission to be launched in January 2000. Several other space missions are in different stages of planning and design. Simultaneous magnetosphere imaging from several spatially separated spacecraft will open the way for stereoscopic imaging.<sup>505</sup>

ENA instrument development continues with the emphasis on expanding energy range, improving mass, and energy identification capabilities and imaging resolution. Increase in instrument geometric factor (throughput) remains an ever-present issue, in particular for compact instruments.

### A. High-energy ENA instrumentation

One can expect further integration of electronics with multianode solid-state detectors, increasing number and size of individual anodes and performing as much as possible signal handling on the detector substrate. An INCA imager and various instruments on its basis are suitable for flying on

many missions and will provide the most detailed information on characteristics of high-energy ENAs in space.

### B. Low-energy ENA instrumentation

The foil-stripping technique is mature and ready for applications on a variety of missions. A large foil-stripping imager, as in Fig. 30, would provide a breakthrough in imaging of the terrestrial magnetosphere. A combination of newly developed transmission grating diffraction filters with the direct-exposure technique would allow building a new generation of highly efficient ENA imagers with the wide (0.5–70 keV) energy range. Diffraction filters will allow one to improve EUV/UV noise suppression in various other ENA instruments.

### C. Ultralow-energy ENA instrumentation

Possible applications of the secondary ion emission technique are limited, since it is not capable of mass and energy analysis, and thus can be used efficiently only when composition and energy of incoming particles are known and the goal is to establish ENA angular distribution (i.e., to obtain the image). The technique can be further improved by secondary electron-secondary ion coincidence detection that would introduce new imaging and noise-suppression capabilities.<sup>392</sup>

An exceptionally promising surface conversion-to-negative ions technique when fully developed will provide a tool for *in situ* study of interstellar gas, heliospheric, magnetospheric, and ionospheric ENAs, tenuous exospheres of planets, comets, and asteroids, as well as monitoring of atomic and molecular oxygen at the low earth orbit.<sup>10</sup> The technique requires extensive laboratory development, accumulation of an experimental database, and feasibility demonstration. It is necessary not only to convert ENAs to negative ions, but to confidently relate negative ion properties to those of incoming ENAs. The technique development and testing, as sometimes overlooked, requires the use of a reliable controlled beam of fast neutral atoms (a few eV–1000 eV) in the ground state. Even a small contamination of the beam by metastable atoms, which are routinely produced in charge exchange, may significantly distort the measurements.

## ACKNOWLEDGMENTS

The author benefitted enormously throughout many years from discussions on various issues related, directly or indirectly, to the study of energetic neutral atoms in space plasmas. Many colleagues provided insight, gave suggestions, sent articles prior to publication, participated in collaborative work, and provided encouragement. I am grateful to each and all of them. Although it is impossible to mention all, I would like to especially thank Ian Axford, Vladimir Baranov, Jean-Loup Bertaux, Ara Chutjian, Charles Curtis, Alex Dessler, Tony Donn , Hans Fahr, Priscilla Frisch, Herb Funsten, George Gloeckler, Lev Gorn, Stan Grzedzielski, Marek Hlond, Tom Holzer, Johnny Hsieh, Darrell Judge, Alexander Kalinin, Boris Khazanov, Rosine Lallement, Mike Lampton, Vlas Leonas, Vitalii Liechtenstein, Yurii Malama, Dave McComas, Don Mitchell, Alexander Mitro-

fanov, Eberhard Moebius, Ed Roelof, Helmut Rosenbauer, Marek Rubel, Daniel Rucinski, Earl Scime, Mark Schattenburg, Milos Seidl, Don Shemansky, Henk Voss, Berend Wilken, and Manfred Witte. This work was partially supported by NASA grants.

- <sup>1</sup>E. C. Roelof and D. J. Williams, Johns Hopkins APL Tech. Dig. **9**, 144 (1988).
- <sup>2</sup>E. C. Roelof and D. J. Williams, Johns Hopkins APL Tech. Dig. **11**, 72 (1990).
- <sup>3</sup>J. W. Freeman, Jr., in *Physics and Astrophysics from a Lunar Base*, AIP Conference Proceedings No. 202, edited by A. E. Potter and T. L. Wilson, (AIP, New York, 1990), pp. 9–16.
- <sup>4</sup>D. J. McComas *et al.*, Proc. Natl. Acad. Sci. USA **88**, 9598 (1991).
- <sup>5</sup>D. J. Williams *et al.*, Rev. Geophys. **30**, 183 (1992).
- <sup>6</sup>K. C. Hsieh *et al.*, Astrophys. J. **393**, 756 (1992).
- <sup>7</sup>Hsieh, K. C. *et al.*, in *Solar Wind Seven*, edited by E. Marsch and R. Schwenn (Pergamon, New York, 1992), pp. 365–368.
- <sup>8</sup>E. C. Roelof, in *Solar Wind Seven*, edited by E. Marsch and R. Schwenn, (Pergamon, New York, 1992), pp. 385–394.
- <sup>9</sup>M. A. Gruntman, Planet. Space Sci. **40**, 439 (1992).
- <sup>10</sup>M. A. Gruntman, Planet. Space Sci. **41**, 307 (1993).
- <sup>11</sup>K. C. Hsieh and M. A. Gruntman, Adv. Space Res. **13** (6), 131 (1993).
- <sup>12</sup>M. A. Gruntman, J. Geophys. Res. **99**, 19213 (1994).
- <sup>13</sup>E. C. Roelof, Eos Trans. AGU **65**, 1055 (1984).
- <sup>14</sup>H. D. Voss *et al.*, *Planetary Plasma Environments: A Comparative Study*, Proceedings of Yosemite '84 edited by C. R. Clauer and J. H. Waite, Jr. (AGU, Washington, DC, 1984), pp. 95–6.
- <sup>15</sup>J. W. Chamberlain, Planet. Space Sci. **11**, 901 (1963).
- <sup>16</sup>B. A. Tinsley, *Fundamentals of Cosmic Physics*, edited by A. G. W. Cameron (Gordon and Breach, New York, 1974), pp. 201–300.
- <sup>17</sup>J. W. Chamberlain and D. M. Hunten, *Theory of Planetary Atmospheres* (Academic, New York, 1987).
- <sup>18</sup>J.-L. Bertaux and J. E. Blamont, Space Res. **X**, 591 (1970).
- <sup>19</sup>R. R. Meier, Space Sci. Rev. **58**, 1 (1991).
- <sup>20</sup>T. Doke *et al.*, J. Geomag. Geoelectr. **46**, 713 (1994).
- <sup>21</sup>H. D. Voss *et al.*, J. Spacecr. Rockets **29**, 566 (1992).
- <sup>22</sup>S. Barabash *et al.*, *Abstracts, Chapman Conference on Measurement Techniques for Space Plasma*, (AGU, Santa Fe, NM, 1995), p. 50.
- <sup>23</sup>O. Norberg *et al.*, Proceedings of the 12th European Symposium on Rocket and Balloon Programmes and Related Research, Lillenhamer, Norway, 1995, pp. 273–7.
- <sup>24</sup>D. G. Mitchell *et al.*, Opt. Eng. **32**, 3096 (1993).
- <sup>25</sup>M. F. Smith *et al.*, *Instrumentation for Magnetospheric Imagery II*, Proc. SPIE 2008, edited by S. Chakrabarti, (SPIE, Bellingham, WA, 1993), pp. 41–56.
- <sup>26</sup>C. L. Johnson and M. Herrmann, Opt. Eng. **33**, 329 (1994).
- <sup>27</sup>L. A. Frank *et al.*, Opt. Eng. **33**, 391 (1994).
- <sup>28</sup>S. Orsini *et al.*, *Instrumentation for Magnetospheric Imagery*, Proc. SPIE 1744, edited by S. Chakrabarti, (SPIE, Bellingham, WA, 1992), pp. 91–101.
- <sup>29</sup>M. A. Gruntman, Eos Trans. AGU, Spring Meeting Suppl., **75** (16), 271 (1994).
- <sup>30</sup>J. A. Joselyn, Rev. Geophys. **33**, 383 (1995).
- <sup>31</sup>F. T. Tacsione and A. J. Preble, Eos Trans. AGU, Fall Meeting Suppl. **76** (46), F431 (1995).
- <sup>32</sup>E. Hildner, Eos Trans. AGU, Fall Meeting Suppl., **76** (46), F431 (1995).
- <sup>33</sup>V. V. Afrosimov and M. P. Petrov, Sov. Phys. Techn. Phys. **12**, 1467 (1968).
- <sup>34</sup>H. P. Eubank, in *Diagnostics for Fusion Experiments*, edited by E. Sindoni and C. Wharton (Pergamon, New York, 1979a), pp. 7–16.
- <sup>35</sup>M. Brusati, in *Diagnostics for Fusion Experiments*, edited by E. Sindoni and C. Wharton (Pergamon, New York, 1979), pp. 35–46.
- <sup>36</sup>I. H. Hutchinson, *Principles of Plasma Diagnostics* (Cambridge University Press, Cambridge, 1987).
- <sup>37</sup>G. Gloeckler and K. C. Hsieh, Nucl. Instrum. Methods **165**, 537 (1979).
- <sup>38</sup>B. Wilken *et al.*, Nucl. Instrum. Methods **196**, 161 (1982).
- <sup>39</sup>B. Wilken and W. Studemann, Nucl. Instrum. Methods **222**, 587 (1984).
- <sup>40</sup>B. Wilken, Rep. Prog. Phys. **47**, 767 (1984).
- <sup>41</sup>D. J. McComas and J. E. Nordholt, Rev. Sci. Instrum. **61**, 3095 (1990).
- <sup>42</sup>D. J. McComas *et al.*, Proc. Natl. Acad. Sci. USA **87**, 5925 (1990).
- <sup>43</sup>D. T. Young, in *Solar System Plasma Physics*, Geophysical Monograph **54**, edited by J. H. Waite Jr., J. L. Burch, and R. L. Moore (AGU, Washington, DC, 1989), pp. 143–157.
- <sup>44</sup>A. G. Ghielmetti and E. G. Shelley, Nucl. Instrum. Methods Phys. Res. A **298**, 181 (1990).
- <sup>45</sup>G. Gloeckler, Rev. Sci. Instrum. **61**, 3613 (1990).
- <sup>46</sup>D. C. Hamilton *et al.*, Rev. Sci. Instrum. **61**, 3104 (1990).
- <sup>47</sup>E. Mobius *et al.*, Rev. Sci. Instrum. **61**, 3609 (1990).
- <sup>48</sup>G. Gloeckler *et al.*, Astron. Astrophys. Suppl. **92**, 267 (1992).
- <sup>49</sup>D. Hovestadt *et al.*, Sol. Phys. **162**, 441 (1995).
- <sup>50</sup>R. A. Mapleton, *Theory of Charge Exchange* (Wiley, New York, 1972).
- <sup>51</sup>C. F. Barnett *et al.*, *Atomic Data for Fusion, Collisions of H, H<sub>2</sub>, He, and Li Atoms and Ions with Atoms and Molecules* (Oak Ridge National Laboratory, 1990), ORNL-6086/V1.
- <sup>52</sup>W. N. Spjeldvik and P. L. Rothwell, in *Handbook of Geophysics and the Space Environment*, edited by A. S. Jursa (Air Force Geophysics Laboratory, 1985), (5-1)–(5-55).
- <sup>53</sup>S.-I. Akasofu, *Physics of Magnetospheric Substorms* (Reidel, Dordrecht, 1977).
- <sup>54</sup>G. L. Siscoe, in *Solar System Plasma Physics, Vol. II, Magnetospheres*, edited by C. F. Kennel, L. J. Lanzerotti, and E. N. Parker (North-Holland, Amsterdam 1979), pp. 319–402.
- <sup>55</sup>*Solar System Plasma Physics, Vol. II, Magnetospheres*, edited by C. F. Kennel, L. J. Lanzerotti, and E. N. Parker (North-Holland, Amsterdam, 1979).
- <sup>56</sup>*Energetic Ion Composition in the Earth's Magnetosphere*, edited by R. G. Johnson (Kluwer, Boston, 1983).
- <sup>57</sup>L. R. Lyons and D. J. Williams, *Quantitative Aspects of Magnetospheric Physics*, (Kluwer, Boston, 1984).
- <sup>58</sup>*The Solar Wind and the Earth*, edited by S. I. Akasofu and Y. Kamide, (Kluwer, Dordrecht, Boston, 1987).
- <sup>59</sup>*Modeling of Magnetosphere Plasma Processes*, edited by R. Wilson (American Geophysical Union Washington, DC, 1991).
- <sup>60</sup>G. Paschmann, “The Magnetopause,” in *Geomagnetism*, edited by J. A. Jacobs (Academic, New York, 1991), Vol. 4, pp. 295–331.
- <sup>61</sup>M. Schulz, “The Magnetosphere,” in *Geomagnetism*, edited by J. A. Jacobs (Academic, New York, 1991), Vol. 4, pp. 87–293.
- <sup>62</sup>Y. Kamide and W. Baumjohann, *Magnetosphere-Ionosphere Coupling* (Springer, Berlin, 1993).
- <sup>63</sup>W. D. Gonzales *et al.*, J. Geophys. Res. **99**, 5771 (1994).
- <sup>64</sup>*Introduction to Space Physics*, edited by M. G. Kivelson and C. T. Russell (Cambridge University Press, Cambridge, 1995).
- <sup>65</sup>D. Stern, Rev. Geophys. **27**, 103 (1989).
- <sup>66</sup>D. Stern, Rev. Geophys. **34**, 1 (1996).
- <sup>67</sup>T. E. Moore and D. C. Delcourt, Rev. Geophys. **33**, 175 (1995).
- <sup>68</sup>*Radiation Belts: Models and Standards*, edited by J. F. Lemaire, D. Heynderickx, and D. N. Baker (American Geophysical Union, Washington, DC, 1996).
- <sup>69</sup>D. J. Williams, Space Sci. Rev. **42**, 375 (1985).
- <sup>70</sup>J. T. Gosling *et al.*, J. Geophys. Res. **96**, 7831 (1991).
- <sup>71</sup>B. T. Tsurutani *et al.*, Geophys. Res. Lett. **19**, 73 (1992).
- <sup>72</sup>E. Hildner, in *Eruptive Solar Flares*, edited by Z. Svestka, B. V. Jackson, and M. E. Machado (Springer, Berlin, 1992), pp. 227–233.
- <sup>73</sup>A. J. Hundhausen, J. Geophys. Res. **98**, 13177 (1993).
- <sup>74</sup>B. T. Tsurutani and W. D. Gonzalez, Phys. Fluids B **5**, 2623 (1993).
- <sup>75</sup>J. T. Gosling, Phys. Fluids B **5**, 2638 (1993).
- <sup>76</sup>J. T. Gosling, J. Geophys. Res. **98**, 18937 (1993).
- <sup>77</sup>A. J. Dessler and E. N. Parker, J. Geophys. Res. **64**, 2239 (1959).
- <sup>78</sup>A. J. Dessler *et al.*, J. Geophys. Res. **66**, 3631 (1961).
- <sup>79</sup>E. C. Roelof, Geophys. Res. Lett. **14**, 652 (1987).
- <sup>80</sup>N. F. Ness, in *Solar System Plasma Physics, Vol. II, Magnetospheres*, edited by C. F. Kennel, L. J. Lanzerotti, and E. N. Parker (North-Holland Amsterdam, 1979), pp. 183–206.
- <sup>81</sup>C. T. Russell, in *Solar System Plasma Physics, Vol. II, Magnetospheres*, edited by C. F. Kennel, L. J. Lanzerotti, and E. N. Parker (North-Holland, Amsterdam, 1979), pp. 207–252.
- <sup>82</sup>C. T. Russell *et al.*, in *Mercury*, edited by F. Vilas, C. R. Chapman, and M. S. Matthews (The University of Arizona Press, Tucson, AZ, 1988), pp. 514–561.
- <sup>83</sup>*Venus*, edited by D. M. Hunten, L. Colin, T. M. Donahue, and V. I. Moroz (The University of Arizona Press, Tucson, AZ, 1983).
- <sup>84</sup>J. G. Luhmann *et al.*, in *Mars*, edited by H. H. Kiefer, B. M. Jakosky, C. W. Snyder, and M. S. Matthews (The University of Arizona Press, Tucson, AZ, 1992), pp. 1090–1134.



- <sup>85</sup> *Jupiter*, edited by T. Gehrels (The University of Arizona Press, Tucson, AZ, 1976).
- <sup>86</sup> *Physics of the Jovian Magnetosphere*, edited by A. J. Dessler (Cambridge University Press, Cambridge, 1983).
- <sup>87</sup> *Saturn*, edited by T. Gehrels and M. S. Matthews (The University of Arizona Press, Tucson, AZ, 1984).
- <sup>88</sup> *Uranus*, edited by J. T. Bergstrahl, E. D. Miner, and M. S. Matthews (The University of Arizona Press, Tucson, AZ, 1991).
- <sup>89</sup> L. J. Lanzerotti, *Geophys. Res. Lett.* **19**, 1991 (1992).
- <sup>90</sup> B. T. Tsurutani *et al.*, *Geophys. Res. Lett.* **19**, 1993 (1992).
- <sup>91</sup> A. Meloni *et al.*, *Rev. Geophys. Space Phys.* **21**, 795 (1983).
- <sup>92</sup> C. W. Anderson, in *Solar System Plasma Physics*, Vol. III, edited by L. J. Lanzerotti, C. F. Kennel, and E. N. Parker (North Holland, Amsterdam, 1979), pp. 323–327.
- <sup>93</sup> D. J. Williams, in *Solar System Plasma Physics*, edited by L. J. Lanzerotti, C. F. Kennel, and E. N. Parker (North Holland, Amsterdam, 1979), Vol. III, pp. 327–330.
- <sup>94</sup> A. W. Peabody, in *Solar System Plasma Physics*, edited by L. J. Lanzerotti, C. F. Kennel, and E. N. Parker (North Holland, Amsterdam, 1979), Vol. III, pp. 349–352.
- <sup>95</sup> W. H. Campbell, in *Solar System Plasma Physics*, edited by L. J. Lanzerotti, C. F. Kennel, and E. N. Parker (North Holland, Amsterdam, 1979), Vol. III, pp. 352–356.
- <sup>96</sup> G. A. Paulikas, in *Solar System Plasma Physics*, edited by L. J. Lanzerotti, C. F. Kennel, and E. N. Parker (North Holland, Amsterdam, 1979), Vol. III, pp. 330–336.
- <sup>97</sup> M. A. Shea and D. F. Smart, *Eos Trans. AGU, Fall Meeting Suppl.* **76** (46), F431 (1995).
- <sup>98</sup> S. DeForest, in *Solar System Plasma Physics*, edited by L. J. Lanzerotti, C. F. Kennel, and E. N. Parker (North Holland, Amsterdam, 1979), Vol. III, pp. 336–339.
- <sup>99</sup> H. B. Garret, *Rev. Geophys. Space Phys.* **19**, 577 (1981).
- <sup>100</sup> D. J. Williams, in *Magnetospheric Physics*, edited by B. Hultqvist and C.-G. Falthammer (Plenum, New York, 1990), pp. 83–101.
- <sup>101</sup> D. Stern, *Eos Trans. AGU* **77**, 165 (1996).
- <sup>102</sup> R. L. Rairden *et al.*, *Geophys. Res. Lett.* **10**, 533 (1983).
- <sup>103</sup> R. L. Rairden *et al.*, *J. Geophys. Res.* **91**, 13613 (1986).
- <sup>104</sup> G. E. Thomas and R. C. Bohlin, *J. Geophys. Res.* **77**, 2752 (1972).
- <sup>105</sup> D. E. Shemansky and D. T. Hall, *J. Geophys. Res.* **96**, 4143 (1992).
- <sup>106</sup> A. T. Lui *et al.*, *Geophys. Res. Lett.* **23**, 2641 (1996).
- <sup>107</sup> E. C. Roelof *et al.*, *J. Geophys. Res.* **90**, 10991 (1985).
- <sup>108</sup> A. F. Cheng, *J. Geophys. Res.* **91**, 4524 (1986).
- <sup>109</sup> K. C. Hsieh and C. C. Curtis, *Geophys. Res. Lett.* **15**, 772 (1988).
- <sup>110</sup> A. F. Cheng and S. M. Krimigis, in *Solar System Plasma Physics*, edited by J. H. Waite Jr., J. L. Burch, and R. L. Moore (AGU, Washington, DC, 1989), pp. 253–260.
- <sup>111</sup> A. F. Cheng *et al.*, *Remote Sens. Rev.* **8**, 101 (1993).
- <sup>112</sup> B. R. Sandel *et al.*, *Remote Sens. Rev.* **8**, 147 (1993).
- <sup>113</sup> M. Hesse *et al.*, *Opt. Eng.* **32**, 3153 (1993).
- <sup>114</sup> K. R. Moore *et al.*, *Instrumentation for Magnetospheric Imagery*, Proc. SPIE 1744 edited by S. Chakrabarti (SPIE, Bellingham, WA, 1992), pp. 51–61.
- <sup>115</sup> K. R. Moore *et al.*, *Opt. Eng.* **33**, 342 (1994).
- <sup>116</sup> C. J. Chase and E. C. Roelof, *Johns Hopkins APL Tech. Dig.* **16**, 111 (1995).
- <sup>117</sup> S. Barabash *et al.*, *Adv. Space Res.* **16** (4), 81 (1995).
- <sup>118</sup> C. J. Chase and E. C. Roelof, *Adv. Space Res.* **18** (1997).
- <sup>119</sup> W. Bernstein *et al.*, *J. Geophys. Res.* **74**, 3601 (1969).
- <sup>120</sup> B. A. Tinsley, *J. Atmosph. Terr. Phys.* **43**, 617 (1981).
- <sup>121</sup> S. Orsini *et al.*, *J. Geophys. Res.* **99**, 13489 (1994).
- <sup>122</sup> I. A. Daglis and S. Livi, *Ann. Geophys. (Germany)* **13**, 505 (1995).
- <sup>123</sup> P. De Michelis and S. Orsini, *J. Geophys. Res.* **102**, 185 (1997).
- <sup>124</sup> J. Moritz, *Z. Geophys.* **38**, 701 (1972).
- <sup>125</sup> H. D. Voss *et al.*, *Opt. Eng.* **32**, 3083 (1993).
- <sup>126</sup> S. Noel and G. W. Pross, *J. Geophys. Res.* **98**, 17317 (1993).
- <sup>127</sup> L. Davis Jr., *Phys. Rev.* **100**, 1440 (1955).
- <sup>128</sup> E. N. Parker, *Astrophys. J.* **134**, 20 (1961).
- <sup>129</sup> A. J. Dessler, *Rev. Geophys. Space Phys.* **5**, 1 (1967).
- <sup>130</sup> W. I. Axford, in *Solar Wind*, NASA SP-308 (NASA, 1973), pp. 609–660.
- <sup>131</sup> W. I. Axford, in *Physics of the Outer Heliosphere*, edited by S. Grzedzielski and D. E. Page (Pergamon, New York, 1990), pp. 7–15.
- <sup>132</sup> A. J. Hundhausen, *Coronal Expansion and Solar Wind* (Springer, Berlin, 1972).
- <sup>133</sup> A. J. Hundhausen, in *Introduction to Space Physics*, edited by M. G. Kivelson and C. T. Russell (Cambridge University Press, Cambridge, 1995), pp. 91–128.
- <sup>134</sup> P. A. Isenberg, in *Geomagnetism*, edited by J. A. Jacobs (Academic, New York, 1991), Vol. 4, pp. 1–85.
- <sup>135</sup> J. L. Phillips *et al.*, *Science* **268**, 1030 (1995).
- <sup>136</sup> A. J. Lazarus and R. L. McNutt, Jr., in *Physics of the Outer Heliosphere*, edited by S. Grzedzielski and D. E. Page (Pergamon, Oxford, 1990), pp. 229–234.
- <sup>137</sup> S. T. Suess, *J. Geophys. Res.* **98**, 15147 (1993).
- <sup>138</sup> D. P. Cox and R. J. Reynolds, *Ann. Rev. Astron. Astrophys.* **25**, 303, (1987).
- <sup>139</sup> P. C. Frisch, in *Physics of the Outer Heliosphere*, edited by S. Grzedzielski and D. E. Page (Pergamon, New York, 1990), pp. 19–28.
- <sup>140</sup> P. C. Frisch, *Space Sci. Rev.* **72**, 499 (1995).
- <sup>141</sup> H. J. Fahr, *Space Sci. Rev.* **15**, 483 (1974).
- <sup>142</sup> T. E. Holzer, *Rev. Geophys. Space Phys.* **15**, 467 (1977).
- <sup>143</sup> G. E. Thomas, *Ann. Rev. Earth Planet. Sci.* **6**, 173 (1978).
- <sup>144</sup> J.-L. Bertaux, *IAU Colloq. No. 81*, NASA CP 2345, 1984, pp. 3–23.
- <sup>145</sup> S. T. Suess, *Rev. Geophys.* **28**, 97 (1990).
- <sup>146</sup> V. B. Baranov, *Space Sci. Rev.* **52**, 89 (1990).
- <sup>147</sup> H. J. Fahr and H. Fichtner, *Space Sci. Rev.* **58**, 193 (1991).
- <sup>148</sup> V. B. Baranov *et al.*, *Sov. Phys. Dokl.* **15**, 791 (1971).
- <sup>149</sup> V. B. Baranov and Yu. G. Malama, *J. Geophys. Res.* **98**, 15157 (1993).
- <sup>150</sup> V. B. Baranov and Yu. G. Malama, *J. Geophys. Res.* **100**, 14755 (1995).
- <sup>151</sup> R. Lallemand *et al.*, *Science* **260**, 1095 (1993).
- <sup>152</sup> P. Bertin *et al.*, *J. Geophys. Res.* **98**, 15193 (1993).
- <sup>153</sup> M. Witte *et al.*, *Adv. Space Res.* **13**, 121 (1993).
- <sup>154</sup> M. Witte *et al.*, *Space Sci. Rev.* **78**, 289 (1996).
- <sup>155</sup> J. Geiss and M. Witte, *Space Sci. Rev.* **78**, 229 (1996).
- <sup>156</sup> P. Frisch and J. D. Slavin, *Space Sci. Rev.* **78**, 223 (1996).
- <sup>157</sup> J. Luhmann, *J. Geophys. Res.* **75**, 13285 (1994).
- <sup>158</sup> H. J. Fahr, *Astrophys. Space Sci.* **2**, 474 (1968).
- <sup>159</sup> R. R. Meier, *Astron. Astrophys.* **55**, 211 (1977).
- <sup>160</sup> F. M. Wu and D. L. Judge, *Astrophys. J.* **231**, 594 (1979).
- <sup>161</sup> J. M. Ajello *et al.*, *Astrophys. J.* **317**, 964 (1987).
- <sup>162</sup> D. T. Hall *et al.*, *J. Geophys. Res.* **98**, 15185 (1993).
- <sup>163</sup> E. Mobius *et al.*, *Nature (London)* **318**, 426 (1985).
- <sup>164</sup> E. Mobius, in *Physics of the Outer Heliosphere*, edited by S. Grzedzielski and D. E. Page (Pergamon, Oxford, 1990), pp. 345–354.
- <sup>165</sup> G. Gloeckler *et al.*, *Science* **261**, 70 (1993).
- <sup>166</sup> J. Geiss *et al.*, *Astron. Astrophys.* **282**, 924 (1994).
- <sup>167</sup> T. F. Adams and P. C. Frisch, *Astrophys. J.* **212**, 300 (1977).
- <sup>168</sup> J. T. Clarke *et al.*, *Astron. Astrophys.* **139**, 389 (1984).
- <sup>169</sup> H. J. Fahr, *Astron. Astrophys.* **241**, 251 (1991).
- <sup>170</sup> V. Izmodenov *et al.*, *Astron. Astrophys.* **317**, 193 (1997).
- <sup>171</sup> P. M. Banks, *J. Geophys. Res.* **76**, 4341 (1971).
- <sup>172</sup> H. J. Fahr *et al.*, *Astron. Astrophys.* **102**, 359 (1980).
- <sup>173</sup> M. A. Gruntman, *J. Geophys. Res.* **101**, 15555 (1996).
- <sup>174</sup> H. Rosenbauer and H. J. Fahr, “Direct measurement of the fluid parameters of the nearby interstellar gas using helium as a tracer. Experimental proposal for the Out-of-Ecliptic Mission, Internal Report” (Max-Planck-Institut für Aeronomie, Katlenburg-Lindau, Germany, 1977).
- <sup>175</sup> H. Rosenbauer *et al.*, *ESA SP-1050*, 123 (1984).
- <sup>176</sup> M. Witte *et al.*, *Astron. Astrophys. Suppl. Ser.* **92**, 333 (1992).
- <sup>177</sup> M. A. Gruntman and V. B. Leonas, “Neutral solar wind: possibilities of experimental investigation,” Report (Preprint) 825 (Space Research Institute (IKI), Academy of Sciences, Moscow, 1983).
- <sup>178</sup> H. J. Fahr, *Astrophys. Space Sci.* **2**, 496 (1968).
- <sup>179</sup> K. C. Hsieh *et al.*, *Instrumentation for Magnetospheric Imagery*, Proc. SPIE 1744, edited by S. Chakrabarti (SPIE, Bellingham, 1992), pp. 72–78.
- <sup>180</sup> M. A. Gruntman, *Sov. Astron. Lett.* **8**, 24 (1982).
- <sup>181</sup> J. H. Moore Jr. and C. B. Opal, *Space Sci. Instrum.* **1**, 377 (1975).
- <sup>182</sup> M. A. Gruntman *et al.*, in *Physics of the Outer Heliosphere*, edited by S. Grzedzielski and D. E. Page (Pergamon, New York, 1990), pp. 355–358.
- <sup>183</sup> S. Bleszynski *et al.*, *Planet. Space Sci.* **40**, 1525 (1992).
- <sup>184</sup> W. I. Axford *et al.*, *Astrophys. J.* **137**, 1268 (1963).
- <sup>185</sup> T. N. L. Patterson *et al.*, *Planet. Space Sci.* **11**, 767 (1963).
- <sup>186</sup> A. J. Hundhausen, *Planet. Space Sci.* **16**, 783 (1968).
- <sup>187</sup> P. Blum and H. J. Fahr, *Astron. Astrophys.* **4**, 280 (1970).
- <sup>188</sup> T. E. Holzer, *J. Geophys. Res.* **77**, 5407 (1972).
- <sup>189</sup> L. A. Fisk *et al.*, *Astrophys. J.* **190**, L35 (1974).
- <sup>190</sup> M. A. Lee, in *Physics of the Outer Heliosphere*, edited by S. Grzedzielski

- and D. E. Page (Pergamon, Oxford, 1990), pp. 157–168.
- <sup>191</sup> J. R. Jokipii and J. Giacalone, *Space Sci. Rev.* **78**, 137 (1996).
  - <sup>192</sup> A. Czechowski *et al.*, *Astron. Astrophys.* **297**, 892 (1995).
  - <sup>193</sup> K. C. Hsieh *et al.*, *Eos Trans. AGU, Spring Meet. Suppl.* **78** (17), S260 (1997).
  - <sup>194</sup> J. W. Chamberlain, *Physics of the Aurora and Airglow* (Academic, New York, 1961).
  - <sup>195</sup> W. I. Axford, *J. Geophys. Res.* **99**, 19199 (1994).
  - <sup>196</sup> N. Fukushima, *J. Geophys. Res.* **99**, 19133 (1994).
  - <sup>197</sup> C. T. Russell, in *Introduction to Space Physics*, edited by M. G. Kivelson and C. T. Russell (Cambridge University Press, Cambridge, 1995), pp. 1–26.
  - <sup>198</sup> *Discovery of the Magnetosphere*, edited by C. S. Gillmor and J. R. Spreiter (American Geophysical Union, Washington, DC, 1997).
  - <sup>199</sup> A. B. Meinel, *Phys. Rev.* **80**, 1096 (1950).
  - <sup>200</sup> A. B. Meinel, *Astrophys. J.* **113**, 50 (1951).
  - <sup>201</sup> C. Y. Fan, *Astrophys. J.* **128**, 420 (1958).
  - <sup>202</sup> L. Vegard, *Nature* (London) **144**, 1089 (1939).
  - <sup>203</sup> G. W. Stuart, *Phys. Rev. Lett.* **2**, 417 (1959).
  - <sup>204</sup> D. C. Morton and J. D. Purcell, *Planet. Space Sci.* **9**, 455 (1962).
  - <sup>205</sup> B. A. Tinsley, *Rev. Geophys. Space Phys.* **9**, 89 (1971).
  - <sup>206</sup> F. S. Johnson and R. A. Fish, *Astrophys. J.* **131**, 502 (1960).
  - <sup>207</sup> S.-I. Akasofu, *Planet. Space Sci.* **12**, 801 (1964).
  - <sup>208</sup> S.-I. Akasofu, *Planet. Space Sci.* **12**, 905 (1964).
  - <sup>209</sup> J. C. Brandt and D. M. Hunten, *Planet. Space Sci.* **14**, 95 (1966).
  - <sup>210</sup> P. A. Cloutier, *Planet. Space Sci.* **14**, 809 (1966).
  - <sup>211</sup> R. L. Wax and W. Bernstein, *Rev. Sci. Instrum.* **38**, 1612 (1967).
  - <sup>212</sup> W. Bernstein *et al.*, in *Small Rocket Instrumentation Techniques* (North-Holland, Amsterdam, 1969), pp. 224–231.
  - <sup>213</sup> W. Bernstein *et al.*, *Nucl. Instrum. Methods* **90**, 325 (1970).
  - <sup>214</sup> R. L. Wax *et al.*, *J. Geophys. Res.* **75**, 6390 (1970).
  - <sup>215</sup> M. R. Ainsbund *et al.*, *Cosmic Res.* (English transl. of *Kosmicheskoe Issledovaniya*) (Plenum, New York, 1973), Vol. 11, pp. 661–665.
  - <sup>216</sup> H. O. Funsten *et al.*, *J. Spacecr. Rockets* **32**, 899 (1995).
  - <sup>217</sup> M. A. Gruntman and V. A. Morozov, *J. Phys. E* **15**, 1356 (1982).
  - <sup>218</sup> M. A. Gruntman, “Interstellar helium at the Earth’s orbit,” Report (Preprint) 543 (Space Research Institute (IKI), Academy of Sciences, Moscow, 1980).
  - <sup>219</sup> S. Grzedzielski, *Artificial Satellites*, **18**, 5 (1983).
  - <sup>220</sup> S. Grzedzielski, *Artificial Satellites*, **19**, 5 (1984).
  - <sup>221</sup> S. Grzedzielski and D. Rucinski, in *Physics of the Outer Heliosphere*, edited by S. Grzedzielski and D. E. Page (Pergamon, New York, 1990), pp. 367–370.
  - <sup>222</sup> K. C. Hsieh *et al.*, “HELENA—A proposal to perform *in situ* investigation of NEUTRALS in geospace and the heliosphere on PPL&IPL of the OPEN mission,” Proposal to NASA, 1980.
  - <sup>223</sup> K.-P. Wenzel and D. Eaton, *European Space Agency (ESA) Bull.* **63**, 10 (1990).
  - <sup>224</sup> M. Banaszekiewicz and S. Grzedzielski, *Ann. Geophys. (Germany)* **10**, 527 (1992).
  - <sup>225</sup> M. A. Gruntman, *EUV, X-Ray, and Gamma-Ray Instrumentation for Astronomy*, Proc. SPIE 1549, edited by O. H. W. Siegmund and R. E. Rothschild (SPIE, Bellingham, 1991), pp. 385–394.
  - <sup>226</sup> M. L. Schattenburg *et al.*, *Phys. Scr.* **41**, 13 (1990).
  - <sup>227</sup> J. M. Carter *et al.*, *J. Vac. Sci. Technol. B* **10**, 2909 (1992).
  - <sup>228</sup> E. E. Scime *et al.*, *Appl. Opt.* **34**, 648 (1995).
  - <sup>229</sup> M. A. Gruntman, *X-Ray and Extreme Ultraviolet Optics*, Proc. SPIE 2515, edited by R. B. Hoover and A. B. C. Walker, Jr. (SPIE, Bellingham, 1995), pp. 231–239.
  - <sup>230</sup> M. A. Gruntman, *Appl. Opt.* **34**, 5732 (1995).
  - <sup>231</sup> M. A. Gruntman, *Appl. Opt.* **36**, 2203 (1997).
  - <sup>232</sup> W. J. Heikkilä, *J. Geophys. Res.* **76**, 1076 (1971).
  - <sup>233</sup> D. Hovestadt *et al.*, *Phys. Rev. Lett.* **28**, 1340 (1972).
  - <sup>234</sup> P. F. Mizera and J. B. Blake, *J. Geophys. Res.* **78**, 1058 (1973).
  - <sup>235</sup> D. Hovestadt and M. Scholer, *J. Geophys. Res.* **81**, 5039 (1976).
  - <sup>236</sup> S. M. Krimigis *et al.*, *Geophys. Res. Lett.* **2**, 457 (1975).
  - <sup>237</sup> E. Kirsch *et al.*, *Geophys. Res. Lett.* **8**, 169 (1981).
  - <sup>238</sup> E. Kirsch *et al.*, *Nature* (London) **292**, 718 (1981).
  - <sup>239</sup> S. M. Krimigis *et al.*, *Space Sci. Rev.* **21**, 329 (1977).
  - <sup>240</sup> D. J. Williams *et al.*, *IEEE Trans. Geosci. Electron.* **GE-16**, 270 (1978).
  - <sup>241</sup> E. C. Roelof and D. G. Mitchell, *Eos Trans. AGU* **63**, 403 (1982).
  - <sup>242</sup> E. C. Roelof and D. G. Mitchell, *Eos Trans. AGU* **63**, 1078 (1982).
  - <sup>243</sup> C. C. Curtis and K. C. Hsieh, in *Solar System Plasma Physics*, edited by J. H. Waite Jr., J. L. Burch, and R. L. Moore, (AGU, Washington, DC, 1989), pp. 247–251.
  - <sup>244</sup> M. G. Henderson *et al.*, *Geophys. Res. Lett.* **24**, 1167 (1997).
  - <sup>245</sup> J. B. Blake *et al.*, *Space Sci. Rev.* **71**, 531 (1995).
  - <sup>246</sup> E. C. Roelof *et al.*, *Instrumentation for Magnetospheric Imagery*, Proc. SPIE 1744, edited by S. Chakrabarti, (SPIE, Bellingham, 1992), pp. 19–30.
  - <sup>247</sup> E. C. Roelof *et al.*, *Instrumentation for Magnetospheric Imagery II*, Proc. SPIE 2008, edited by S. Chakrabarti (SPIE, Bellingham, 1993), pp. 202–213.
  - <sup>248</sup> K. C. Hsieh *et al.*, in *Solar Wind Seven*, edited by E. Marsch and R. Schwenn (Pergamon, New York, 1992), pp. 357–364.
  - <sup>249</sup> M. A. Gruntman and V. B. Leonas, “Experimental opportunity of planetary magnetosphere imaging in energetic neutral particles,” Report (Preprint) 1181 (Space Research Institute (IKI), Academy of Sciences, Moscow, 1986) (also published in Proceedings, International Workshop on Problems of Physics of Neutral Particles in the Solar System, Zakopane, 1985, pp. 151–179).
  - <sup>250</sup> R. W. McEntire and D. G. Mitchell, in *Solar System Plasma Physics*, edited by J. H. Waite Jr., J. L. Burch, and R. L. Moore, (AGU, Washington, DC, 1989), pp. 69–80.
  - <sup>251</sup> K. C. Hsieh and C. C. Curtis, in *Solar System Plasma Physics*, edited by J. H. Waite, Jr., J. L. Burch, and R. L. Moore (AGU, Washington, DC, 1989), pp. 159–164.
  - <sup>252</sup> E. P. Keath *et al.*, in *Solar System Plasma Physics*, edited by J. H. Waite, Jr., J. L. Burch, and R. L. Moore (AGU, Washington, DC, 1989), pp. 165–170.
  - <sup>253</sup> M. A. Gruntman *et al.*, *JETP Lett.* **51**, 22 (1990).
  - <sup>254</sup> D. J. McComas *et al.*, *Instrumentation for Magnetospheric Imagery*, Proc. SPIE 1744, edited by S. Chakrabarti, (SPIE, Bellingham, 1992), pp. 40–50.
  - <sup>255</sup> H. O. Funsten *et al.*, *Opt. Eng.* **32**, 3090 (1993).
  - <sup>256</sup> H. O. Funsten *et al.*, *Opt. Eng.* **33**, 349 (1994).
  - <sup>257</sup> A. G. Ghielmetti *et al.*, *Opt. Eng.* **33**, 362 (1994).
  - <sup>258</sup> P. Wurz *et al.*, *Opt. Eng.* **34**, 2365 (1995).
  - <sup>259</sup> A. Amsif *et al.*, *J. Geophys. Res.* **102** (in press, 1997).
  - <sup>260</sup> J. M. Young and J. C. Holmes, *Science* **171**, 379 (1971).
  - <sup>261</sup> D. W. Swift *et al.*, *Planet. Space Sci.* **37**, 379 (1989).
  - <sup>262</sup> D. L. Murphy and Y. T. Chiu, *Opt. Eng.* **32**, 3147 (1993).
  - <sup>263</sup> D. E. Garrido *et al.*, *Opt. Eng.* **33**, 371 (1994).
  - <sup>264</sup> R. L. Meier and J. M. Picone, *J. Geophys. Res.* **99**, 6307 (1994).
  - <sup>265</sup> L. A. Frank and J. D. Cravens, *Rev. Geophys.* **26**, 249 (1988).
  - <sup>266</sup> W. L. Imhof *et al.*, *Opt. Eng.* **33**, 383 (1994).
  - <sup>267</sup> D. L. McKenzie *et al.*, *Opt. Eng.* **33**, 414 (1994).
  - <sup>268</sup> W. Calvert *et al.*, *Radio Sci.* **30**, 1577 (1995).
  - <sup>269</sup> R. A. Greenwald, *Radio Sci.* **32**, 277 (1997).
  - <sup>270</sup> W. Calvert *et al.*, *Radio Sci.* **32**, 281 (1997).
  - <sup>271</sup> R. A. Greenwald, *Radio Sci.* **32**, 877 (1997).
  - <sup>272</sup> S. Chakrabarti *et al.*, *J. Geophys. Res.* **88**, 4898 (1983).
  - <sup>273</sup> S. Chakrabarti *et al.*, *J. Geophys. Res.* **89**, 5660 (1984).
  - <sup>274</sup> G. Boella *et al.*, *IEEE Trans. Nucl. Sci.* **NS-33**, 755 (1986).
  - <sup>275</sup> J. E. Grindlay *et al.*, *IEEE Trans. Nucl. Sci.* **NS-33**, 750 (1986).
  - <sup>276</sup> K. C. Hsieh *et al.*, Proposal to Planetary Instrument Definition and Development Program, NASA, 1985.
  - <sup>277</sup> C. C. Curtis *et al.*, *Instrumentation for Magnetospheric Imagery*, SPIE Proj. 1744, edited by S. Chakrabarti, (SPIE, Bellingham, 1992), pp. 138–147.
  - <sup>278</sup> C. C. Curtis, *Instrumentation for Magnetospheric Imagery*, SPIE Proc. 1744, edited by S. Chakrabarti (SPIE, Bellingham, 1992), pp. 161–170.
  - <sup>279</sup> R. H. Dicke, *Astrophys. J. Lett.* **153**, L101 (1968).
  - <sup>280</sup> J. G. Ables, *Proc. Astron. Soc. Aust.* **1**, 172 (1968).
  - <sup>281</sup> R. L. Blake *et al.*, *Rev. Sci. Instrum.* **45**, 513 (1974).
  - <sup>282</sup> J. Gunson and B. Polychronopoulos, *Mon. Not. R. Astron. Soc.* **177**, 485 (1976).
  - <sup>283</sup> E. E. Fenimore and T. M. Cannon, *Appl. Opt.* **17**, 337 (1978).
  - <sup>284</sup> T. M. Cannon and E. E. Fenimore, *Appl. Opt.* **18**, 1052 (1979).
  - <sup>285</sup> E. E. Fenimore *et al.*, *Appl. Opt.* **18**, 945 (1979).
  - <sup>286</sup> K. A. Nugent, *Appl. Opt.* **26**, 563 (1987).
  - <sup>287</sup> E. Caroli *et al.*, *Space Sci. Rev.* **45**, 349 (1987).
  - <sup>288</sup> D. Ress *et al.*, *Rev. Sci. Instrum.* **63**, 5086 (1992).
  - <sup>289</sup> E. E. Fenimore, *Appl. Opt.* **17**, 3562 (1978).
  - <sup>290</sup> S. W. Golomb, *Digital Communications with Space Applications* (Prentice Hall Englewood Cliffs, NJ, 1964).
  - <sup>291</sup> F. J. MacWilliams and N. J. A. Sloane, *Proc. IEEE* **64**, 1715 (1976).

- 292 K. Skold, Nucl. Instrum. Methods **63**, 114 (1968).
- 293 G. Comsa *et al.*, Rev. Sci. Instrum. **52**, 789 (1981).
- 294 R. David *et al.*, Rev. Sci. Instrum. **57**, 2771 (1986).
- 295 M. A. Gruntman, *Instrumentation for Magnetospheric Imagery II*, Proc. SPIE 2008, edited by S. Chakrabarti (SPIE, Bellingham, 1993), pp. 58–72.
- 296 M. H. Tai *et al.*, Appl. Opt. **14**, 2678 (1975).
- 297 P. Zeppenfeld *et al.*, Rev. Sci. Instrum. **64**, 1520 (1993).
- 298 V. V. Afrosimov *et al.*, Sov. Phys. Tech. Phys. **5**, 1378 (1961).
- 299 H. P. Eubank, in *Diagnostics for Fusion Experiments*, edited by E. Sindoni and C. Wharton (Pergamon, New York, 1979), pp. 17–34.
- 300 J. E. Osher, in *Diagnostics for Fusion Experiments*, edited by E. Sindoni and C. Wharton (Pergamon, New York, 1979), pp. 47–77.
- 301 V. V. Afrosimov *et al.*, Sov. Phys. Tech. Phys. **20**, 33 (1975).
- 302 C. J. Armentrout *et al.*, Rev. Sci. Instrum. **56**, 2101 (1985).
- 303 D. E. Voss and S. A. Cohen, Rev. Sci. Instrum. **53**, 1696 (1982).
- 304 J. M. McChesney *et al.*, Rev. Sci. Instrum. **66**, 348 (1995).
- 305 P. E. Stott, Rev. Sci. Instrum. **63**, 4696 (1992).
- 306 G. Bracco *et al.*, Rev. Sci. Instrum. **63**, 5685 (1992).
- 307 H. Verbeek, J. Phys. E **19**, 964 (1986).
- 308 K. Hayashi *et al.*, Rev. Sci. Instrum. **56**, 359 (1985).
- 309 Y. Kusama *et al.*, Rev. Sci. Instrum. **66**, 339 (1995).
- 310 S. Costa *et al.*, Rev. Sci. Instrum. **66**, 330 (1995).
- 311 E. Scime and S. Hokin, Rev. Sci. Instrum. **63**, 4527 (1992).
- 312 W. Van Toledo *et al.*, Rev. Sci. Instrum. **61**, 622 (1990).
- 313 W. Van Toledo *et al.*, Rev. Sci. Instrum. **63**, 2223 (1992).
- 314 H. Verbeek *et al.*, J. Phys. E **10**, 944 (1977).
- 315 H. H. Fleischmann and R. Kribel, Rev. Sci. Instrum. **39**, 233 (1968).
- 316 J. S. Vickers *et al.*, Opt. Eng. **32**, 3126 (1993).
- 317 M. D. Daybell *et al.*, Opt. Eng. **33**, 445 (1994).
- 318 D. L. Judge *et al.*, Nucl. Instrum. Methods Phys. Res. A **347**, 472 (1994).
- 319 C. C. Curtis and K. C. Hsieh, Rev. Sci. Instrum. **59**, 2424 (1988).
- 320 E. E. Scime *et al.*, Rev. Sci. Instrum. **66**, 336 (1995).
- 321 D. J. McComas *et al.*, Opt. Eng. **33**, 335 (1994).
- 322 M. A. Gruntman, Instrum. Exp. Techn. **26**, 943 (1983).
- 323 W. A. de Zeeuw *et al.*, Rev. Sci. Instrum. **62**, 110 (1991).
- 324 E. Rutherford, J. Chadwick, and C. D. Ellis, *Radiation from Radioactive Substances* (MacMillan Company, New York, 1930), p. 548.
- 325 F. S. Goulding and D. A. Landis, in *Nuclear Spectroscopy and Reactions, Part A*, edited by J. Cerny (Academic, New York, 1974), pp. 413–481.
- 326 W. F. Schneider *et al.*, Nucl. Instrum. Methods **87**, 253 (1970).
- 327 H. Pleyer *et al.*, Nucl. Instrum. Methods **96**, 263 (1971).
- 328 G. Gabor *et al.*, Nucl. Instrum. Methods **130**, 65 (1975).
- 329 C. C. Curtis and K. C. Hsieh, Rev. Sci. Instrum. **57**, 989 (1986).
- 330 E. Keppler *et al.*, Nature (London) **321**, 273 (1986).
- 331 C. C. Curtis *et al.*, Astron. Astrophys. **187**, 360 (1987).
- 332 T. Zurbuchen *et al.*, Opt. Eng. **34**, 1303 (1995).
- 333 C. Leinert and D. Kluppelberg, Appl. Opt. **13**, 556 (1974).
- 334 M. A. Gruntman, Rev. Sci. Instrum. **65**, 758 (1994).
- 335 G. Bertolini and A. Coche, *Semiconductor Detectors* (Wiley, New York, 1968).
- 336 G. F. Knoll, *Radiation Detection and Measurement* (Wiley, New York, 1979, 1989).
- 337 F. S. Goulding and R. H. Pehl, in *Nuclear Spectroscopy and Reactions, Part A*, edited by J. Cerny (Academic, New York, 1974), pp. 289–343.
- 338 F. M. Ipavich *et al.*, Nucl. Instrum. Methods **154**, 291 (1978).
- 339 H. D. Voss, IEEE Trans. Nucl. Sci. **NS-29**, 178 (1982).
- 340 W. E. Baumgartner and W. K. Huber, J. Phys. E **76**, 321 (1976).
- 341 F. Paresce, Appl. Opt. **14**, 2823 (1975).
- 342 M. C. Johnson, Rev. Sci. Instrum. **40**, 311 (1969).
- 343 G. A. Goodrich and W. C. Wiley, Rev. Sci. Instrum. **33**, 761 (1962).
- 344 D. S. Evans, Rev. Sci. Instrum. **36**, 375 (1965).
- 345 E. A. Kurz, Am. Laboratory **11**, 67 (1979).
- 346 B. W. Manley *et al.*, Adv. Electron. Electron Phys. **28A**, 471 (1969).
- 347 D. Washington *et al.*, Acta Electron. **14**, 201 (1971).
- 348 B. Lescovar, Phys. Today **30**, 42 (1977).
- 349 A. R. Asam, Opt. Eng. **17**, 640 (1978).
- 350 J. L. Wiza, Nucl. Instrum. Methods **62**, 587 (1979).
- 351 G. W. Fraser, *X-Ray Detectors in Astronomy* (Cambridge University Press, Cambridge, 1989).
- 352 J. Adams and B. W. Manley, Philips Tech. Rev. **28**, 156 (1967).
- 353 J. G. Timothy, Rev. Sci. Instrum. **52**, 1131 (1981).
- 354 W. M. Sackinger and J. M. Johnson, Adv. Electron. Electron Phys. **28A**, 487 (1969).
- 355 G. Beck, Rev. Sci. Instrum. **47**, 849 (1976).
- 356 P. Wurz and L. Gubler, Rev. Sci. Instrum. **65**, 871 (1994).
- 357 P. Wurz and L. Gubler, Rev. Sci. Instrum. **67**, 1790 (1996).
- 358 M. Lampton, Proc. Intern. Astron. Union Colloq. 40, Meudon Observatory, France, 32/1–32/28, 1977.
- 359 R. W. Wijnaendts van Resandt and J. Los, *Proceedings of the XI International Conference on Physics Electronic and Atomic Collisions (IC-PEAC)* (North-Holland, Amsterdam, 1981), pp. 831–841.
- 360 J. G. Timothy, Publ. Astron. Soc. Pac. **95**, 810 (1983).
- 361 M. A. Gruntman, Instrum. Exp. Tech. **27**, 1 (1984).
- 362 O. H. W. Siegmund *et al.*, ESA Symposium on Photon Detectors for Space Instrumentation, 1982, ESA SP-356, pp. 89–96.
- 363 M. Lampton and F. Paresce, Rev. Sci. Instrum. **45**, 1098 (1974).
- 364 M. Lampton and C. Carlson, Rev. Sci. Instrum. **50**, 1093 (1979).
- 365 C. Martin *et al.*, Rev. Sci. Instrum. **52**, 1067 (1981).
- 366 W. Parkes *et al.*, Nucl. Instrum. Methods **121**, 151 (1974).
- 367 R. W. Wijnaendts van Resandt *et al.*, Chem. Phys. **26**, 223 (1977).
- 368 F. Busch *et al.*, Nucl. Instrum. Methods **171**, 71 (1980).
- 369 G. Charpak *et al.*, Nucl. Instrum. Methods **65**, 217 (1968).
- 370 B. P. Duval *et al.*, Rev. Sci. Instrum. **57**, 2156 (1986).
- 371 S. E. Sobottka and M. B. Williams, IEEE Trans. Nucl. Sci. **NS-35**, 348 (1988).
- 372 M. Lampton *et al.*, Rev. Sci. Instrum. **58**, 2298 (1987).
- 373 M. Lampton *et al.*, IEEE Trans. Nucl. Sci. **NS-37**, 1548 (1990).
- 374 R. Raffanti and M. Lampton, Rev. Sci. Instrum. **64**, 1506 (1993).
- 375 O. H. W. Siegmund *et al.*, *EUV, X-Ray, and Gamma-Ray Instrumentation for Astronomy IV*, Proceedings SPIE 2006, edited by O. H. W. Siegmund (SPIE, Bellingham, 1993), pp. 176–187.
- 376 P. G. Friedman *et al.*, Rev. Sci. Instrum. **67**, 596 (1996).
- 377 F. R. Powell *et al.*, Opt. Eng. **29**, 614 (1990).
- 378 H. Bradner, Rev. Sci. Instrum. **19**, 662 (1948).
- 379 F. E. Carpenter and J. A. Curcio, Rev. Sci. Instrum. **21**, 675 (1950).
- 380 S. Bashkin and G. Goldhaber, Rev. Sci. Instrum. **22**, 112 (1951).
- 381 G. A. Sawyer, Rev. Sci. Instrum. **23**, 604 (1952).
- 382 G. Dearnaley, Rev. Sci. Instrum. **31**, 197 (1960).
- 383 P. Vouros *et al.*, Rev. Sci. Instrum. **39**, 741 (1968).
- 384 G. Both *et al.*, Rev. Sci. Instrum. **58**, 424 (1987).
- 385 J. O. Stoner, Jr. and S. Bashkin, Appl. Opt. **17**, 321 (1978).
- 386 J. O. Stoner, J. Appl. Phys. **40**, 707 (1969).
- 387 A. H. F. Muggleton, Vacuum **37**, 785 (1987).
- 388 T. M. Ivkova *et al.*, Nucl. Instrum. Methods Phys. Res. A **362**, 77 (1995).
- 389 H. O. Funsten *et al.*, Rev. Sci. Instrum. **63**, 4741 (1992).
- 390 M. Rubel *et al.*, Nucl. Instrum. Methods Phys. Res. B **47**, 202 (1990).
- 391 P. Lorenzen *et al.*, Nucl. Instrum. Methods Phys. Res. A **282**, 213 (1989).
- 392 M. A. Gruntman, Rev. Sci. Instrum. **60**, 3188 (1989).
- 393 L. Kay and R. Shepherd, J. Phys. E **17**, 882 (1984).
- 394 H. H. Bukow *et al.*, Nucl. Instrum. Methods **182/183**, 383 (1981).
- 395 V. A. Kurnaev, Sov. Phys. Tech. Phys. **21**, 383 (1976).
- 396 T. Ngo *et al.*, Surf. Sci. **314**, L817 (1994).
- 397 E. Fermi and E. Teller, Phys. Rev. **72**, 399 (1947).
- 398 N. Bohr, Mat. Fys. Medd. K. Dan. Vidensk. Selsk. **18**, 8 (1948).
- 399 J. Lindhard and M. Scharff, Phys. Rev. **124**, 128 (1961).
- 400 J. D. Jackson, in “Classical Electrodynamics,” Chapter 13, *Collisions Between Charged Particles, Energy Loss, and Scattering* (Wiley, New York, 1962, 1975).
- 401 U. Fano, Annu. Rev. Nucl. Sci. **13**, 1 (1963).
- 402 P. Siegmund, Mat. Fys. Medd. K. Dan. Vidensk. Selsk. **40**, 1 (1978).
- 403 P. Siegmund, *The Stopping and Range of Ions in Matter* (Pergamon, New York, 1979), Vol. 1.
- 404 J. F. Ziegler, *The Stopping and Range of Ions in Matter* (Pergamon, New York, 1980), Vol. 5.
- 405 J. F. Ziegler *et al.*, *The Stopping and Range of Ions in Solids* (Pergamon, New York, 1985), Vol. 1.
- 406 S. H. Overbury *et al.*, Radiat. Eff. **41**, 219 (1979).
- 407 J. P. Biersack and L. G. Hagmark, Nucl. Instrum. Methods **174**, 257 (1980).
- 408 J. F. Ziegler, IBM Research, Yorktown, New York.
- 409 H. O. Funsten, Phys. Rev. B **52**, R8703 (1995).
- 410 A. Burgi *et al.*, J. Appl. Phys. **68**, 2547 (1990).
- 411 R. Kallenbach *et al.*, Nucl. Instrum. Methods Phys. Res. B **83**, 68 (1993).
- 412 M. Gonin *et al.*, Rev. Sci. Instrum. **65**, 648 (1994).
- 413 A. Burgi *et al.*, J. Appl. Phys. **73**, 4130 (1993).
- 414 M. Gonin *et al.*, Nucl. Instrum. Methods Phys. Res. B **94**, 15 (1994).
- 415 M. Gonin *et al.*, Nucl. Instrum. Methods Phys. Res. B **101**, 313 (1995).



- <sup>416</sup>R. Kallenbach *et al.*, Nucl. Instrum. Methods Phys. Res. B **103**, 111 (1995).
- <sup>417</sup>E. J. Sternglass, Phys. Rev. **108**, 1 (1957).
- <sup>418</sup>E. S. Parilis and L. M. Kishinevskii, Sov. Phys. Solid State **3**, 885 (1960).
- <sup>419</sup>W. Meckbach, in *Beam-Foil Spectroscopy*, edited by I. A. Sellin and D. J. Pegg (Plenum, New York, 1976), Vol. 2, pp. 577–592.
- <sup>420</sup>B. E. Baklitskii *et al.*, Sov. Phys. Tech. Phys. **20**, 1513 (1976).
- <sup>421</sup>H. Rothard *et al.*, in *Particle Induced Electron Emission II* (Springer, Berlin, 1992), pp. 97–147.
- <sup>422</sup>W. Meckbach *et al.*, J. Phys. B **8**, L344 (1975).
- <sup>423</sup>V. Kh. Likhtenshtein and I. I. Tankov, Sov. Tech. Phys. Lett. **1**, 424 (1975).
- <sup>424</sup>V. Kh. Liechtenstein *et al.*, Radio Eng. Electron. Phys. **23**, 107 (1978).
- <sup>425</sup>K. Kuroki and Y. Yamazaki, Nucl. Instrum. Methods Phys. Res. B **33**, 276 (1988).
- <sup>426</sup>M. A. Gruntman *et al.*, Instrum. Exp. Tech. **32**, 668 (1989).
- <sup>427</sup>V. B. Leonas, Sov. Phys. Usp. **34**, 317 (1991).
- <sup>428</sup>R. E. Barrington and J. M. Anderson, Proc. Phys. Soc. London **72**, 717 (1958).
- <sup>429</sup>C. F. G. Delaney and P. W. Walton, IEEE Trans. Nucl. Sci. **NS-13**, 742 (1966).
- <sup>430</sup>L. A. Dietz and J. C. Sheffield, J. Appl. Phys. **46**, 4361 (1975).
- <sup>431</sup>Y. Yamazaki and K. Kuroki, Nucl. Instrum. Methods Phys. Res. A **262**, 118 (1987).
- <sup>432</sup>G. Lakits *et al.*, Rev. Sci. Instrum. **60**, 3151 (1989).
- <sup>433</sup>G. Lakits and H. Winter, Nucl. Instrum. Methods Phys. Res. B **48**, 597 (1990).
- <sup>434</sup>G. Lakits *et al.*, Phys. Rev. B **42**, 15 (1990).
- <sup>435</sup>K. Ohya *et al.*, Phys. Rev. B **46**, 3101 (1992).
- <sup>436</sup>P. Sigmund, Phys. Rev. **184**, 383 (1969).
- <sup>437</sup>K. C. Hsieh *et al.*, J. Appl. Phys. **51**, 2242 (1980).
- <sup>438</sup>K. C. Hsieh *et al.*, Nucl. Instrum. Methods Phys. Res. B **61**, 187 (1991).
- <sup>439</sup>J. A. R. Samson and R. B. Cairns, Appl. Opt. **4**, 915 (1965).
- <sup>440</sup>E. Dietz *et al.*, Nucl. Instrum. Methods **97**, 581 (1971).
- <sup>441</sup>E. Dietz *et al.*, Nucl. Instrum. Methods **108**, 607 (1973).
- <sup>442</sup>J. D. Bowman and R. H. Heffner, Nucl. Instrum. Methods **148**, 503 (1978).
- <sup>443</sup>T. Odenweller *et al.*, Nucl. Instrum. Methods **198**, 263 (1982).
- <sup>444</sup>A. V. Mitrofanov, Instrum. Exp. Tech. **26**, 971 (1983).
- <sup>445</sup>A. V. Mitrofanov and P. Yu. Apel, Nucl. Instrum. Methods Phys. Res. A **282**, 542 (1989).
- <sup>446</sup>G. N. Flerov and V. S. Barashenkov, Sov. Phys. Usp. **17**, 783 (1975).
- <sup>447</sup>B. E. Fischer and R. Spohr, Rev. Mod. Phys. **55**, 907 (1983).
- <sup>448</sup>R. Spohr, *Ion Tracks and Microtechnology* (Friedrich Vieweg & Sons Verlagsgesellschaft mbh, Braunschweig, 1990).
- <sup>449</sup>C. Riedel and R. Spohr, Radiat. Eff. **42**, 69 (1979).
- <sup>450</sup>A. V. Mitrofanov *et al.*, Nucl. Instrum. Methods Phys. Res. A **308**, 347 (1991).
- <sup>451</sup>V. A. Mitrofanov *et al.*, *EUV, X-Ray, and Gamma-Ray Instrumentation for Astronomy V*, Proc. SPIE 2280, edited by O. H. Siegmund and J. V. Vallerga (SPIE, Bellingham, 1994), pp. 272–277.
- <sup>452</sup>J. P. O'Sullivan and G. C. Wood, Proc. R. Soc. London, Ser. A **317**, 511 (1970).
- <sup>453</sup>R. C. Furneaux *et al.*, Nature (London) **337**, 147 (1989).
- <sup>454</sup>R. C. Furneaux and M. C. Thornton, Br. Ceram. Proc. **43**, 93 (1988).
- <sup>455</sup>R. C. Furneaux *et al.*, Mater. Res. Soc. Symp. Proc. **188**, 281 (1990).
- <sup>456</sup>M. C. Thornton and R. C. Furneaux, J. Mater. Sci. Lett. **10**, 622 (1991).
- <sup>457</sup>H. Masuda and K. Fukuda, Science **268**, 1466 (1995).
- <sup>458</sup>E. H. Anderson, Ph.D. dissertation, Massachusetts Institute of Technology, Cambridge, MA, 1988.
- <sup>459</sup>A. Yen *et al.*, Appl. Opt. **31**, 2972 (1992).
- <sup>460</sup>A. Yen *et al.*, Appl. Opt. **31**, 4540 (1992).
- <sup>461</sup>T. A. Savas *et al.*, J. Vac. Sci. Technol. B **13**, 2732 (1995).
- <sup>462</sup>M. L. Schattensburg *et al.*, J. Vac. Sci. Technol. B **13**, 3007 (1995).
- <sup>463</sup>M. L. Schattensburg *et al.*, *X-Ray Instrumentation in Astronomy II*, Proc. SPIE 980 (SPIE, Bellingham, 1988), pp. 210–218.
- <sup>464</sup>M. L. Schattensburg *et al.*, Opt. Eng. **30**, 1590 (1991).
- <sup>465</sup>D. W. Keith *et al.*, Phys. Rev. Lett. **61**, 1580 (1988).
- <sup>466</sup>C. R. Eckstrom *et al.*, Appl. Phys. B: Lasers Opt. **54**, 369 (1992).
- <sup>467</sup>H. S. Ogawa *et al.*, Opt. Eng. **32**, 3121 (1993).
- <sup>468</sup>J. A. R. Samson, Nucl. Instrum. Methods **152**, 225 (1978).
- <sup>469</sup>J. H. Hoffman *et al.*, Geochim. Cosmochim. Acta **3**, 2865 (1973).
- <sup>470</sup>M. A. Gruntman *et al.*, EOS Trans. AGU, Fall Meeting Suppl., **72** (44), 393 (1991).
- <sup>471</sup>A. W. Kleyn, *Proceedings of the Fifth International Symposium on the Production and Neutralization of Negative Ions and Beams*, AIP Conf. Proc. 210, edited by A. Hershcovitch (AIP, New York, 1990), pp. 3–16.
- <sup>472</sup>Yu. Belchenko, Rev. Sci. Instrum. **64**, 1385 (1993).
- <sup>473</sup>J. R. Hiskes and A. M. Karo, Bull. Am. Phys. Soc. **23**, 702 (1978).
- <sup>474</sup>P. Massmann *et al.*, Nucl. Instrum. Methods **165**, 531 (1979).
- <sup>475</sup>J. N. M. Van Wunnik and J. Los, Phys. Scr. **T6**, 27 (1983).
- <sup>476</sup>H. Verbeek *et al.*, *Proceedings of the 3rd International Symposium on Production and Neutralization of Negative Ions and Beams*, AIP Conf. Proc. 111, edited by K. Prelec (AIP, New York, 1984), pp. 273–280.
- <sup>477</sup>P. J. Schneider *et al.*, Phys. Scr. **T6**, 35 (1983).
- <sup>478</sup>J. R. Hiskes and P. J. Schneider, Phys. Rev. B **23**, 949 (1981).
- <sup>479</sup>M. Seidl *et al.*, in *Microwave and Particle Beam Sources and Directed Energy Concepts*, 106I (SPIE, Bellingham, 1989), pp. 547–554.
- <sup>480</sup>P. W. Van Amersfoort *et al.*, J. Appl. Phys. **58**, 3566 (1985).
- <sup>481</sup>J. N. M. Van Wunnik, Surf. Sci. **131**, 1 (1983).
- <sup>482</sup>H. L. Cui, J. Vac. Sci. Technol. A **9**, 1823 (1991).
- <sup>483</sup>C. F. A. Van Os *et al.*, J. Appl. Phys. **64**, 3863 (1988).
- <sup>484</sup>P. J. Schneider *et al.*, Phys. Rev. B **23**, 941 (1981).
- <sup>485</sup>J. N. M. Van Wunnik *et al.*, Surf. Sci. **131**, 17 (1983).
- <sup>486</sup>A. E. Souzis *et al.*, J. Vac. Sci. Technol. A **7**, 720 (1989).
- <sup>487</sup>S. T. Melnychuk and M. Seidl, J. Vac. Sci. Technol. A **9**, 1650 (1991).
- <sup>488</sup>C. F. A. Van Os *et al.*, Appl. Phys. Lett. **51**, 1495 (1987).
- <sup>489</sup>A. Danon and A. Amirav, Phys. Rev. Lett. **61**, 2961 (1988).
- <sup>490</sup>P. Wurz *et al.*, Surf. Sci. **373**, 56 (1997).
- <sup>491</sup>P. J. M. Van Bommel *et al.*, J. Appl. Phys. **56**, 751 (1984).
- <sup>492</sup>H. M. Van Pijsteren *et al.*, Europhys. Lett. **10**, 715 (1989).
- <sup>493</sup>D. Teillet-Billy and J. P. Gauryacq, Surf. Sci. **239**, 343 (1990).
- <sup>494</sup>S. Hayakawa *et al.*, Rev. Sci. Instrum. **63**, 1958 (1992).
- <sup>495</sup>P. Haochang *et al.*, Phys. Rev. Lett. **57**, 3035 (1986).
- <sup>496</sup>P. H. F. Reijnen *et al.*, J. Chem. Phys. **94**, 695 (1991).
- <sup>497</sup>H. S. W. Massey, *Negative Ions* (Cambridge University Press, Cambridge, 1976).
- <sup>498</sup>B. M. Smirnov, *Negative Ions* (McGraw-Hill, New York, 1982).
- <sup>499</sup>P. J. Schneider *et al.*, Nucl. Instrum. Methods Phys. Res. B **2**, 525 (1984).
- <sup>500</sup>W. Husinsky *et al.*, Nucl. Instrum. Methods Phys. Res. B **33**, 824 (1988).
- <sup>501</sup>C. C. Hsu *et al.*, Nucl. Instrum. Methods Phys. Res. B **119**, 471 (1996).
- <sup>502</sup>E. E. Scime and P. A. Keiter, Rev. Sci. Instrum. **68**, 296 (1997).
- <sup>503</sup>T. Yasue *et al.*, Jpn. J. Appl. Phys., Part 2 **25L**, 363 (1986).
- <sup>504</sup>M. A. Gruntman, Adv. Space Res. **13** (6), 141 (1993).
- <sup>505</sup>D. G. Mitchell *et al.*, Eos Trans. AGU., Spring Meeting Suppl. **77** (17), S250 (1996).